DEPARTAMENTO DE ASTROFÍSICA

Universidad de La Laguna

GALAXIES WITH MULTIPLE BARS: CONSTRAINTS ON THEIR FORMATION SCENARIOS

Memoria que presenta
ADRIANA DE LORENZO-CÁCERES RODRÍGUEZ
para optar al grado de
Doctora en Ciencias Físicas.

INSTITUTO Đ ASTROFÍSICA Đ CANARIAS
enero de 2013

Examination date: September, 2012
Thesis supervisor: Dr. Alexandre Vazdekis Vazdekis

Some of the material included in this document has been already published in *The Astrophysical Journal* and *The Monthly Notices of the Royal Astronomical Society*.

A mi abuelo

Y en el mundo, en conclusión,
todos sueñan lo que son,
aunque ninguno lo entiende
La vida es sueño (Calderón de la Barca)

Abstract

Much of current astrophysical research is aimed at addressing one key issue: how galaxies form and evolve. We still do not fully understand the evolutionary processes driving the lifetimes of the zoo of galaxies which populate the Universe. Galaxies may be isolated, or in groups or clusters; they may appear as pure ellipsoids or discs or include a variety of structures; they may be forming stars violently or passing quietly through their lives; and the many other properties that we are progressively discovering. Each piece we add to the puzzle pile complicates the picture a bit more. This thesis is aimed at fixing one of these pieces, a specific one related to the very interesting, but so far not well characterised, double-barred galaxies.

Barred galaxies are rather common structures in the Universe and, more importantly, they are key elements for secular evolution theories. In fact, bars can transport gas to the central regions of galaxies and trigger the formation of bulges and other new structures. Double bars go a step farther: they allow the material to reach the very central regions where the gas driven inwards by a single bar cannot get to. Therefore, nested bar systems are considered a very efficient way to bring about the internal secular evolution of galaxies and even to feed active galactic nuclei. This hypothesis has, however, some detractors, as it is very promising from a theoretical point of view but there is not much observational evidence that it is valid.

In this thesis we have carefully observed and studied a sample of five double-barred galaxies using the state-of-the-art techniques for the analysis of their kinematics and stellar populations. This has led to original work not previously performed, so each result is relevant and provides clues to the nature of these objects. We are pleased to present the discovery of the σ-hollows, the only known kinematical signature of the presence of stellar inner bars. Moreover, we disentangle the complex structural composition of the galaxies of our sample, dealing with different formation scenarios and rejecting those which do not account for the observational properties derived here. We find out that

one out of the five galaxies is probably hosting a disc-like bulge, whereas the other four present a classical bulge in their centres. Finally, we ascertain that inner bars tend to be younger and more metal-rich than the outer structures. Nevertheless, the characteristic stellar populations for the bulge and the inner bar are indistinguishable and there is no evidence of star-forming structures in the central regions of these galaxies, so we have to conclude that these five inner bars are not playing a major role in the secular evolution of their host galaxies.

Resumen

Gran parte de la investigación astrofísica actual gira en torno a una única e importante cuestión: cómo se forman y evolucionan las galaxias. Todavía hoy no comprendemos los procesos evolutivos que dirigen la vida de ese zoo de objetos que puebla el Universo. Las galaxias pueden estar aisladas o viviendo en grupos o cúmulos; pueden aparentar ser simple elipsoides o discos o estar constituídas por variedad de estructuras; pueden formar estrellas violentamente o dejar pasar tranquilamente sus vidas; y un largo etcétera de propiedades que vamos descubriendo poco a poco. Cada pieza que añadimos al puzle complica la imagen final un poco más. Esta tesis pretende colocar por fin una de esas piezas, aquella relacionada con el fascinante, aunque todavía poco estudiado, caso de las galaxias con dos barras.

Las galaxias con barra son estructuras comunes en el Universo y elementos clave en las teorías de evolución secular, puesto que las barras son capaces de transportar gas a las regiones centrales y, por lo tanto, promover la formación de bulbos y otras estructuras. Las dobles barras van un paso más allá al permitir que el material alcance las partes más internas de las galaxias, donde el gas transportado por una barra simple no puede llegar. Es por tanto lógico que estos sistemas dobles sean considerados fundamentales y muy eficientes para la evolución secular interna de las galaxias, e incluso se les relaciona a menudo con los núcleos activos galácticos. Esta hipótesis encuentra, sin embargo, varios detractores, pues aunque es muy prometedora desde un punto de vista puramente teórico, no hay evidencias observacionales que la sustenten.

En la presente tesis hemos observado y estudiado en detalle una muestra de cinco galaxias con dos barras y hemos hecho uso de las técnicas de análisis más novedosas con el objetivo de caracterizar su cinemática y poblaciones estelares. Se trata de un trabajo completamente original jamás antes realizado, por lo que cada resultado es relevante y proporciona nuevas pistas sobre la naturaleza de estos objetos. Así pues, presentamos el descubrimiento de los llamados σ-*hollows*, las únicas señales cinemáticas conocidas de la presencia

de barras internas. Desentrañamos también la compleja composición estructural de las galaxias de nuestra muestra, considerando los diferentes escenarios de formación posibles y rechazando aquellos que no explican las propiedades observacionales encontradas. Obtenemos así que una de las cinco galaxias en estudio probablemente contiene un bulbo tipo disco, mientras que el resto de la muestra está compuesta por bulbos clásicos. Finalmente, averiguamos que las barras internas tienden a ser más jóvenes y metálicas que las estructuras externas; sin embargo, las poblaciones estelares características para el bulbo y la barra interna son indistinguibles y no hay evidencias de formación estelar relevante en las regiones centrales, por lo que concluimos que al menos estas cinco barras internas no están desempeñando un papel importante en la evolución secular de sus galaxias anfitrionas.

Contents

List of Figures

1

On barred galaxies and secular evolution

Sole orto, spes; ...

All the great projects and discoveries are triggered by one or more key questions. It is amazing that nowadays, despite all our scientific knowledge and technical advance, we are still dismayed by basic questions such as *how are the galaxies in the Universe forming? How are they changing and evolving? Why are there so many different types of galaxies?* The main goal of this thesis is to fit a new piece of the general puzzle that is the formation and evolution of the Universe that, at the end, is described by the formation and evolution of the galaxies which populate it. But let us start from the beginning...

1.1 The great variety of galaxies: the Hubble sequence

Galaxies in the Universe show a wide range of properties, their visual morphologies being the most evident example of the intrinsic differences among them. The first morphological classification scheme was introduced by Edwin Hubble already in 1936. Hubble had realised that many galaxies presented a stellar spheroidal component, so he decided to divide the *nebulae* (now called galaxies) by the relative, visual importance of their spheroidal structure. Hence, Hubble created the so-called *Tuning-Fork* diagram (see Figure 1.1), in which galaxies are classified in three main classes: ellipticals (E), completely ellipsoidal and structureless; lenticulars (S0), made up by a central spheroidal component called *bulge* and a disc-like structure; and spirals (S, SB), composed also by a

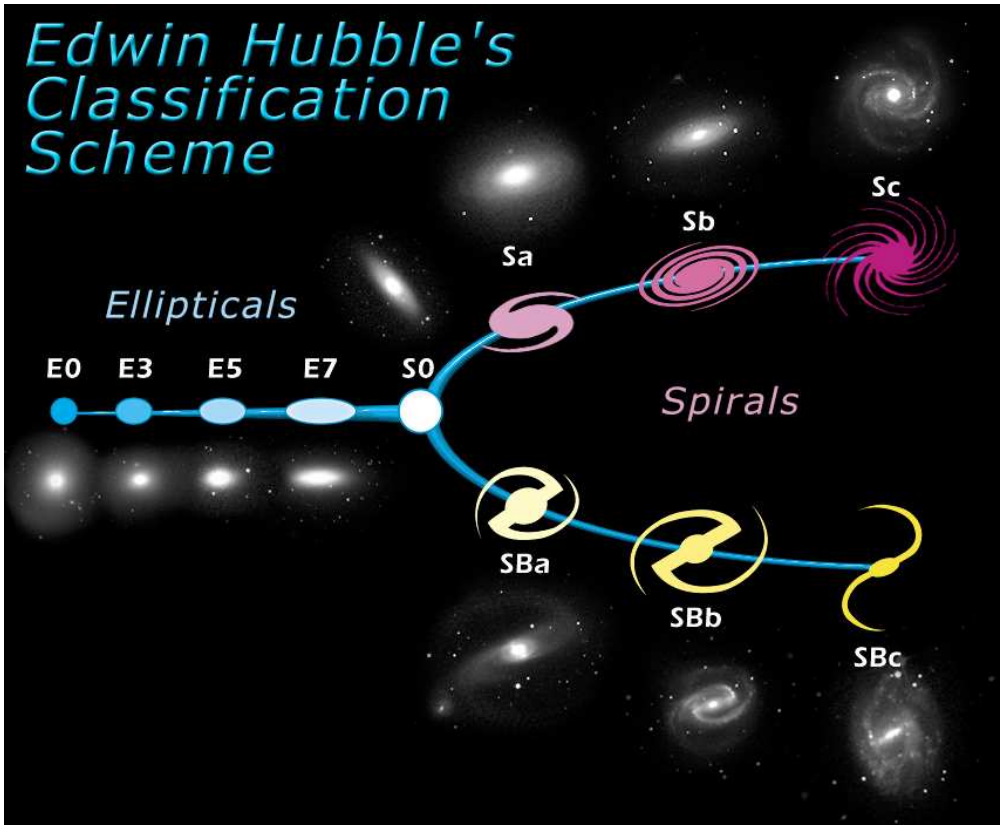

FIGURE 1.1— *Tuning-Fork* diagram from Hubble (1936). This classification scheme divides the galaxies in three main groups in accordance with their visual morphology: ellipticals (E), lenticulars (S0), and spirals (S). Spirals are in turn classified in two classes, namely non-barred (S) and barred (SB) galaxies.

bulge and a disc, apart from a spiral structure that shines out in the disc and sets the name of this broad class of galaxies. Within the elliptical class, galaxies are divided into subgroups following their ellipticity as a criterion, from the most spherical E0 galaxies, placed at the left-side of the Hubble diagram, to the most elongated ellipticals that make up the E7 class, preceding the lenticulars. In fact, lenticulars mark the transition between the ellipticals and the broad spirals group which, in turn, is divided in two main branches: *normal* and *barred* spirals. A barred galaxy is characterised by the elongated, non-axisymmetric, bar-like stellar component present in its central zone, interior to the spiral arms. Barred and non-barred spirals are also subclassified in different

types depending on the relative prominence of the bulge and spiral structures, so the Sa galaxies are dominated by the bulge whereas the Sc galaxies show almost no bulge but very prominent spiral arms. Finally, galaxies relying outside the Tuning-Fork diagram, with non ellipsoidal nor disc-like structure, were considered by Hubble as *irregulars* (I).

The morphological classification performed by Hubble has been refined over the years, taking into account new structures, such as rings or shells, and different morphologies due to galaxy interactions or mergers, such as tidal streams and complicated shapes that place the galaxy into the *peculiar* class. Intermediate types between barred and non-barred galaxies (SAB) have been also added, as well as several spiral subclasses (Sd, Sm; see de Vaucouleurs et al., 1991, for a detailed classification of over 20,000 galaxies). Nevertheless, the basis of the Hubble diagram is still relevant; but Hubble went a step beyond the simple classification of galaxies when he proposed also an evolutionary process from the left- to right-sides of the diagram. Following this hypothesis, galaxies would begin their lives as ellipticals and they would gradually change their morphologies towards the spiral types. In fact, galaxies are still considered as early- or late-types depending on their position on the Hubble sequence, although Hubble's evolutionary concept is not longer considered valid.

It is worth noting the revision of the Tuning-Fork diagram introduced by van den Bergh (1976), who proposed a sequence in which lenticulars are placed in their own branch (S0a-S0b-S0c), which is parallel and analogous to that composed by spirals (Sa-Sb-Sc). The diagram of van den Bergh (1976) is driven exclusively by the bulge-to-total light ratio of the objects, so S0 or simply S galaxies with small bulges are placed at the right-end of their respective sequences. The main novelty introduced by van den Bergh (1976) is the hypothesis that galaxies can evolve between these two main branches, so lenticulars are, in fact, spiral galaxies which have lost their spiral structure and star formation due to evolutionary processes such as ram-pressure stripping of their cold gas in rich environments. Recently, Kormendy & Bender (2012) have proposed a revised version of the parallel sequence of van den Bergh (1976); in their work, Kormendy & Bender (2012) include the pure spheroidal galaxies (Sph) as the next step in the lenticulars sequence, in the same way as irregulars extend the spirals branch (see Figure 1.2). Therefore, the evolutionary scenario proposed by Kormendy & Bender (2012) creates spheroidal galaxies through the ram-pressure stripping of cold gas from Sc-Sd-I galaxies. Barred galaxies do not occupy a distinguished place in the diagram of Kormendy & Bender (2012), as they are included in the corresponding lenticulars or spirals branch.

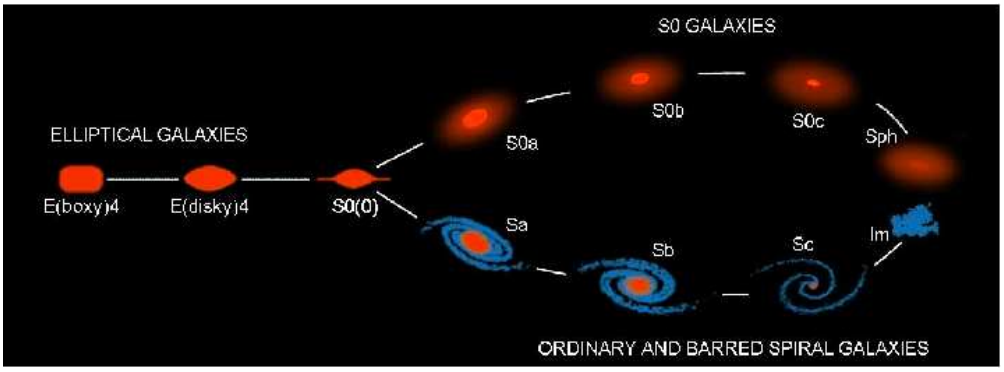

FIGURE 1.2— Morphological classification proposed by Kormendy & Bender (2012). Spirals (S) and lenticulars (S0) are placed in two parallel sequences driven by their bulge-to-total light ratios, which decreases towards the right-end. Irregulars (Im or simply I) and spheroidals (Sph) are bulgeless. Kormendy & Bender (2012) propose an evolutionary process between these two main branches, so S0 and Sph come from S and latest-type S and I, respectively. *Figure taken from Kormendy & Bender (2012).*

To summarise, the morphological diagram of Hubble (1936) and their most recent versions are not simply classifications but evolutionary diagrams which propose different structural transformations in order to explain the wide variety of galaxies observed nowadays. However, these evolutionary scenarios are still a matter of discussion, since the general evolution of galaxies, how they form and how they change during their lifetimes, is still an open question.

1.2 Structural evolution scenarios. The nature of bulges

Galaxies are continuously affected by physical processes that may induce morphological changes. Universe is in transition, so the dominant driver of galaxy evolution will depend on the cosmic epoch and timescale of these changes (Kormendy & Kennicutt, 2004). In fact, consequences of different evolutionary processes may coexist in a single galaxy. Figure 1.3 shows the most extended schematic visualisation of the variety of processes that might drive galactic morphological evolution (Zwicky, 1957; Kormendy & Kennicutt, 2004).

Fast processes are violent and dominated during early cosmic epochs, when monolithic collapse and mergers induced dissipation and star formation, thus forming new galaxies. These processes happened on very short timescales in discrete events. On the other hand, slow, gradual processes are important on significantly longer timescales; these are known as *secular* processes, which may

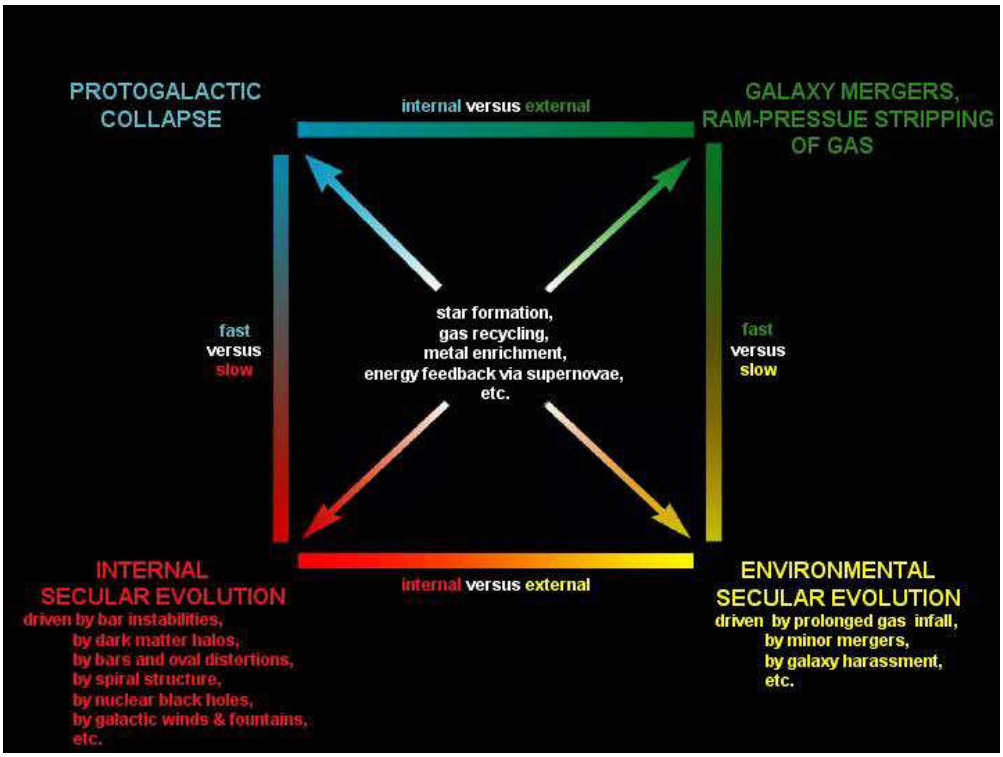

FIGURE 1.3— Morphological box diagram (Zwicky, 1957; Kormendy & Kennicutt, 2004). The processes that drive the morphological evolution of galaxies are classified into *fast* (top) and *slow* (bottom), according to their timescale, and in *internal* (left), if they take place in the galaxy without external factors, and *environmental* (right), when they are triggered by external agents. Processes at the centre of the box are compatible with all the possibilities. *Figure taken from Kormendy & Kennicutt (2004).*

be triggered by environmental factors, such as mergers or interactions, or by the internal rearrangement of material due to non-axisymmetric structures, galactic winds, or black holes, among others. When compared, the violence of fast processes such as major mergers dominate the more subtle effects of the slow secular evolution. However, the frequency of major mergers falls with cosmic time (e.g., López-Sanjuan et al., 2009), so internal processes acquire a significant effect on the structural transformation of galaxies once the merging process has weakened and the timescale is long enough to let the secular evolution take place. Therefore, all the processes included in Figure 1.3 may promote that galaxies evolve from late to early types along the Hubble sequence and form

new components. In particular, they are related to the formation of bulges.

Bulges are properly defined as the central excess of light found in the brightness distribution of a disc galaxy, i.e., they imply a central concentration of stars. According to their photometric and kinematical properties, bulges are classified in two main groups, which are also linked to the different evolutionary processes that have formed them:

- ***Classical* bulges.** Photometrically, they are well-described by a Sérsic profile (Sérsic, 1968):

$$I(r) = I_e \, 10^{-b_\mathrm{n}\left[\left(\frac{r}{R_\mathrm{e}}\right)^{1/n}-1\right]}, \tag{1.1}$$

  where I_e is the intensity at the *effective radius* of the galaxy (R_e), which encloses half of its total light; n is a shape index which describes the curvature of the profile; and the value of b_n is a function of n, which can be approximated by a linear relation given by Caon et al. (1993). In particular, classical bulges are characterised by showing high n index values ($n > 2$, Fisher & Drory, 2008; see also Andredakis et al., 1995; Scannapieco & Tissera, 2003). Concerning the kinematics, it is dominated by random motions, so classical bulges are pressure-supported structures (e.g., Kormendy & Illingworth, 1982; Cappellari et al., 2006).

  In general, classical bulges are considered analogous to elliptical galaxies, since they show very similar properties. Moreover, they are mainly found in early-type hosts and the bulk of their stellar populations is old (e.g., Peletier et al., 1999). The formation and growth of this kind of bulges is thought to be driven by fast processes, such as monolithic collapse or hierarchical scenarios such as mergers (see e.g., Kauffmann, 1996; Merlin & Chiosi, 2006; Aguerri et al., 2001).

- ***Disc-like* bulges**. Usually known as *pseudobulges* (Kormendy & Kennicutt, 2004), their luminosity profile is also fitted by a Sérsic law, but with rather lower n values than classical bulges ($n < 2$, Fisher & Drory, 2008; see also Andredakis & Sanders, 1994; MacArthur et al., 2003). These bulges are rotational-supported, i.e., their stellar kinematics is mostly dominated by ordered motions, as in the case of discs. The last main difference with respect to classical bulges is that disc-like bulges present rather younger stellar populations (e.g., Goudfrooij et al., 1999). Finally, this kind of structures appear mainly in late-type spirals, although they have been also found in early-types (Erwin et al., 2004).

Kormendy & Kennicutt (2004) suggest that disc-like bulges are formed by secular evolution processes that take place inside the galaxies, mainly thanks to bars that drive gas towards the central regions, where it can trigger star formation. Minor merging processes might also promote the gas inflow and contribute to the secular growth of bulge structures (Aguerri et al., 2001; Eliche-Moral et al., 2006).

As explained, the level of rotation with respect to random motions of bulges is closely related to their nature (classical or disc-like bulges) and the way they were formed. Figure 1.4 represents a V/σ vs. ellipticity diagram for several stellar systems, where V is their maximum velocity and σ is their velocity dispersion inside the half-light region. The relative importance of the motions that dominate the kinematics of these systems is therefore highlighted in this diagram. Elliptical galaxies present almost no-rotation and are extremely anisotropic; on the other hand, disc-like bulges are dominated by velocity dispersion isotropy and present a high level of rotation. Classical bulges, in the middle of both extreme situations, are consistent with being isotropic oblate spheroids.

To summarise, among the different factors responsible for the secular evolution of galaxies, non-axisymmetric structures are specially relevant due to their efficiency and high frequency in the Universe (e.g., Aguerri et al., 2009, but see Section 1.3 for a wider and more detailed explanation). Bars, and stellar bars in particular, are considered key elements for evolution scenarios, and they tend to be directly related to the formation of spheroidal structures, specially disc-like bulges.

1.3 Short review on barred galaxies

Bars have been extensively studied in the literature since the beginning of the twentieth century. Searching methods, observational properties, and numerical simulations have been performed in order to fully characterise the population of barred galaxies in the local Universe and beyond, and finally understand the formation processes that generate bars and their evolution along their lifetimes, which is still matter of discussion.

1.3.1 The bar fraction

How many barred galaxies are in the Universe? Observations at redshift $z \sim 0$ and optical wavelengths have found that $\sim$45% of nearby disc galaxies host a bar (Marinova & Jogee, 2007; Reese et al., 2007; Barazza et al., 2008; Aguerri et al., 2009; Masters et al., 2011), but this fraction rises up to $\sim$60-70% when moving towards infrared bands, which are unaffected by dust extinction (Knapen et al.,

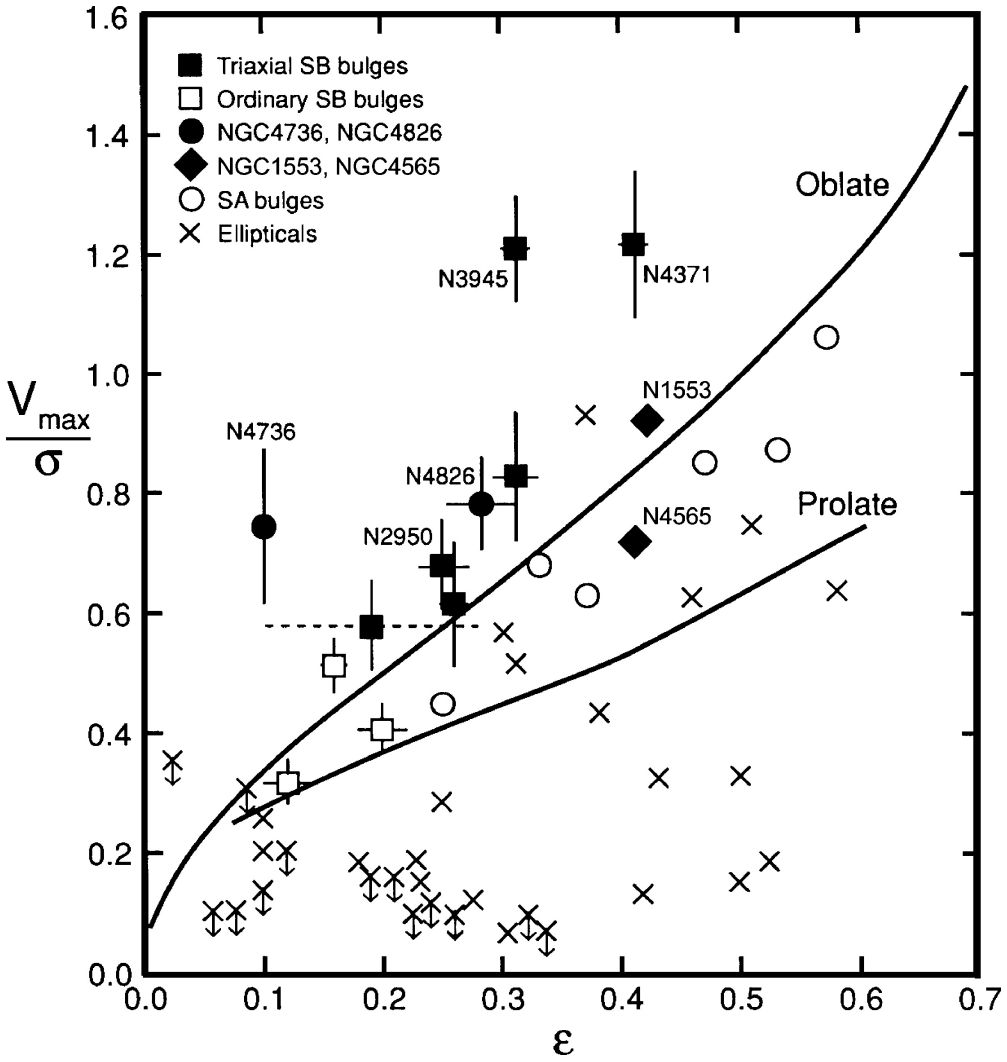

FIGURE 1.4— V/σ vs. ϵ diagram for several representative stellar systems. V is the maximum velocity whereas σ is the velocity dispersion; this ratio is measured inside the half-light radius and it represents the level of ordered motions compared to random motions of the system. ϵ is the ellipticity, which traces the flattening of the system and it is related to its gravitational potential. Crosses are giant elliptical galaxies, filled symbols are disc-like bulges, and open circles are classical bulges. The oblate line describes the behaviour of an isotropic, oblate spheroid flattened due to its rotation, while the prolate line shows that prolate spheroids may be flattened due to velocity dispersion anisotropy, thus rotating more slowly. *Figure taken from Kormendy & Kennicutt (2004).*

2000; Laurikainen et al., 2004; Menéndez-Delmestre et al., 2007; Aguerri et al., 2009; Barway et al., 2011). Bars are therefore common structures in the local Universe.

The evolution of the bar fraction with redshift is still a matter of debate, given the difficulties inherent in the detection of structures in the central regions of distant galaxies, and problems with selection effects. Several works claim that the frequency of bars keeps constant from the local Universe to redshift $z \sim 1.2$ (Sheth et al., 2003; Jogee et al., 2004; Elmegreen et al., 2004; Cameron et al., 2010). However, a recent study by Sheth et al. (2008) finds a significantly lower bar fraction (dropping to about $\sim 20\%$) at $z = 0.84$ with respect to the present day. Bars appear naturally in simulations of galaxies with a cold, rotationally-supported disc due to dynamical instabilities, and they are mostly long-lived structures (e.g., Debattista & Sellwood, 2000; Athanassoula & Misiriotis, 2002; Martinez-Valpuesta et al., 2006; Berentzen et al., 2007); the survival of barred systems supports the idea that these structures are frequent at all cosmic epochs.

The bar fraction and its cosmic evolution are functions of galaxy luminosity and mass, Hubble type, and environment. Cameron et al. (2010) find that bars are more frequent in early-type discs than in later-types for intermediate galaxy masses, whereas this result is reversed for the most massive galaxies. Barway et al. (2011) focus on the case of S0 galaxies, finding that bars tend to appear in the faintest objects of their sample; moreover, they find also that cluster lenticulars show a higher bar fraction than their counterparts in the field, which suggests a close relation between the bar frequency and environment. In fact, interactions can promote bar formation (Noguchi, 1987) or, on the contrary, weaken the bars and even destroy them (Aguerri & González-García, 2009).

Méndez-Abreu et al. (2010, but see also Marinova et al., 2012) study in detail the bar fraction in a rich environment such as the Coma cluster, finding that barred galaxies are mostly located in a short range of high masses and luminosities, whereas the peak of the bar distribution for field galaxies is slightly moved toward fainter, less massive galaxies. They also compare regions within the cluster itself, from the central parts to the outskirts, finding no differences in the bar fraction among them. Finally, the dwarf regime completely lacks the presence of barred galaxies; it is remarkable that the disc nature of dwarf galaxies is a matter of discussion (Binggeli & Cameron, 1991; Ryden et al., 1999), and barred structures found by Lisker et al. (2006) in a set of dwarf galaxies are notable for this reason.

FIGURE 1.5— Barred galaxy NGC 1097 as observed in the optical range (left panel; *Credit: R. Jay GaBany, www.cosmotography.com*) and at infrared wavelengths (right panel; the final picture is a combination of three infrared images, at wavelengths of 3.6 μm -blue-, 4.5 μm -green-, and 8.0 μm -red- from the NASA's Spitzer Space Telescope *Credit: SINGS team*). The clear dust lanes present in the optical picture are not shown in the infrared image, which is transparent to dust extinction. Note however that the red glow tracing the spiral arms at 8.0 μm corresponds to emission from dust heated by hot stars, whereas blue colours represent the oldest population. As well as the bar, this galaxy presents a central black hole surrounded by a ring of stars.

1.3.2 Luminosity profile and photometric parameters

Stellar bars were first detected from photometric analyses at optical and near infrared wavelengths. The latter are less affected by the the obscuring dust extinction thus allowing a most accurate observation of the stellar structures (see Figure 1.5 for an example of a barred galaxy observed in the optical and infrared bands). Bar signatures appear in the isophotal fitting as components with commonly larger ellipticities and different position angles from the surrounding disc, while a surface-brightness decomposition requires the addition of a new structure to get a good match with the luminosity profile of a barred galaxy. A barred galaxy is therefore composed by, at least, three structures: a disc, whose azimuthally averaged luminosity profile is usually described by an exponential law (Freeman, 1970); a bulge, which follows the Sérsic profile already introduced in Equation 1.1; and the bar, with a surface-brightness profile that can be described by an elliptical or Freeman law (Freeman, 1966):

$$I_{\rm bar}^{\rm Freeman}(r) = I_{0,\rm bar}\sqrt{1-\left(\frac{r}{a_{\rm b}}\right)^2}, \qquad (1.2)$$

a Ferrers ellipsoid (Ferrers, 1877):

$$I_{\rm bar}^{\rm Ferrers}(r) = I_{0,\rm bar}\left[1-\left(\frac{r}{a_{\rm b}}\right)^2\right]^{n_{\rm b}+0.5} \tag{1.3}$$

or a flat profile (Prieto et al., 1997):

$$I_{\rm bar}^{\rm Flat}(r) = I_{0,\rm bar}\frac{1}{1+e^{\frac{r-a_{\rm b}}{r_{\rm S}}}}, \tag{1.4}$$

In Equations 1.2, 1.3, and 1.4, $I_{0,\rm bar}$ and $a_{\rm b}$ represent the central surface-brightness of the bar and the bar length, respectively. The Ferrers profile (Equation 1.3) also includes the $n_{\rm b}$ parameter, which is a shape index, while the $r_{\rm S}$ parameter that appears in the flat profile (Equation 1.4) is a scale-length, so at radii larger than a_b the luminosity profile decays with a typical $r_{\rm S}$ distance. Figure 1.6 shows an example of the surface-brightness decomposition performed on a barred galaxy (Morelli et al., 2012).

Bars are described with two important photometric parameters: the bar length and strength. In fact, these two quantities together with a third dynamical parameter, the pattern speed (defined in Section 1.3.3), fully characterise a bar system. There are several definitions for the bar length, according to the criterion adopted for its measurement. The lack of a standard way to measure the bar size forces the researcher to choose the most convenient method, taking into account that different procedures may lead to final variations of up to $\sim$35% (Athanassoula & Misiriotis, 2002).

The simplest and direct methods to estimate the bar size are visual, well inspecting the images (Kormendy, 1979), considering the spiral arms or other out structures (e.g., rings) as tracers of the bar edges (Martin, 1995), or well analysing the variations in the slope of the luminosity profile along the bar major axis (Chapelon et al., 1999). Given that bars are usually identified by ellipse fitting to the galaxy isophotes, the distance where the maximum isophotal ellipticity is found (a_ϵ) inside the bar region provides a lower limit for the bar length, frequently taken as a first approximation (e.g., Wozniak & Pierce, 1991; Wozniak et al., 1995; Jungwiert et al., 1997; Sheth et al., 2003). A simple estimation of the bar size is therefore the radius of minimum ellipticity found outside a_ϵ ($a_{\rm min}$; Erwin, 2004, 2005). However, it is also usual to establish another criterion based on the position angle, for example the length where the difference between the position angles of the disc and bar exceeds $10^{\rm o}$ (a_{10}). The minimum of these two measurements, $a_{\rm min}$ and a_{10}, provides an upper limit for the true bar size ($L_{\rm bar}$; Erwin & Sparke, 2003; Erwin, 2005).

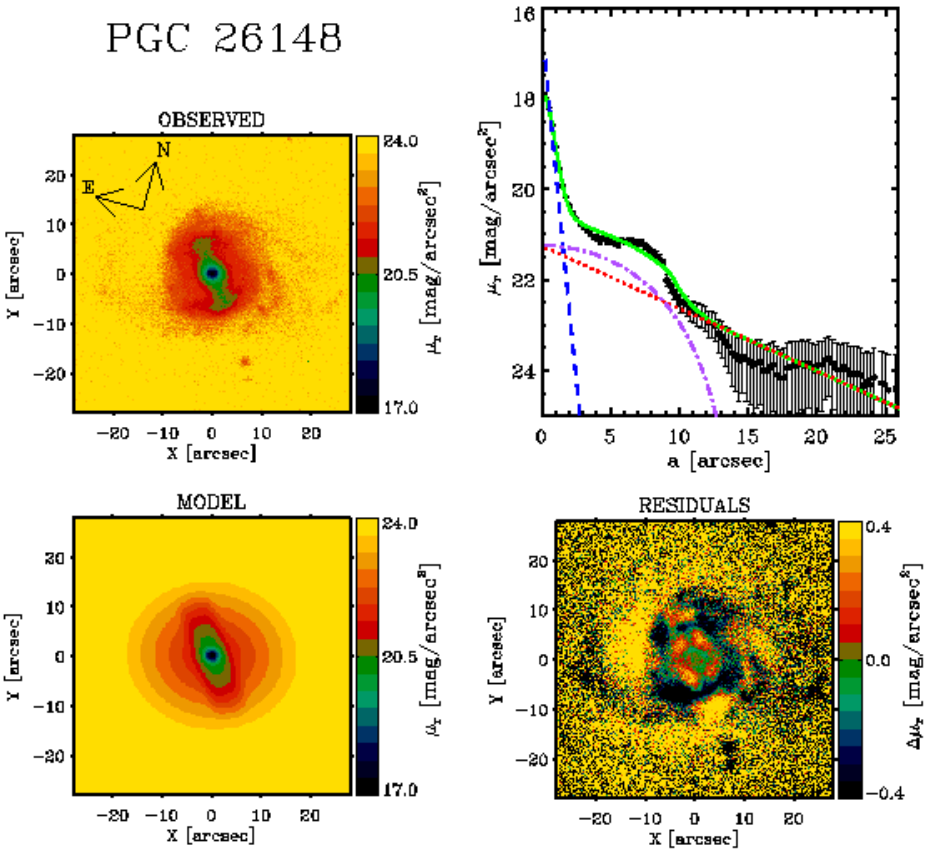

FIGURE 1.6— Example of a two dimensional photometric decomposition of the barred galaxy PGC 26148 from a FORS2 r-band image (top left panel). The best fitted model image and the residuals resulting from the subtraction of the model to the observed data are shown in the bottom row. The top right panel shows the surface-brightness radial profiles of the data (black dots) and the model image (green line), whereas the dashed blue, dot-dashed purple, and dotted red lines represent the intrinsic profiles of the bulge, bar, and disc, respectively. The photometric decomposition has been performed with the GASP2D fitting algorithm (Méndez-Abreu et al., 2008a). *Figure taken from Morelli et al. (2012).*

A complementary way of estimating the bar size is based on Fourier analysis: the image of a barred galaxy is deprojected and decomposed in a Fourier series. Even terms of this decomposition trace symmetric components, so the length at which the odd terms start to increase is a direct estimate of the bar size (Aguerri et al., 1998). However, there is a more valid way to derive the bar length: in the interbar region, where there is no bar and the disc is axisymmetric, only the 0-th order term acquires a non-zero value; the bar region, however, is a symmetric but non-axisymmetric component, and it is therefore dominated by even terms. Comparison between the even terms of the two regions provides a more accurate estimate of the bar length (Ohta et al., 1990; Elmegreen & Elmegreen, 1985; Aguerri et al., 2000, 2003, 2005, 2009).

The strength is a measurement of the shape and prominence of a bar, so this is considered *strong* if it is long, massive, elongated, and induces intense tangential forces, whereas *weak* bars are those which are small and with little gravitational influence on the rest of the galaxy. As in the case of the bar length, the strength can be estimated by visual inspection just according to the prominence of the bar in the galaxy, or using the bar ellipticity as a tracer of its shape (Martin, 1995; Shlosman et al., 2000; Laine et al., 2002). Methods based in the Fourier analysis taking into account the even terms are also used (Aguerri et al., 1998; Aguerri, 1999; Aguerri et al., 2000). However, the most extended way to estimate the bar strength is by means of the $Q_{\rm b}$ parameter, introduced by Buta & Block (2001). $Q_{\rm b}$ is measured as the maximum value of the ratio between the tangential force and the mean axisymmetric radial force in a barred potential, and correlates well with other strength estimators, such as the bar ellipticity (Laurikainen et al., 2002) or the parametrisation by Abraham & Merrifield (2000).

In the local Universe it has been found that early-type galaxies host longer bars than later types. As an example, Erwin (2005) obtains a mean size of $\sim$3.3 kpc for bars in SB0-SBb galaxies, whereas this value drops to $\sim$1.5 kpc for SBc-SBd types. Differences are even found between the lenticulars and the early-type galaxies, since the former tend to have even longer bars (Aguerri et al., 2009). There is also a positive correlation between the bar length and galaxy size independently of the Hubble type (Aguerri et al., 2009). Concerning the bar strength, lenticulars seem to present weaker bars that spirals in general, following a unimodal distribution for all galaxy types (Laurikainen et al., 2007; Aguerri et al., 2009).

Despite the fact that most photometrical studies of barred galaxies rely on the ellipsoidal approximation, observations and numerical simulations have

demonstrated that bars may present a great variety of deviations from the pure elliptical isophotes (Sparke & Sellwood, 1987; Combes et al., 1990; Athanassoula, 1990; Aguerri et al., 1998, 2000; Martinez-Valpuesta et al., 2006). In fact, bars have been found to present more oval or boxy shapes, or even more complex structures such as the *ansae* that appear at the bar edges, in the transition region with the galaxy disc (Martinez-Valpuesta et al., 2007). Ansae are frequent in early-type galaxies (Athanassoula, 1984) and have been attributed to the mass flow towards the spiral arms (Danby, 1965).

1.3.3 Dynamical properties: orbits, resonances, and pattern speeds

The dynamical composition of an non-axisymmetric potential as that of a barred galaxy is described by two fundamental frequencies, one associated with the bar itself and an additional one related to the free oscillations, which is defined as the local epicyclic frequency κ. Even so, the bar is embedded in the galaxy potential so the final orbital configuration results from the interaction of all the systems that shape the galaxy. In fact, some galactic orbits are resonant with the bar, i.e., the motions are coupled to the bar rotation thus generating closed orbits in the rest frame of the bar (Contopoulos & Papayannopoulos, 1980; Ceverino & Klypin, 2007).

The most important resonance is called *corotation* (CR hereafter), which happens at a radius r where $\Omega(r) = \Omega_{\rm b}$, i.e., the angular velocity of the stars is equal to the angular rotation velocity of the bar ($\Omega_{\rm b}$). Other relevant resonances are the *Inner Lindblad Resonance* (ILR hereafter), where $\Omega_{\rm b} = \Omega(r) - \kappa/2$, and the *Outer Lindblad Resonance* (OLR hereafter), where $\Omega_{\rm b} = \Omega(r) + \kappa/2$. Therefore, a star placed at any of the Lindblad resonances will cover two epicyclic oscillations during one angular revolution. It is important to note that a barred galaxy might show up to two ILRs, but only one OLR. Figure 1.7 illustrates the resonance concept by showing a scheme of these three main resonances in a single-barred potential.

Although CR, ILR, and OLR are the three main resonances, it is important to note that a barred potential has many other resonances associated to it, which provide different families of orbits. Some of these orbits may be rather exotic and give place to a variety of structures in the bar, such as the ansae mentioned in Section 1.3.2. Among the dynamical configurations of a barred galaxy, it is interesting to highlight the periodic orbits (Contopoulos & Grosbol, 1989), such as the x_1 family, elongated along the bar major axis and always within the corotation radius (Contopoulos & Papayannopoulos, 1980). This is the main family supporting the bar, as most of the stars which populate it are trapped by the x_1 orbits. Moreover, it is mainly composed by ILR resonant orbits (Athanassoula, 2003). The family of orbits perpendicular to the bar major

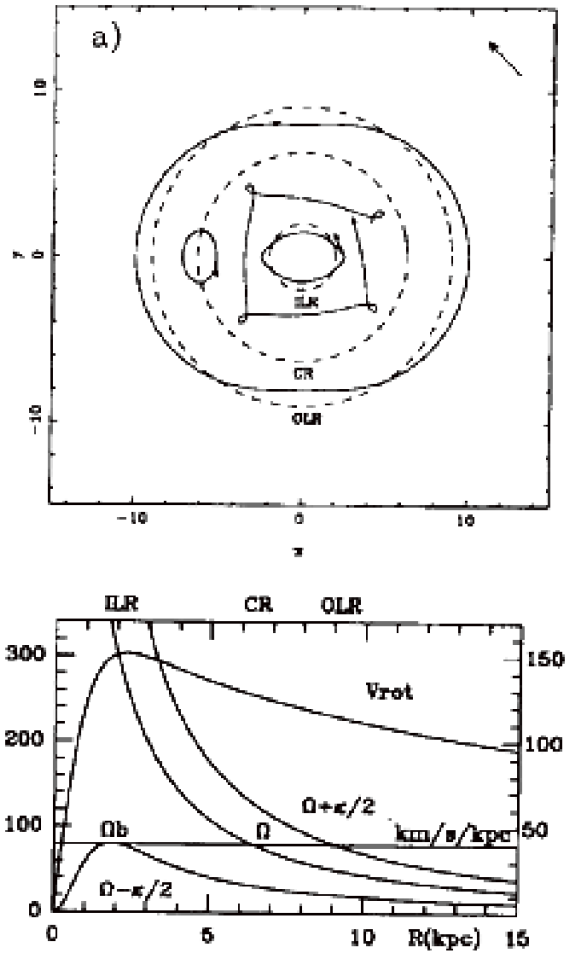

FIGURE 1.7— Scheme of the main resonances of a barred potential. The upper panel (a) shows the resonant orbits in the rotating rest frame of the bar, whereas the bottom panel (b) presents the rotation curve (km/s; left scale) and frequencies (km/s/kpc; right scale) of the disc ($V_{\rm rot}$), the corotation (Ω), and the ILR and the OLR ($\Omega(r) - \kappa/2$ and $\Omega(r) + \kappa/2$, respectively). The horizontal line indicates the pattern speed of the bar $\Omega_{\rm b}$. *Figure taken from Buta & Combes (1996).*

axis are called x_2 and they are placed between the two ILRs, if present (Buta & Combes, 1996). If the bar strength is high enough, the appearance of the x_2 orbits may be inhibited.

The pattern speed, $\Omega_{\rm b}$, is the third fundamental parameter that fully characterise a bar, together with the length and strength already defined in Section 1.3.2. This angular velocity is linked to the dark matter content of the galaxy, as very dense haloes slow down the bar because of dynamical friction (Debattista & Sellwood, 2000). It is also remarkable that bars in more concentrated haloes tend to be stronger than those formed in less dense ones, due to the higher mass concentration at the resonances, which promotes a more efficient angular momentum exchange with the galaxy disc (Athanassoula & Misiriotis, 2002; Athanassoula, 2003).

The pattern speed is usually parametrised by the ratio $R = R_{\rm CR}/a_{\rm b}$, where $R_{\rm CR}$ and $a_{\rm b}$ are the corotation radius and bar semi-major axis, respectively. This quantity is independent of the galaxy distance and establishes a criterion for classifying bars related to their pattern speed, so bars that extend almost toward the corotation radius are considered *fast* ($R \in [1., 1.4]$), while short bars ($R > 1.4$) are *slow*. Hence, the parameter R is an indirect estimate of the bar pattern speed, and given the intrinsic difficulties of a more proper determination of $\Omega_{\rm b}$, R has been extensively used to characterise the dynamics of a barred galaxy. The corotation radius can be derived with different indirect methods, such as the location of morphological structures (e.g., rings), analyses in the Fourier domain, or determination of the radius at which the star formation is inhibited (Cepa & Beckman, 1990; Puerari & Dottori, 1997; Aguerri et al., 1998; Pérez et al., 2012).

The most accurate way to derive the bar pattern speed is, however, the Tremaine-Weinberg method (TW hereafter; Tremaine & Weinberg, 1984), as it gets $\Omega_{\rm b}$ directly from kinematical observations. The TW is based on three fundamental assumptions: the selected tracer (which depends on the nature of the observations; e.g., optical wavelengths trace principally old stellar populations) satisfies the continuity equation, the galaxy disc is flat, and the bar pattern speed is well-defined and unique. If these conditions are fulfilled, the $\Omega_{\rm b}$ should be properly derived by measuring the luminosity-weighted mean velocities in slits parallel to the galaxy line of nodes.

The observations required to apply the TW method to a sample of galaxies are demanding and time-consuming; however, it has been used for analysing a moderate number of nearby galaxies, specially with high surface-brightness, finding that most of them host fast bars that end near the corotation radius (e.g., Debattista et al., 2002; Aguerri et al., 2003; Corsini et al., 2007). It is also worth noting that, despite the fact that gas does not obey the continuity equation, positive results have been found when applying the TW method to CO (Rand & Wallin, 2004; Zimmer et al., 2004) and Hα (Hernandez et al., 2005; Fathi et al., 2007, 2009) observations.

1.3.4 Stellar populations

The formation, evolution, and survival of bars are still open questions, despite all the observational evidence and theoretical analyses. Important evidence for understanding the life of barred galaxies is to determine their stellar populations and recover their star formation histories. Unfortunately, there are very few stellar population analyses performed in the disc region of spiral galaxies, mainly due to the complex structures that meet there (e.g., disc, spiral arms, dust lanes, or bars) and the difficulties of disentangling the ages and metallicities of the different components, affected by strong degeneracies.

Gadotti & de Souza (2006) analyse the ages of a sample of bars simplifying the problem by assuming that colours are tracers of ages. However, they do not take into account the metallicity or dust extinction, which strongly affect broad-band colours. Absorption line-strength indices are, on the contrary, insensitive to dust effects (MacArthur, 2005), and therefore they represent a better way to analyse the stellar populations of disc galaxies. Other attempts to estimate ages without the measurement of line-strength indices include the work by Gadotti & de Souza (2005), who develop a diagnostic tool based on the assumption that bars are formed in vertically thin discs.

Pérez et al. (2007) and Pérez et al. (2009) finally deal with the challenge of measuring absorption line-strength indices along the bars for a sample of early-type spirals. They carefully analyse the age, metallicity, and α-enhancement radial profiles along the bars, obtaining very interesting and surprising results. In fact, Pérez et al. (2007) and Pérez et al. (2009) find variations in the line-strength measurements which are translated into positive, negative, and even zero metallicity gradients along the bars. This result led the authors to divide the galaxies in three main types and study their properties. They found that galaxies with negative metallicity gradients also show young ages and the lowest stellar maximum velocity dispersion values, while galaxies with positive metallicity gradients are older and present higher velocity dispersions. The third case, i.e., galaxies with zero metallicity variations, turn out to have a negative gradient in age in many, although not all, the cases. Figure 1.8 shows an example for each type of barred galaxy.

The results obtained by Pérez et al. (2007) and Pérez et al. (2009) are difficult to interpret. By means of numerical simulations, Friedli et al. (1994, see also Wozniak, 2007) had studied the influence of gas flows driven by bars in the abundance gradients; they concluded that the stellar metallicity profile tends to be flattened with time due to the mixing induced by the bar. Therefore, bars with zero metallicity gradients are easily understood as the expected evolution of a barred galaxy, whereas the negative gradients might be the relic of the

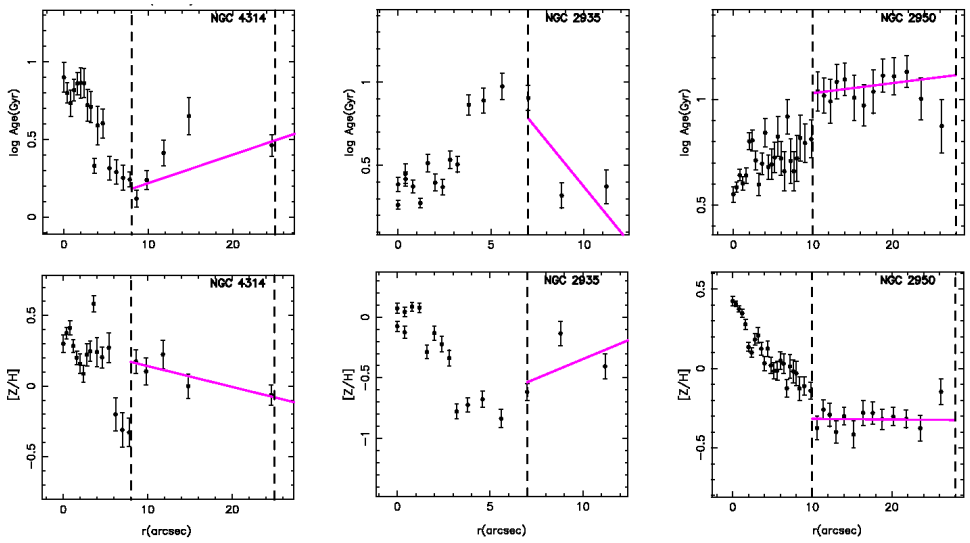

FIGURE 1.8— Age (top) and metallicity (bottom) gradients along the bars of three early-type galaxies: NGC 4314 (left panels), NGC 2935 (middle panels), and NGC 2950 (right panels). The vertical dashed lines indicate the beginning (and end, when present the second line) of the bar regions. A linear fit of the corresponding parameter within the bar-dominated region is plotted in fuchsia. NGC 4314, NGC 2935, and NGC 2950 show negative, positive, and zero metallicity gradients, respectively. *Figure taken from Pérez et al. (2009).*

expected trend for the disc (e.g., Yoachim & Dalcanton, 2008), especially if it is assumed that these bars have formed recently so the effects of the mixing are not relevant. However, the positive metallicity gradients represent a challenge for the present theories on bar formation and evolution.

In the last years the use of full-spectrum fitting techniques has gained relevance with respect to the measurement of the line-strength indices for studying stellar populations. Sánchez-Blázquez et al. (2011) apply this method to a small sample of barred galaxies in order to investigate their formation histories. When comparing the age and metallicity gradients along the bars and the disc major axis, they find significant differences. In fact, the stellar population properties of the bar resemble very well those of the bulge region. Sánchez-Blázquez et al. (2011) conclude that, at least for some of the bars studied, these are old, long-lived structures.

Although the results obtained so far for the stellar populations of barred galaxies are promising and provide important clues on the formation and evo-

lution of these structures, much work is still needed to finally reconstruct the true picture.

1.3.5 The role of bars in secular evolution

As introduced in Section 1.2, bars are intimately related to the internal secular evolution of galaxies and the formation of bulges. In fact, the non-axisymmetric nature of bars and their high frequency of appearance (see Section 1.3.1) imply that these structures are the main drivers of structural evolution in disc galaxies. Bars are responsible for the angular momentum exchange between the baryonic and dark matter components (Debattista & Sellwood, 1998, 2000; Athanassoula, 2003; Sellwood, 2006; Sellwood & Debattista, 2006), especially efficient at the locations of the resonances (Athanassoula, 2003; Martinez-Valpuesta et al., 2006). Moreover, they are capable of transporting material towards the central regions of galaxies, since the gravity torques induced by a bar can promote the gas inflow along it (Pfenniger & Norman, 1990; Combes et al., 1990; Friedli & Benz, 1995). Hence, gas concentrates at the centres, where it may trigger star formation and, in turn, form new structures, such as rings (Muñoz-Tuñón et al., 2004), bulges (Kormendy & Kennicutt, 2004; Boone et al., 2007), or even new bars (Erwin, 2004, see Section 1.4 for a review on this topic). Moreover, bar-driven structural evolution of disc galaxies would produce significant kinematical and morphological changes, as it may increase the bulge-to-disc light ratio, which in turn could lead to a parallel evolution along the Hubble sequence (Pfenniger & Norman, 1990; Friedli & Martinet, 1993, see also Section 1.1).

The role of bars in the formation of new structures is directly related with their own evolution, as the inflow process can contribute to the bar destruction. It has been theoretically proved that very massive central material concentrations may, together with the angular momentum exchange induced by the bar, dissolve it in rather short timescales ($\sim$2 Gyr; see for example Bournaud & Combes, 2002). However, given the observational evidence and the results from many numerical simulations, bars are thought to be long-lived structures (e.g., Debattista & Sellwood, 2000; Athanassoula & Misiriotis, 2002; Martinez-Valpuesta et al., 2006), despite the combined effect of the gas flow and the central mass concentrations (Berentzen et al., 2007).

It is thought that bulges formed secularly through the transformation of bars are disc-like, whereas classical bulges are formed during monolithic collapse or major merging (Kormendy & Kennicutt, 2004, but see also Section 1.2). Classical bulges are considered to be analogous to elliptical galaxies, as both show strong correlations of their properties with the maximum velocity dispersion; moreover, their stellar population properties are similar (e.g., Goudfrooij et al.,

1999). In fact, classical bulges are mainly old structures (MacArthur et al., 2009, see also Morelli et al., 2008), which suggests there is little or no influence of discs, and therefore of bars, in their formation. Even so, ellipticals and classical bulges are not completely equivalent, as pointed out by Proctor & Sansom (2002), Falcón-Barroso et al. (2002), or Ganda et al. (2007). It is in general difficult to compare a structurally complex system such as a disc galaxy with an elliptical; the overlapping of components in the central regions of a spiral, where bulge, disc, and other structures such as bars coexist, may disguise the actual properties of their bulges (Peletier et al., 2007).

There have been only a few attempts to compare bulges of barred and non-barred galaxies, in order to find clues about the role of secular evolution in their formation. Moorthy & Holtzman (2006) analyse a sample of face-on spirals and obtain a trend toward younger ages for the bulges of barred galaxies; on the contrary, Jablonka et al. (2007) find no differences between the stellar population properties of edge-on barred and non-barred galaxies. Pérez & Sánchez-Blázquez (2011) study the bulge properties of a sample of early-type galaxies hosting bars, finding significant differences with respect to their unbarred counterparts, the former being more metal-rich and slightly more α-enhanced. The metallicity of the bulge is very similar to that of the bar, and Pérez & Sánchez-Blázquez (2011) conclude that both structures form simultaneously but with different episodes of star formation. Finally, Coelho & Gadotti (2011) compare the age and metallicity values for a sample of bulges hosted by barred and non-barred galaxies; their results suggest that bars do affect the mean stellar age of bulges, so bars would actually trigger the star formation at the centres of their galaxies.

Gas inflow is not the only mechanism through which a barred galaxy can contribute to the formation of central structures. In fact, the inner regions of a bar may inflate after some rotations due to bending instabilities also known as vertical *buckling* instabilities, which produce an increase of the bar thickness and vertical velocity dispersion (Combes & Sanders, 1981; Combes et al., 1990; Bureau & Freeman, 1999; Athanassoula, 2003; Debattista et al., 2004, 2006). This process usually causes a secular growth of the bar which, in turn, induces a second buckling instability which may finally result in the appearance of the so-called *boxy/peanut/X-shaped* bulges (Martinez-Valpuesta et al., 2006, see Figure 1.9).

Boxy/peanut bulges have been found in $\sim$45% of edge-on spirals (Lütticke et al., 2000, see also Bureau et al., 2006) and have been also detected in face-on galaxies (Méndez-Abreu et al., 2008b) thanks to a kinematic diagnostic (Debattista, 2003). This kind of method is necessary because for low inclinations

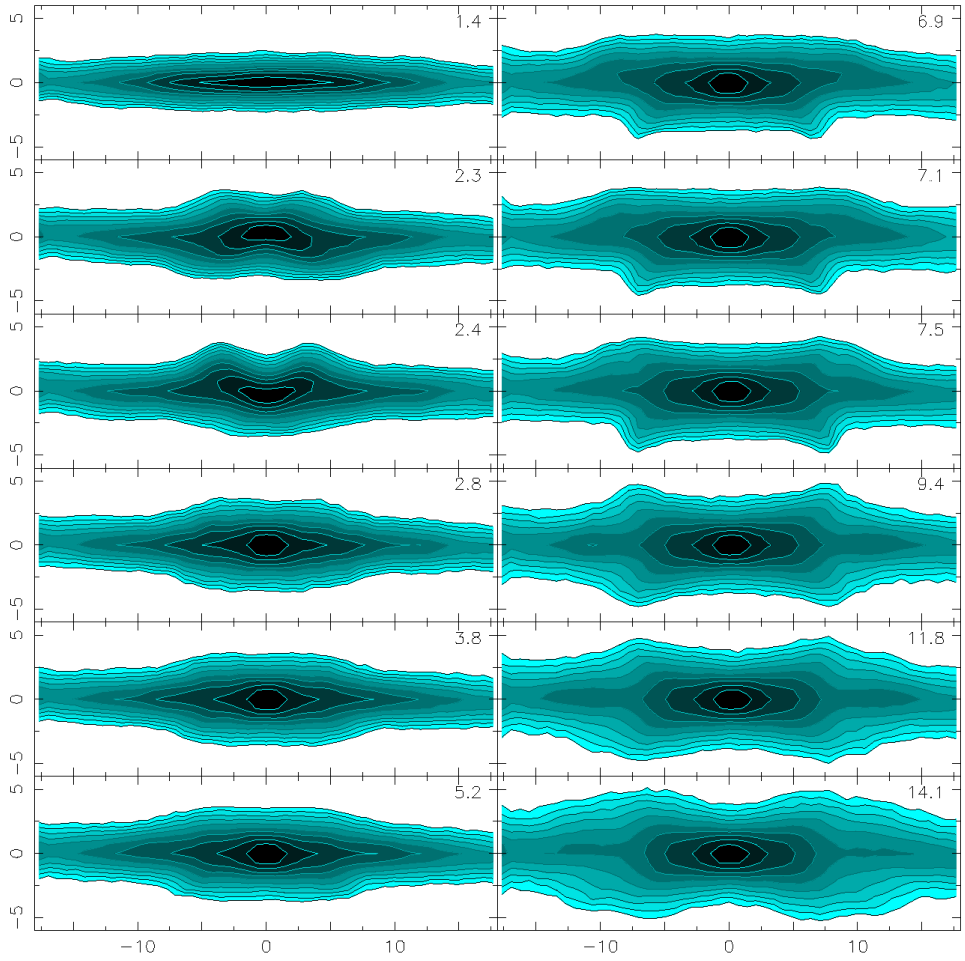

FIGURE 1.9— Simulation of the vertical evolution of a bar, seen edge-on along the bar minor axis. The upper right corners of each frame indicate the time in Gyr, so the sequence is from top to bottom in each column. The two buckling instabilities happen at ∼2.4 and ∼7 Gyr, respectively. Note the final appearance of a boxy/peanut bulge. The lengths are given in kpc and the isodensity contours are overplotted. *Figure taken from Martinez-Valpuesta et al. (2006).*

the boxy/peanut structure is projected on the disc plane, where it is completely masked. Since this kind of bulges are formed directly from the bars, their structural and kinematical properties should resemble very well those of the bar, as confirmed by observations (e.g., Bureau & Freeman, 1997, 1999; Chung & Bureau, 2004) and numerical simulations (Bureau & Athanassoula, 1999, 2005).

Definitely, bars are responsible for the formation of a variety of structures in the central regions of disc galaxies, and are able to even give rise to a secondary, smaller, inner bar.

1.4 Two better than one: double-barred galaxies

The particular case of double-barred galaxies, i.e., galaxies which host not only one, but two stellar bar structures at their centres (see Figure 1.10 for a schematic view of this kind of galaxies), has turned out to be of great relevance for the secular evolution theories of disc galaxies. Double bars have been studied mainly through numerical simulations or photometric observations, but the results obtained so far have highlighted the importance of spectroscopic analyses in order to determine the role of inner bars in galaxy evolution. In this Section we review the characteristics observed so far for these complex systems and the hypothesis proposed from the results of the theoretical works on the particularly efficient transport of material through nested bars towards the very central regions of galaxies. Moreover, we will show that inner bars are also related to the feeding of active galactic nuclei (hereafter AGNs) and that, from an evolutionary point of view, two bars might be better than just one bar.

1.4.1 Double bars frequency and photometric properties

Double bars were first discovered as isophotal twists in the photometric optical analysis at the centre of barred galaxies. Later on, deeper observations at higher spatial resolution revealed that these twists appeared due to the existence of an inner, secondary stellar bar structure, embedded in the main, larger bar (e.g., Friedli & Martinet, 1993; Wozniak et al., 1995; Laine et al., 2002).

The main photometric techniques employed for the search of structures in the central regions of disc galaxies are the isophotal fits to ellipses, as in the case of single-barred galaxies explained in Section 1.3.2 (e.g., Jungwiert et al., 1997), or different filtering procedures, as the widely used unsharp masking (Erwin & Sparke, 2003). The unsharp masking technique consists in applying a high-pass filtering to the optical or infrared images, so the low-frequency variations, which correspond to large-scale structures, are suppressed. This smoothed model is then subtracted from or divided into the original image, so

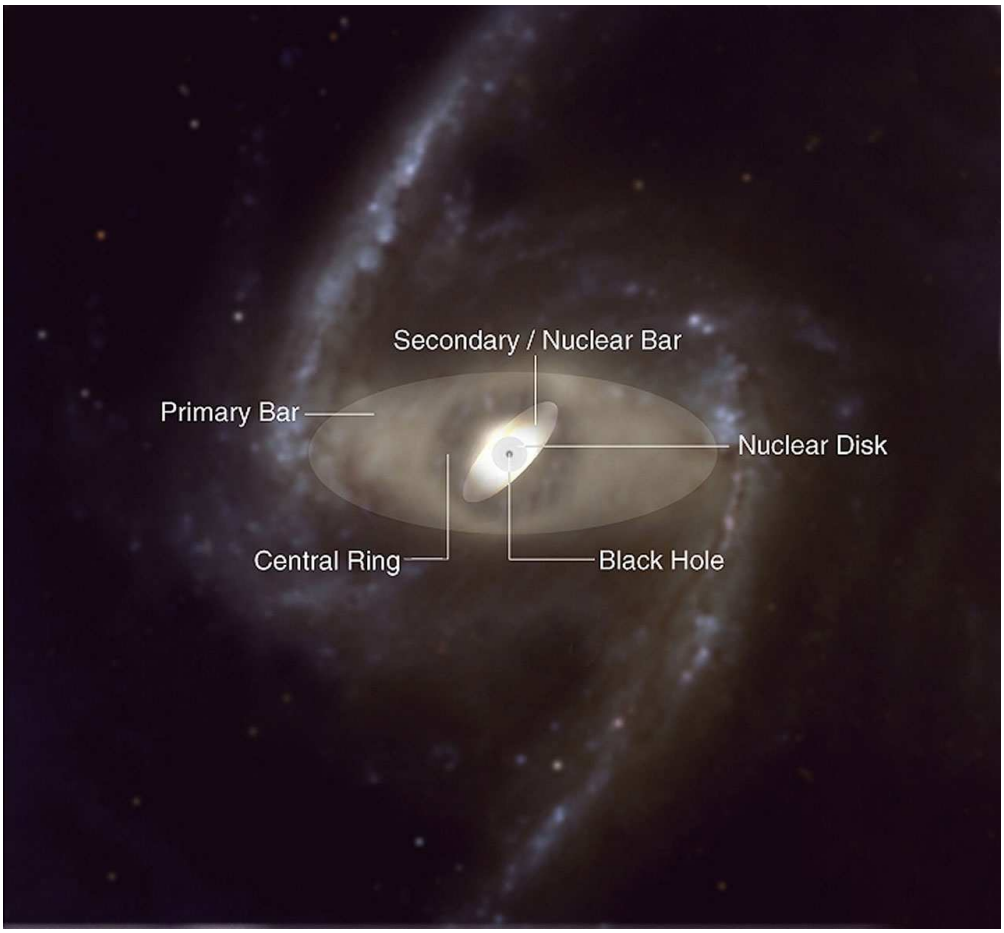

FIGURE 1.10— Schematic view of a double-barred galaxy and its different structural components. In this thesis, we will usually refer to the primary and secondary bar as *main* or *outer*, and *inner* bars, respectively. The presence of nuclear discs, black holes, or central rings depends on each galaxy and its properties, although double-barred galaxies are rather complex structures in general and tend to show many other components apart from the two bars, disc, and bulge. *Credit: ESO.*

the remaining unsharp mask is again added to or multiplied by the original to get the final sharpened image. This method is very sensitive to the small-scale, high frequency structures, allowing the detection of small bars embedded in the bulge or main bar light. Figure 1.11 illustrates the power of this technique in detecting inner structures.

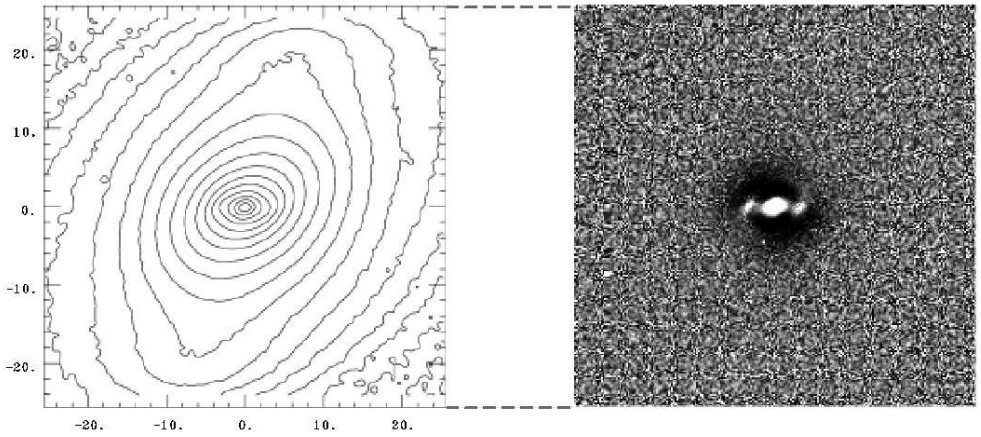

FIGURE 1.11— Example of an unsharp masking for the case of the double-barred early-type galaxy NGC 2950. Left: isodensity contours of an R-band image of NGC 2950. The x- and y-axes indicate the lengths in arcsec. Right: unsharp mask highlighting the presence of the inner bar. *Figure taken from Erwin & Sparke (2003).*

To date, ∼30% of local barred spirals have been found to host at least one inner bar (e.g., Moiseev, 2001; Erwin & Sparke, 2002; Laine et al., 2002; Erwin, 2004), and there is the particularly remarkable case of the early-type galaxy NGC 2681, which is believed to present three nested bars (Erwin & Sparke, 1999, 2003). Therefore, double bars are rather common systems, and a double-barred galaxy has been observed even at $z \sim 0.15$ by Lisker et al. (2006). Given the difficulty of detecting such small structures embedded in the light of other components, such as the bulge or the main bar, it is reasonable to conclude that the double bar fraction may be even higher in both the local and high-redshift Universe.

Double bars have been observed to be randomly oriented relative to each other (Friedli & Martinet, 1993; Wozniak et al., 1995). Moreover, it seems there is no correlation between the presence of an inner bar and the Hubble type of the host galaxy or its main bar properties. Inner bars usually do not span beyond the location of the ILR of the main bar (Shlosman et al., 1989). Erwin & Sparke (2002) find that inner bars extend to ∼12% of the outer bar size, and that they have in general smaller ellipticities; however, this result may be distorted by the fact that the inner bar might be embedded in the bulge light,

which tends to be rather round.

1.4.2 Dynamics: the loop concept and multiple pattern speeds

The fact that the two bars of a double-barred system are randomly oriented (Friedli & Martinet, 1993; Wozniak et al., 1995, see Section 1.4.1) suggests that they rotate independently, as predicted by numerical simulations (Shlosman & Heller, 2002; Debattista & Shen, 2007) and confirmed by some observations. In fact, the attempts to observationally disentangle multiple pattern speeds for the case of multiple-barred galaxies are sparse, with the notable exceptions of the analyses by Corsini et al. (2003), Maciejewski (2006), and Meidt et al. (2009). These works make use of different modifications of the traditional Tremaine-Weinberg method defined in Section 1.3.3 in order to analyse the secondary pattern speed introduced by the inner bar.

Only in the case of exactly perpendicular double bars, both pattern speeds may be equal, with the inner bar dynamics dominated by the x_2 orbits of the main bar. Any other configuration would produce the alignment of both bars due to gravitational torques, so they would merge into one single bar (Friedli & Martinet, 1993). Moreover, bars usually rotate in the same direction, even though merging processes could generate counter-rotating stellar bars (Sellwood & Merritt, 1994).

The complex stellar dynamics of a bar-within-bar system was finally simplified by Maciejewski & Sparke (1997, 2000), who developed a simple formalism to study the orbits of their stars based on the *loop* concept. As explained in Section 1.3.3, the dynamics of a single bar can be described by two fundamental frequencies, corresponding to the bar and free oscillations, respectively. However, a double-barred potential needs an additional frequency related to the secondary bar, so there are three fundamental frequencies in total, which prevents the existence of closed orbits. The *loop* is therefore defined as a family of orbits whose populating particles return to the same curve when the two bars recover the same relative position between them, but each individual particle is not in the same initial place. Although a loop is not exactly a closed orbit, it is stable and its global shape is preserved. Numerical simulations have even found loops families analogous to the x_1 and x_2 orbits of a single-barred potential, i.e., parallel and perpendicular to the main bar, respectively. These families are characterised by showing just two fundamental frequencies corresponding to the two bars, since there are no free oscillations between them.

It is interesting to note that many numerical works find that inner bars tend to rotate faster than main bars (e.g., Heller & Shlosman, 1994; Debattista &

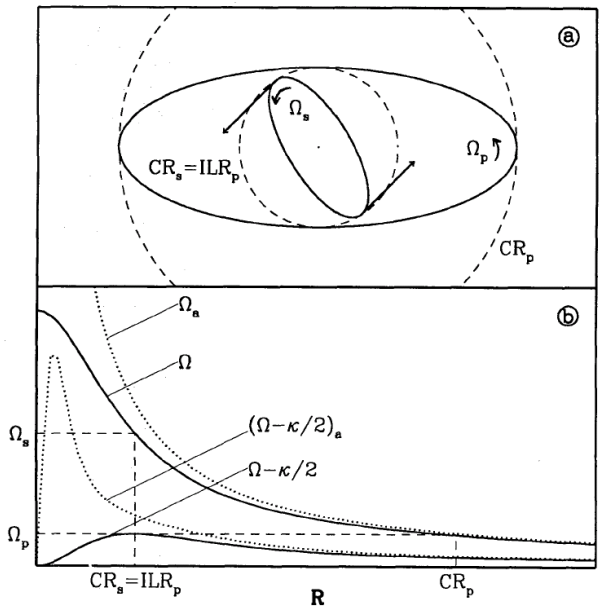

FIGURE 1.12— Scheme of a double-barred galaxy and its resonances. The top panel shows the main (p) and inner (s) bars rotating independently, with pattern speeds Ω_p and Ω_s, respectively. The dashed lines mark the location of the resonances, with the CR radius of the inner bar (CR_s) at the same location of the main bar ILR (ILR_p). The outer bar does not extend beyond its CR radius (CR_p). The bottom panel shows the resonances diagram for the two-bar system: the outer bar presents only one ILR, whereas there are two for the inner bar. *Figure taken from Friedli & Martinet (1993).*

Shen, 2007; Heller et al., 2007), as the orbits become stable when the CR of the inner bar is coincident with the ILR of the main bar (Friedli & Martinet, 1993, see Figure 1.12 for a schematic view of the resonances in a double-barred potential). This result is also backed by the determination of the two pattern speeds in NGC 2950 performed by Corsini et al. (2003), or by the evidence found by Emsellem et al. (2001) in a sample of four double-barred galaxies. However, stable loops appear only when inner bars are slow, i.e., much smaller than their CR radii (Maciejewski & Sparke, 2000).

1.4.3 Kinematical analyses of double-barred galaxies and the discovery of the σ-drops

As mentioned, most of the works devoted to the study of double-barred galaxies have been purely theoretical or based only on photometric observations.

This bias is mainly due to the difficulties inherent in the complex structure of these objects, which require time-consuming spectroscopic observations and a spectral analysis full of demanding details. Therefore, there is a notable lack of kinematical and stellar populations analyses of double-barred objects. Concerning the former topic, it is important to highlight the works by Emsellem et al. (2001), Moiseev (2001), and Moiseev et al. (2004).

Moiseev (2001) and Moiseev et al. (2004) analyse a sample of candidate double-barred galaxies observed with the `MPFS` integral-field spectrograph attached to the BTA-6 m telescope in Russia, complemented with Fabry-Perot observations carried out at the same telescope. Hence, the authors recover not only the stellar and gaseous kinematical information, but also the spatial distribution of the kinematic parameters, such as the line-of-sight velocity and velocity dispersion. Interestingly, Moiseev et al. (2004) conclude that the great variety of structures revealed by the kinematic maps (e.g., inner discs or gas counter-rotating) are exclusively due to the presence of the main bar and completely independent from the inner bar. The inner bar therefore does not affect any of the stellar kinematical parameters, neither velocity nor velocity dispersion, and it is considered a rare phenomenon which only shows up in photometric analyses.

The work presented by Emsellem et al. (2001) is particularly noteworthy since it led to the discovery of the so-called σ-drops at the centre of the spiral galaxies. In fact, Emsellem et al. (2001) observed four double-barred galaxies using long-slit spectroscopy, with the slit placed parallel and perpendicular to the inner bar for each case, and noticed that for three out of the four galaxies the velocity dispersion profiles showed a significant local minimum exactly at the centre (see Figure 1.13). Similar features had already been detected in the non-barred galaxy NGC 6503 by Bottema (1989) and Bottema & Gerritsen (1997), and since 2001 many other works have confirmed that they are not so rare a phenomenon, including in double-barred systems. Hence, Falcón-Barroso et al. (2006) find this signature in at least 46 % of a sample of 24 early-type spirals, and other cases have been noticed in different samples (e.g., Márquez et al., 2003; Ganda et al., 2006), specially in barred and Seyfert (Comerón et al., 2008) galaxies.

The origin of the σ-drops is usually related to the presence of a cold, newly formed stellar component, such as an inner disc: the stars retain the kinematical properties of the gas they are formed from, and since the dissipative nature of the gas is more efficient at the highest densities of the central regions, the final stellar component is cold, with velocity dispersion values lower than their surroundings (Wozniak et al., 2003; Wozniak & Champavert, 2006). However,

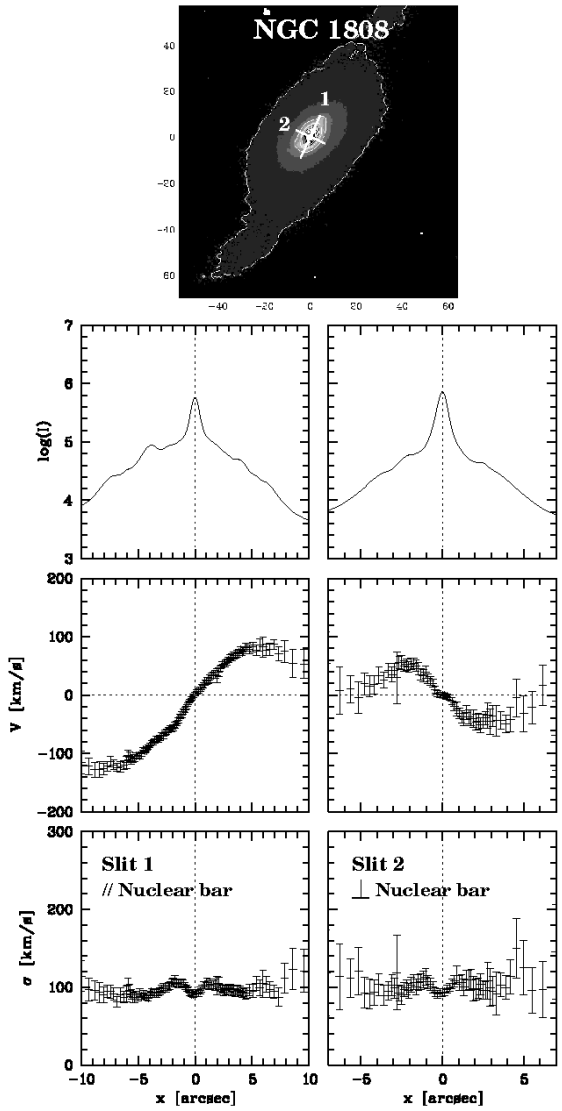

FIGURE 1.13— Kinematical analysis of the double-barred galaxy NGC 1808. The top near-infrared image indicates the positions and lengths of the two slits used for the study, parallel and perpendicular to the major axis of the inner bar. North is up and East is left. The plots correspond to the luminosity (top panels), velocity (middle panels), and velocity dispersion (bottom panels) profiles along the two slit directions (left and right, respectively). The velocity dispersion profiles clearly show the σ-drops at the centres. *Figure taken from Emsellem et al. (2001).*

Bureau & Athanassoula (2005) succeed at reproducing σ-drops in purely stellar simulated bars, since the x_1 orbits tend to be rounder at the central regions thus inducing a decrease in the velocity dispersion values there.

1.4.4 Stellar populations: no conclusions so far

If stellar population studies of single-barred galaxies are sparse, analogous studies focused on double-barred galaxies are almost nonexistent. To date, there are very few stellar population studies involving double bars, all of them being projects devoted to the analysis of samples of barred galaxies in general, which include only some double-barred objects. These works focus only on the main bar and they do not study the inner bar. This is the case in the set of papers by Pérez et al. (2007, 2009), Pérez & Sánchez-Blázquez (2011), and Sánchez-Blázquez et al. (2011), already detailed in Section 1.3.4. 40% of their barred galaxy sample are actually double-barred galaxies (i.e., 8 out of the 20 galaxies of their sample). However, there are no relevant correlations within the results they find and the presence of inner bars: 50% of their double-bars turn out to show positive age gradients, and also 50% present positive metallicity gradients, which indicates there is not a clear trend for double-barred objects with respect to those with single bars. The implications of these results within evolutionary scenarios is still unclear; however, specific analyses of inner bars and comparison with single- and non-barred galaxies are mandatory to disentangle their stellar population properties.

1.4.5 How are double-barred galaxies formed? Their role in secular evolution

How a double-barred system is born and how it evolves during the galaxy lifetime is one of the most intriguing and also studied topics concerning galaxy structure and evolution. The challenge of building long-lived double bars has been the motivation for many numerical simulations but, despite the variety of observational evidence gained during the years, the true scenario is still not clear.

The most accepted hypothesis is that the outer bar appears first, so the gas flows along it and it is finally captured by its x_2 orbits, subsequently forming the dynamically decoupled inner bar structure. In this scenario the dissipative component plays a major role, as backed by the numerical works of Friedli & Martinet (1993), Shlosman & Heller (2002), or Englmaier & Shlosman (2004). For example, Heller et al. (2001) pay attention to the gas viscosity at the ILR location of the main bar and conclude that this gas is responsible for the dynamical decoupling of the gaseous, slower inner bar with respect to the main

bar potential. A different way of proceeding is the work by Rautiainen et al. (2002), who include the gas as inelastically colliding particles in their N-body simulations. Interestingly, a fast-rotating inner bar shows up in a purely stellar disc without a major contribution of the gas component. Finally, Heller et al. (2007) generate a two bar system within a dark matter halo thanks to its tidal torques. Both bars are gas-rich and short-lived, since the interaction of several non-axisymmetric components weakens the bars and finally dissolves them.

Only Debattista & Shen (2007) are able to create a purely stellar inner bar without any dissipational process at all, from pure collissionless N-body simulations. These inner bars are formed before the appearance of the outer bars although this time sequence is probably a consequence of the peculiar initial conditions imposed by the authors in their simulations. In fact, Debattista & Shen (2007) warn that in the real Universe it is more probable that inner bars appeared after, and thanks to, the main bars. Moreover, the simulations by Debattista & Shen (2007) need the presence of a rapidly rotating structure at the centre of the galaxies, such as a disc-like bulge (or pseudobulge) or an stellar inner disc, for the inner bars to be formed.

In general, all the numerical simulations involving gas finally create inner bars which are very efficient at transporting material to the central regions of disc galaxies (Friedli & Martinet, 1993; Heller et al., 2007). In fact, the gas flow may be transferred from the outer to inner bars and, although the outer regions of both structures tend to be gas depleted, the flow inside the bars is very important and with little or no dissipation (Shlosman & Heller, 2002). Hence, as their single-barred analogues do, double-barred systems may contribute to the formation of new structures and therefore to the secular evolution of their host galaxies (Pfenniger & Norman, 1990).

It has been theoretically demonstrated that the flow of gas through a single bar stops before reaching the galactic centre, at a distance of $\sim$100 pc (Boone et al., 2007); however, a system of nested bars may efficiently transport the material to the nuclear regions, where it even would help to fuel nuclear activity, as proposed by Shlosman et al. (1989), Shlosman et al. (1990), and Friedli & Martinet (1993). Although this hypothesis is very promising, there have been several observational studies devoted to test it and the results obtained so far are still not determinant (e.g., Ho et al., 1997; Márquez et al., 2000, but see also Moles et al., 1995).

With these pieces of evidence, it is clear that double-barred galaxies are the perfect benchmark to constrain the role of secular processes within galaxy nuclei. The only way to estimate the formation histories of theses systems

is to perform a detailed kinematic and stellar population analysis: if double bars are playing a major role in galaxy evolution, this fact will be reflected in the properties (star formation, age, and metallicity) of the galaxy components (bulge, inner bar, outer bar, and disc), resulting in a gradient of ages and metallicities between them. However, this is difficult to achieve due to the structural complexity of galaxies with nested bars, as illustrated by the lack of this kind of spectroscopic studies (see Section 1.4.4).

1.5 Spectroscopic analysis: long-slit vs. integral-field

To achieve a detailed picture of the kinematics and stellar population properties of double-barred galaxies from an observational point of view, spectroscopic analysis is fully demanded. In fact, only spectra contain information on the line-of-sight stellar velocity distribution, as well as of the star formation history and chemical evolution of a galaxy. However, spectrographs scatter the light from the galaxy thus providing signal-to-noise (S/N hereafter) ratios rather lower than those from broad-band images, making it difficult to accomplish the high-quality requirements needed for a detailed stellar population study.

The most widely used strategy to get spectra from a galaxy is to use the long-slit technique: since spectroscopy is based on the light dispersion in different wavelengths, a *one-dimensional* slit is positioned in the focal plane in front of the dispersor element in order to avoid the mixing of information due to spectra overlapping on the CCD. Therefore, long-slit spectrographs miss one of the two spatial dimensions of the projected sky, as the resulting image on the detector contains just one spatial direction and one wavelength direction. Hence, in order to analyse both the inner and outer bars of a double-barred galaxy with a long-slit spectrograph, it is necessary to place the slit along both major axes, thus increasing the amount of time needed to carry out such observations.

However, double-barred galaxies are structurally complex and the spatial distribution of their properties might also provide important clues on their formation and evolution. The transition regions between components, such as those between the main bar and the disc or between the two bars themselves, are specially interesting since they might locate new structures (e.g., the ansae, see Section 1.3.2) or provide relevant information related to the dynamics or the efficiency of the gas transference. Moreover, gradients of different parameters, such as velocity dispersion, age, or metallicity, along directions parallel and perpendicular to the major axes of the bars, also provide clues about their role in the angular momentum exchange and material migration.

The natural evolution of the spectroscopic techniques has been conducted towards strategies which allow the observation of the missed spatial information, such as moving the slit to map the desired field-of-view (e.g., Wilkinson et al., 1986), or tuning the etalon of a Fabry-Perot interferometer to map the spectrum (e.g., Tully, 1974; Mayya et al., 2012). However, these methods introduce an additional dimension: the time. Nowadays the use of the so-called *integral-field* spectrographs is of growing importance: these instruments include a variety of optical elements in order to store both the spatial and wavelength information of a single pointing of the telescope on the two-dimensional detectors. In fact, they are composed of a traditional spectrograph together with an *integral-field unit* (IFU hereafter), which spatially rearranges the image in order to pack the spectra from all the spatial elements (known as *spaxels*) inside the CCD. Therefore, during the reduction process the information on the CCD can be properly extracted and rearranged in a data cube with two spatial and one spectral dimensions. IFUs usually work in the optical and near-infrared spectral ranges, although their use is extending towards the middle-infrared.

Taking into account the way IFUs rearrange the spatial information, these instruments are classified in three main classes. A schematic view of them can be found in Figure 1.14:

- ***Lenslet arrays.*** The image is projected onto a microlens array which sections the field-of-view into a set of spaxels whose light is collimated into several micropupils and introduced into the spectrograph. In order to avoid the overlapping of the spectra on the detector, the dispersion direction is slightly angled with respect to the rows and columns of the array, as illustrated in Figure 1.14. Lenslet arrays are extensively used for integral field spectrographs since they provide a filling factor of 100%, i.e., they cover the full field-of-view. `SAURON` (Bacon et al., 2001, see Chapter 2 for a description of this instrument) and `OASIS` (Bacon, 1995), both mounted on the William Herschel Telescope (WHT, 4.2 m; La Palma, Spain), are two examples of integral field spectrographs working with lenslet arrays.

- ***Fibre beam.*** Light coming from each spaxel is introduced in an optic fibre and conducted towards the spectrograph. The most common procedure is to rearrange the two-dimensional field-of-view in a single line, thus simulating the traditional long-slit. The main disadvantage of this method is the loss of spatial information due to physical voids between fibres, so the typical filling factor of IFUs based on fibre beams is of $\sim$65%. For this reason, a lenslet array is usually placed in the focal plane in order to fit the total field-of-view at the entrance of the fibre spectrograph, as

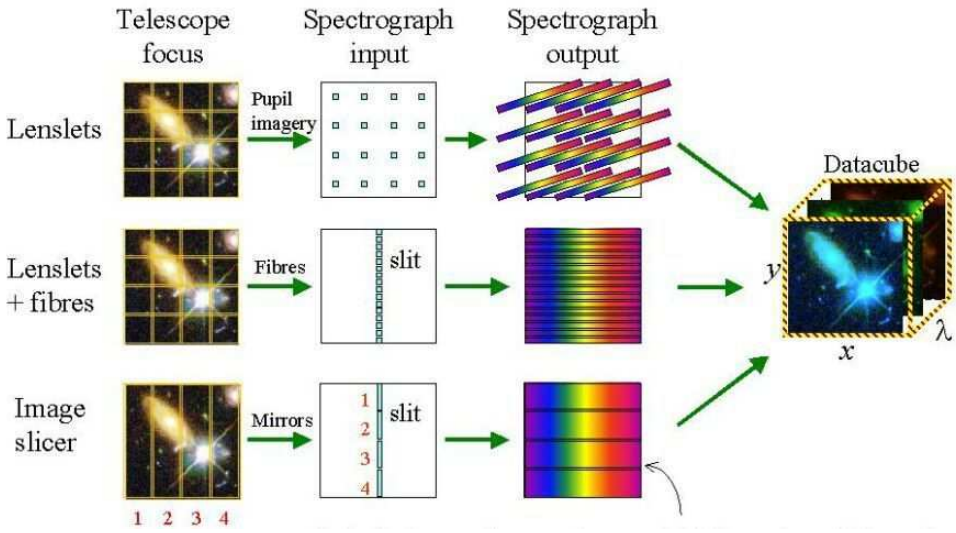

FIGURE 1.14— Scheme of the types of integral-field units (IFUs) used to create an integral-field spectrograph. The top row shows the case of a lenslet array, which sections the field-of-view in different spaxels that are collimated into the spectrograph. The dispersor element is angled to avoid the spectra overlapping on the CCD. The middle row shows a lenslet+fibres coupling, so the sectioned field-of-view is introduced in a fibre bundle which conducts the light towards the spectrograph. Finally, the bottom row shows a slicer which sections the field-of-view in several unidimensional slits and rearranges the image in a single long-slit, as if it was a traditional spectrograph. Once the information on the CCD is properly extracted, the data can be rearranged in a cube with two spatial and one spectral dimensions. *Credit: Centre for Advanced Instrumentation (CfAI), Physics Department, Durham (UK).*

seen in Figure 1.14. Some examples of integral-field spectrographs based on simple fibre beams are `HEXAFLEX` (Arribas et al., 1991) and `INTEGRAL` (Arribas et al., 1998), both developed by the *Instituto de Astrofísica de Canarias* and mounted on the Nasmyth focus of the WHT. `PMAS` (Roth et al., 2005), on the Cassegrain focus of the Calar Alto 3.5 m telescope (Almería, Spain), the two `GMOS` spectrographs (Allington-Smith et al., 2002), on the Cassegrain focus of each GEMINI telescope (8.1 m, Hawaii and Chile), `VIMOS` (Le Fèvre et al., 2003), on the Nasmyth focus of one out of the four VLT telescopes (8.2 m, Chile), and `FLAMES` (Pasquini et al., 2000), also in the VLT, are examples of integral field spectrographs which combine fibre beams with lenslet arrays.

- ***Slicers.*** This IFU sections the image in slices and places them in line

as they were a single, traditional long-slit, as explained in Figure 1.14 and done by SINFONI (Eisenhauer et al., 2003), which works in the near-infrared and is mounted on the Cassegrain focus of one of the VLT telescopes, or GNIRS (Allington-Smith et al., 2004), on the Cassegrain focus of the GEMINI-South telescope (Chile). As in the case of the lenslet array, the filling factor of a slicer is 100%.

Irrespective of which type of spectrograph is used, what the observer gets is what is stored on the restricted number of pixels of the CCD detector, which needs to include as many spectra as spaxels. Therefore, although IFUs allow us to recover both spatial and spectral information, the final amount of data is limited. There are four main parameters the developer of an integral-field spectrograph has to deal with: field-of-view, spatial resolution, spectral range, and spectral dispersion. The scientific goal of the instrument will determine which parameters will have the priority, so similar IFUs and spectrographs might finally provide very different data. Therefore, it is common that integral-field spectroscopic data present very short spectral ranges and small field-of-view (between $1\times1\,\mathrm{arcsec}^2$ and $10\times10\,\mathrm{arcsec}^2$); larger images would mean loss of spatial resolution or spectral dispersion. This characteristic usually makes observations with IFUs to be longer and more time-consuming than analogous observations with traditional long-slit spectrographs (if observing an object with the same surface brightness and getting the same S/N ratio).

Hence, the great advantage of the integral-field spectrographs, which is the spatial information they provide, is weakened by the variety of properties that are sacrificed with respect to their long-slit counterparts, which usually observe longer spectral ranges. The desired scientific goal to accomplish may require a certain observational strategy, or even a combination of the two, as in the case of double-barred galaxies. The thesis presented here illustrates how integral-field and long-slit spectroscopic data provide different and complementary information for studying double-barred galaxies. Whereas integral-field spectra allow us to analyse the spatial distribution of kinematical and stellar population properties of a limited region (including just the central structures), a long-slit analysis along the directions of the major axes of both bars provides a wide variety of spectral features, necessary to constrain the formation history of these objects, and allows us to reach outer regions in order to achieve a complete picture of the properties of double-barred galaxies.

To advance in the development of astronomical instrumentation it is necessary to solve the difficulties inherent in integral-field spectrographs and other strategies to recover both the spatial and spectral information from galaxies. Three-dimensional detectors, which can store these three dimensions without

the need of messing up the field-of-view and packing the spectra on a bidimensional CCD, would mean a great revolution for instrumental and astrophysical research. First steps have been given in this direction, with the development of detectors such as the *Superconduction Tunnel Junction* (STJ), *Kinetic Inductance Detector* (KID), or *Transition Edge Detector* (TES); however, all these instruments work at very low temperatures, below 1 K, so they require cryogenic techniques which make them more expensive and place them still outside the reach of the astrophysical community in general.

1.6 Goals and outline: questions asked and answers found

The present introduction has outlined the different theories that try to explain the formation of bulges and therefore the internal evolution of galaxies. Special emphasis has been put on the role of barred galaxies and double bars in particular, which have thought to be a most efficient way to transfer material to the very central regions of galaxies. By performing a brief review of the studies related to these objects in the literature, this chapter illustrates what we know but also, and more interestingly, how much we still do not know, about double bars. In fact, the present thesis is designed to be the natural link between what is suspected and what actually happens, so a sample of double-barred galaxies has been carefully observed and analysed in order to fully characterise their kinematics and stellar population properties. Therefore this work provides the detailed description of the observational characteristics of double-barred systems which is still missed in the literature, and presents several features never noticed or simulated before. Following the main goal of moving from theoretical hypothesis to observational evidence, we discuss the results in the framework of the different scenarios suggested for the formation of double-barred galaxies and we put constraints on their evolution.

Chapter 2 briefly describes the sample, observations, and long-slit and integral-field data reduction process, while some photometric analysis is performed in Chapter 3 in order to show the power of the data and to introduce several characteristics of the galaxies relevant for the work. The specific goals of this thesis are accomplished in the next Chapters as follows:

- Detailed characterisation of both stellar and gaseous kinematical properties and their spatial distribution for a sample of double-barred galaxies. This work is presented in Chapter 4.

- Detailed characterisation of the stellar population properties for a sample of double-barred galaxies. Determination of the age, metallicity, and α-enhancement distributions. Discussion on the different formation scenar-

ios of double-barred galaxies and on the role of inner bars in the formation of bulges. This work is presented in Chapter 5.

- Detailed characterisation of the stellar kinematics and stellar population properties of the double-barred galaxy NGC 357. One of the main goals of this thesis is to combine the information provided by the complementary integral-field and long-slit spectroscopic techniques. NGC 357 is the only galaxy of the sample analysed through long-slit data and therefore its analysis provides important and unique information on double-barred objects. Moreover, NGC 357 has revealed itself as a galaxy with a particular structural composition, which differs from the findings obtained for the rest of the double-barred sample. For all these reasons, the study of this object is discussed independently in Chapter 6.

The work presented in this thesis sheds light on the properties of double-barred galaxies and the way they form and evolve, and the main conclusions are collected in Chapter 7 (see Chapter 8 for the Spanish version of the conclusions). As expected, the results we have obtained lead to many questions that still need answers. The future of double-barred galaxies research is summarised in Chapter 9.

2

The galaxies: sample, observations, and reduction

The truth is out there
The X-files

Since double-barred galaxies are structurally complex objects, it is important to select the sample carefully and to use state-of-the-art techniques in their observation and data reduction, in order to achieve the precision in the detailed kinematics and stellar population analysis this thesis is aiming at. The present Chapter discusses the five double-barred galaxies which compose the sample and briefly describes the instrumental setup and weather conditions of the different observing runs carried out to collect the spectra. It also includes an outline of the reduction process followed for preparing the integral-field and the long-slit data for their later analysis.

2.1 The double-barred sample

The sample is composed by five double-barred galaxies selected from the catalogue of Erwin (2004), namely NGC 357, NGC 2859, NGC 3941, NGC 4725, and NGC 5850. Optical images for the five galaxies are shown in Figure 2.1. During the present work the five galaxies will be normally divided in two groups, attending to the technique used for their observations. In fact, NGC 2859, NGC 3941, NGC 4725, and NGC 5850 were observed with the `SAURON` integral-field spectrograph, whereas long-slit spectra for NGC 357 were taken with the `EMMI` instrument.

Several criteria were used when selecting the double-barred sample. The

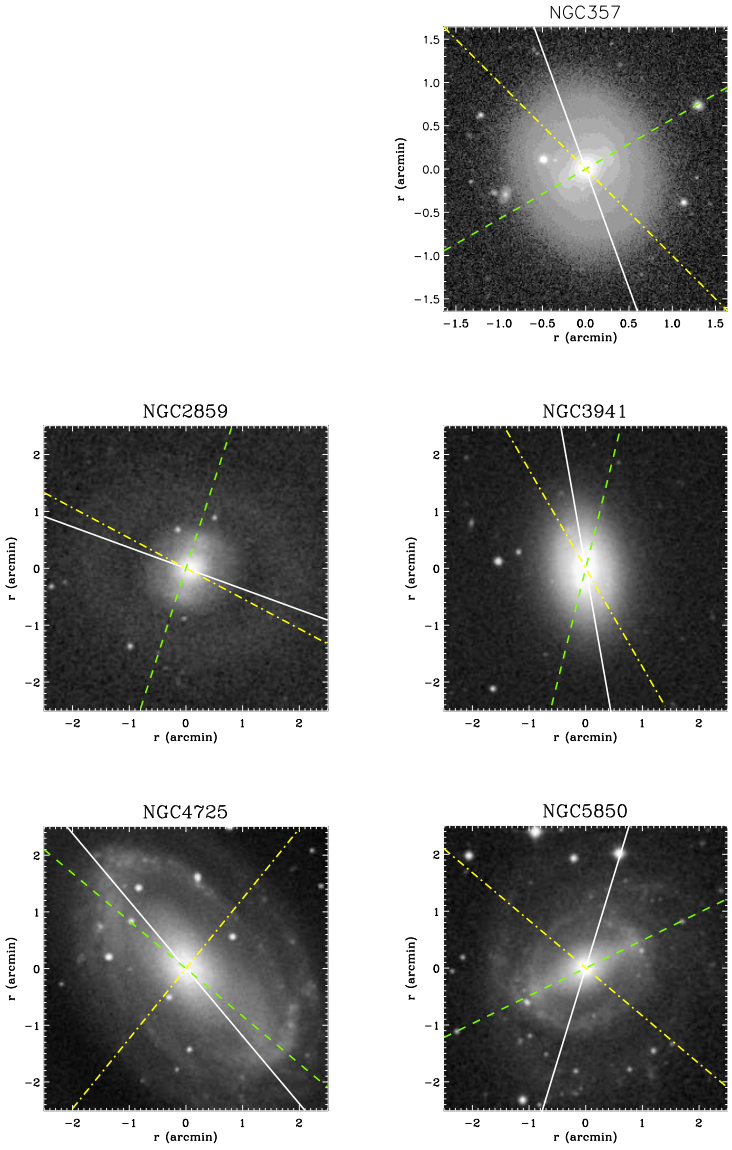

FIGURE 2.1— Optical images from the Sloan Digital Sky Survey (SDSS; York et al., 2000) for the five double-barred galaxies of the sample. Solid white, dashed green, and dash-dotted yellow lines indicate the directions of the galaxy disc, outer bar, and inner bar, respectively. North is up and East is left.

inclinations of the five galaxies deliberately range between 25° and 50°; these intermediate values allow us to recover the line-of-sight (LOS) kinematics, but the mixing of the components due to the LOS projection is moderate. Moreover, only early-type galaxies were considered in order to avoid additional handicaps for the stellar population analysis, such as complex spiral structures or the presence of dust. One of the main requirements for the selection was the length of the inner bars, since they had to be long enough to completely resolve them with the available instrumentation. For the particular case of the SAURON sample, we also took into account the size of the inner bars: we assured that they were big enough to be well mapped within the SAURON field-of-view (hereafter FoV), but they were also small enough to allow the mapping of the transition regions between the two bars. Note that the main bar is usually larger than the total FoV, as illustrated in Figure 2.2.

The bar lengths, ellipticities, position angles (hereafter PA), and other relevant properties for the sample galaxies are summarised in Table 2.1. It is worth noting that in Erwin (2004), which is our main reference for the sample selection, there is an erratum related to the PA of the inner bar of NGC 3941, which is estimated as 85°. The kinematical analysis of the σ-hollows performed in Chapter 4 allowed us to realise this mistake so we finally established a correct PA of 30° for NGC 3941, in agreement with the measurements of Erwin & Sparke (2003), who provide a value between 20° and 35°.

Taking into account the known correlation between the bar strength and ellipticity (Laurikainen et al., 2002, see also Section 1.3.2 in Chapter 1), and considering the low values of ϵ_{max} given in Table 2.1 for the five inner bars, it is also interesting to point out that our sample is composed mainly by weak inner bars.

NGC 3941 and NGC 4725 are Seyfert 2 galaxies (Véron-Cetty & Véron, 2006), whereas NGC 357 is classified as a LINER (Gadotti et al., 2007), and NGC 2859 and NGC 5850 present no signs of nuclear activity. Concerning the environment, the five galaxies were selected to be almost isolated. NGC 2859 and NGC 3941 are in fact field galaxies, whereas NGC 4725 and NGC 5850 belong to small groups. Although NGC 357 has been claimed to be isolated (e.g., Gadotti et al., 2007), van den Bergh (2002) finds it belongs to a group with at least six other members. However, it shows no signatures of interaction with its closer companions.

Finally, note that at the given distances compiled in Table 2.1 for the five galaxies, the corresponding spatial scales are $\sim$150 pc arcsec^{-1}, $\sim$120 pc arcsec^{-1}, $\sim$90 pc arcsec^{-1}, $\sim$60 pc arcsec^{-1}, and $\sim$140 pc arcsec^{-1} for NGC 357, NGC 2859, NGC 3941, NGC 4725, and NGC 5850, respectively.

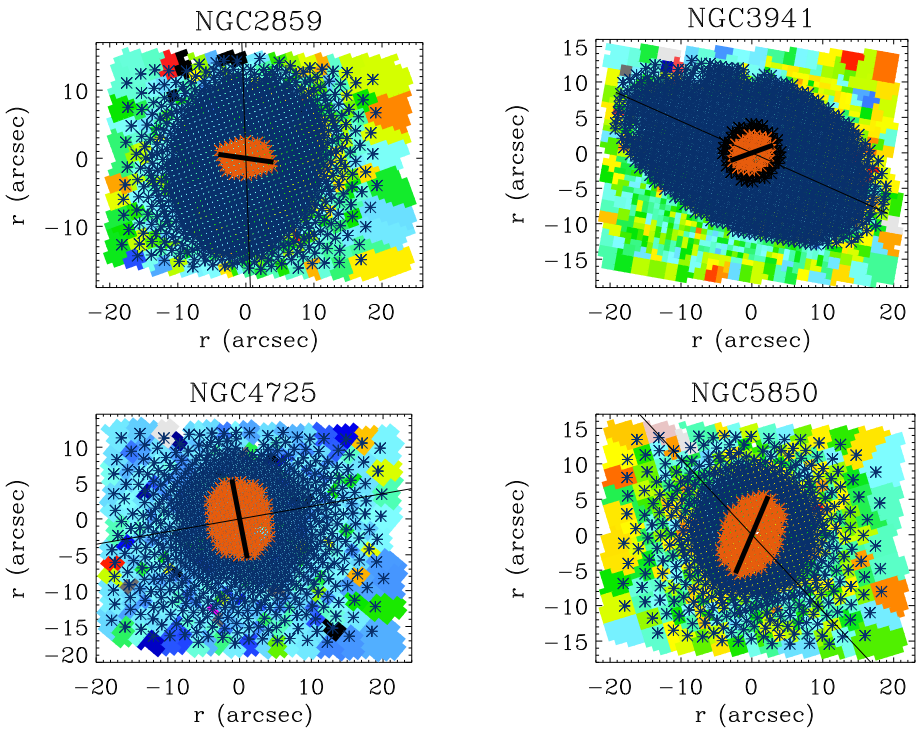

FIGURE 2.2— SAURON intensity maps (arbitrary units) for the four double-barred galaxies: NGC 2859, NGC 3941, NGC 4725, and NGC 5850. The bins corresponding to the inner (orange asterisks) and outer (blue asterisks) bars are identified. The outer bar is larger than the SAURON FoV for all the galaxies except NGC 3941, whose bars are completely mapped with these observations.

2.2 Observations and instrumental setup

As mentioned above, the data used for the present work are divided in two main sets, according to the observing runs carried out with two different telescopes. Integral-field spectra for NGC 2859, NGC 3941, NGC 4725, and NGC 5850 were obtained with the SAURON (Spectrographic Area Unit for Research on Optical Nebulae) spectrograph, attached to the William Herschel Telescope (WHT) at the Observatorio del Roque de los Muchachos (La Palma, Spain). NGC 357 was observed with the EMMI (ESO Multi-Mode Instrument) long-slit spectrograph, mounted on the New Technology Telescope (NTT) at the Observatorio de La Silla (Chile). In the following, we will describe the instrumental configuration used and the important remarks of both observing runs.

TABLE 2.1— Relevant properties of the double-barred sample.

	RC3 Type (1)	D (2)	i (3)	Position angle (4)			Semi-major axis (5)		ϵ_{max} (6)	
				Disc	Inner bar	Outer bar	Inner bar	Outer bar	Inner bar	Outer bar
NGC 357	SB(r)0/a	32.5 Mpc	36°	20°	45°	120°	3.1 arcsec	21 arcsec	0.16	0.44
NGC 2859	(R)SB(r)0^+	25.4 Mpc	25°	90°	62°	162°	4.1 arcsec	34 arcsec	0.31	0.40
NGC 3941	SB(s)0^0	18.9 Mpc	51°	10°	30°	166°	3.2 arcsec	21 arcsec	0.21	0.47
NGC 4725	SAB(r)ab	12.4 Mpc	42°	40°	141°	50°	5.6 arcsec	118 arcsec	0.20	0.67
NGC 5850	SB(r)b	28.5 Mpc	30°	163°	50°	116°	5.9 arcsec	63 arcsec	0.30	0.68

(1) Morphological type from de Vaucouleurs et al. (1991);
(2) distance to the galaxy, from Tully (1988);
(3) galaxy inclination, from Erwin (2004) (except for NGC 357, which is taken from Aguerri et al., 2005);
(4) position angle of the major axis (disc) and the two bars, taken from Aguerri et al. (2005) for NGC 357, Erwin & Sparke (2003) and the present kinematical analysis for NGC 3941, and Erwin (2004) for the rest of the galaxies;
(5) bar lengths, estimated as the semi-major axes of maximum isophotal ellipticity, from Erwin (2004);
(6) maximum isophotal ellipticity of the bars ($\epsilon = 1 - b/a$), from Erwin (2004).

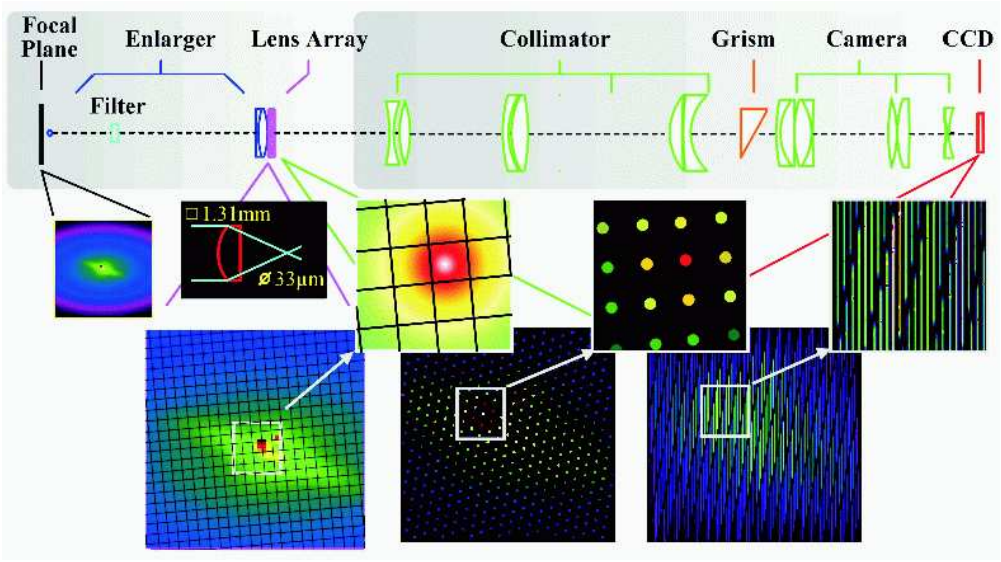

FIGURE 2.3— SAURON optical design: the lenslet array divides the FoV into several spatial elements or spaxels, whose light is collimated and then transported towards the grism. The enlarger aims at adjusting the FoV at the focal plane to the physical size of the lens array. The final dispersion direction is angled with respect to the dimensions of the CCD in order to avoid the spectra overlapping. *Credit: http://home.strw.leidenuniv.nl/ dynamics/Instruments/Sauron/.*

2.2.1 WHT observations

Spectra for NGC 2859, NGC 3941, NGC 4725, and NGC 5850 were taken during four nights in 2007 (14 and 16-18 April) with SAURON (Bacon et al., 2001), a private instrument developed by a consortium composed by the Lyon Observatory (France), Leiden Observatory (Holland), and Oxford University (United Kingdom), and attached to the Cassegrain focus of the 4.2 m WHT telescope. SAURON is an integral-field spectrograph based on the lenslet array concept, already explained in Section 1.5 in Chapter 1. Figure 2.3 illustrates the SAURON optical design and the way it sections the FoV in order to pack the spectra from each spaxel onto the CCD detector. It is worth noting that SAURON does not use optical fibers to conduct the light towards the dispersor element, so it prevents the great loss of light introduced by these elements.

SAURON provides two resolution modes, both with a spectral dispersion of 1.1 Å pixel^{-1}. For the double-barred sample observations, the spectrograph was operated in the Low-Resolution (LR) mode, characterised by a 33×41 arcsec^2

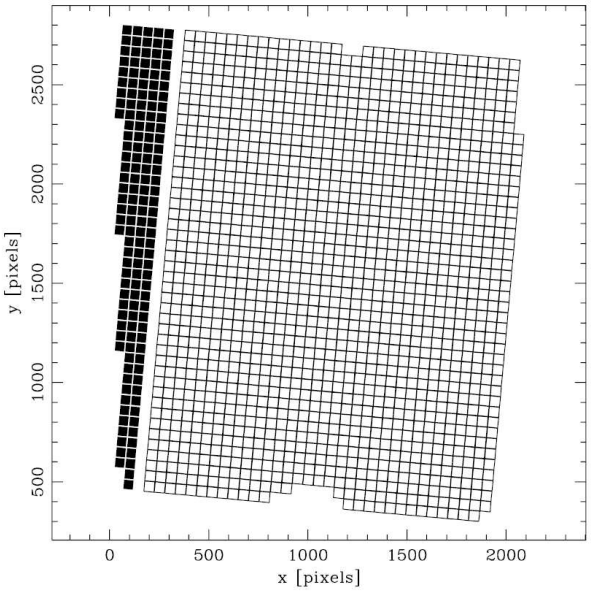

FIGURE 2.4— Distribution of the lenses on the SAURON CCD detector. Black squares indicate the location of the sky lenses, which take spectra at a distance of 1.9 arcmin from the galaxy FoV. *Figure taken from Bacon et al. (2001).*

FoV , a spatial sampling of 0.94 arcsec spaxel^{-1}, and a spectral resolution of 3.74 Å (FWHM), which corresponds to $\sigma_{\rm inst} \sim 94$ km s^{-1}.. The dispersor element is a VPH (Volume Phase Holographic) grism, which covers the wavelength range from 4800 to 5380 Å. Finally, the detector is an EEV12 CCD composed of 2148×4200 pixels of 13.5×13.5 μm^2 each.

The observations were taken with the galaxies centred on the focal plane corresponding to the lenslet array, and the instrument was orientated so the major axis of the FoV is parallel to the major axis of each galaxy disc. The total integration time for the galaxies ranged between three and four hours, in exposures of 30 min each. Detailed information on the observation nights is found in Table 2.2. The dithering of 1 arcsec applied between the different exposures allows a correction of possible bad pixels of the CCD. Apart from the object lenslets, SAURON has an additional array of 146 lenses for simultaneous sky observations. These spectra are taken at a distance of 1.9 arcmin from the main FoV and their location on the CCD is shown in Figure 2.4.

At least one Neon lamp exposure of 30 seconds was obtained after each

galaxy exposure, in order to check the focus and possible bending of the instrument and to assure an accurate wavelength calibration. Sky flatfields were taken during the twilights, whereas Tungsten lamp and dome flatfields were respectively observed during each night and during the periods the dome was closed due to weather conditions. Only one flux standard star was used in this work, namely EG131. Several standard stars of different spectral types and common to both Lick and MILES (Sánchez-Blázquez et al., 2006) libraries were observed during each night. The weather conditions were changeable, with a seeing FWHM value ranging from 0.5 to 1.6 arcsec. The humidity forced the closing of the dome several times, preventing the observation of more galaxies.

2.2.2 NTT observations

The long-slit spectroscopic observations of NGC 357 were carried out with the 3.5 m NTT telescope at the European Southern Observatory (ESO) in La Silla (Chile) on 5-13 October 2002. The `EMMI` instrument was operated both in blue (BLMD) and red medium-dispersion spectroscopic (REMD) modes.

`EMMI` was mounted on the NTT in BLMD using the grating No. 3 blazed at 3800 Å with 1200 grooves mm^{-1} in the first order in combination with a 1.3 arcsec $\times$ 5.5 arcmin slit. The detector was the No. 31 Tektronix TK1024 EB CCD with 1024×1024 pixels of 24×24 $\mu\mathrm{m}^2$. It yielded a wavelength coverage between about 3990 Å and 4440 Å with a reciprocal dispersion of 0.45 Å pixel^{-1}. The spatial scale was 0.37 arcsec pixel^{-1}. The instrumental resolution was 1.3 Å (FWHM) corresponding to $\sigma_{\mathrm{inst}} \sim 40$ km s^{-1}.

Six spectra of 45 min each were taken aligning the slit with the major axis of the inner bar (PA = 45°, see Table 2.1). Two more spectra of 45 min each were obtained aligning the slit with the major axis of the outer bar (PA = 120°, see Table 2.1). All the spectra were obtained using the guiding TV camera to centre the slit on the galaxy nucleus.

`EMMI` was mounted on the NTT in REMD using the grating No. 6 blazed at 5200 Å with 1200 grooves mm^{-1} in first order. A 1.0 arcsec $\times$ 5.5 arcmin slit was adopted. The mosaiced MIT/LL CCDs No. 62 and 63 with 2048×4096 pixels of 15×15 $\mu\mathrm{m}^2$ covered the wavelength range between about 4800 Å and 5460 Å. The on-chip 2×2 pixel binning provided a reciprocal dispersion and spatial scale of 0.40 Å pixel^{-1} and 0.332 arcsec pixel^{-1}. The instrumental resolution was 1.6 Å (FWHM) corresponding to $\sigma_{\mathrm{inst}} \sim 30$ km s^{-1}.

TABLE 2.2— Summary of the observations.

	Dates of observation (1)	# of exposures (2)	Total integration time (3)	Seeing (4)	Central S/N (5)
NGC 2859	April 14, 2007	2	4 hours	1 arcsec	353
	April 17, 2007	6		0,9 arcsec	
NGC 3941	April 17, 2007	7	3,5 hours	0,6 arcsec	389
NGC 4725	April 18, 2007	6	3 hours	1 arcsec	252
NGC 5850	April 16, 2007	5	4 hours	1,6 arcsec	161
	April 17, 2007	2		0,6 arcsec	
	April 18, 2007	1		1 arcsec	

(1) Observation nights of each galaxy;
(2) number of exposures of 30 min;
(3) total integration time for each galaxy;
(4) mean seeing value during the observation period of the same galaxy each night;
(5) maximum S/N value reached for each galaxy; this S/N corresponds to a spectrum in the central region of the galaxy, where the surface brightness profile presents also a maximum.

After centring the slit on the galaxy nucleus, two spectra of 30 min each were obtained along the disc major axis (PA = 20°, see Table 2.1).

The range of the seeing FWHM during the observing runs was 0.6-1.4 arcsec as measured by the ESO Differential Image Motion Monitor. A comparison lamp exposure was obtained after each object integration to allow accurate wavelength calibration. Quartz lamp and twilight sky flatfields were used to remove pixel-to-pixel variations and large-scale illumination patterns. Several G and K stars and spectrophotometric standard stars were observed with the same set-up to serve as templates in measuring the stellar kinematics and in flux calibration, respectively.

2.3 Data reduction

The reduction process for the integral-field spectra presents some peculiarities with respect to the traditional long-slit data reduction. In this Section we describe the actions carried out to prepare the spectra for their later detailed analysis, putting special emphasis on the particular steps required by the SAURON data and on the key actions needed to procure a high-quality reduction in order to further study the kinematics and stellar populations of double-barred galaxies.

2.3.1 SAURON spectra

The data reduction of the SAURON data was mainly performed using the specifically designed XSAURON package, following the prescriptions given in Bacon et al. (2001) and in Emsellem et al. (2004). Additional programs in IDL were also used to deal with the spectra. As usual, the first step is the preprocessing of the images, which includes bias, overscan, and dark subtraction. The spectra are then extracted from their CCD packing. For this purpose it is necessary to create a mask, i.e., a pattern of almost parallel lines indicating which pixels of the CCD corresponds to the same spectrum of each spaxel. The mask making is a very crucial step which has to be carried out very carefully, since any error in the mask is transformed into a mixing of the final spectra. Figure 2.5 shows an example of a Neon spectrum extracted with a subtly wrong mask: even though the error is very slight, it causes the contamination by the so-called *ghost lines*, coming from adjacent spectra.

The mask is characteristic of each observing run, since bends or slight changes in the physical configuration of the instrument generate distortions on the final CCD image. It is important to note that SAURON is located at the Cassegrain focus, so it is subject to strain forces as the telescope moves. To

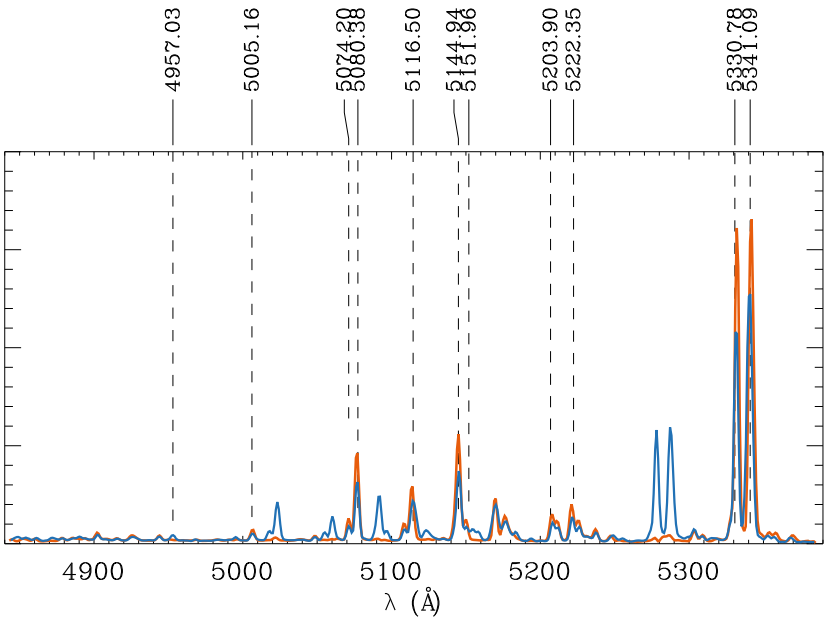

FIGURE 2.5— Neon spectrum extracted with a correct mask (orange) and with a wrong mask (blue). The bad-extracted spectrum is affected by ghost lines, due to contamination from adjacent spectra. In this particular case, the ghost lines appear at a central wavelength which is 62 Å lower than the central wavelength of the original features.

create the mask, we use an iterative process over a previous mask and a Tungsten flatfield exposure; the Tungsten images do not contain prominent spectral features and therefore they provide the main information needed for the mask making. Figure 2.6 illustrates the advantages of using a Tungsten flatfield to generate the mask.

The initial mask is, in turn, iteratively shifted and rotated in order to match the observed Tungsten exposures, thus creating the correct mask for the specific data. Several details, such as the bad columns on the CCD or gradients in the spectrograph transmission, have to be properly fixed before or during the mask making in order to finally find the most suitable mask for each observing run.

Once the individual spectra are extracted, they are wavelength calibrated taken as a reference the known lines of the Neon spectrum, also identified in Figure 2.5. We get a final standard deviation for the calibration of 0.090 pixels.

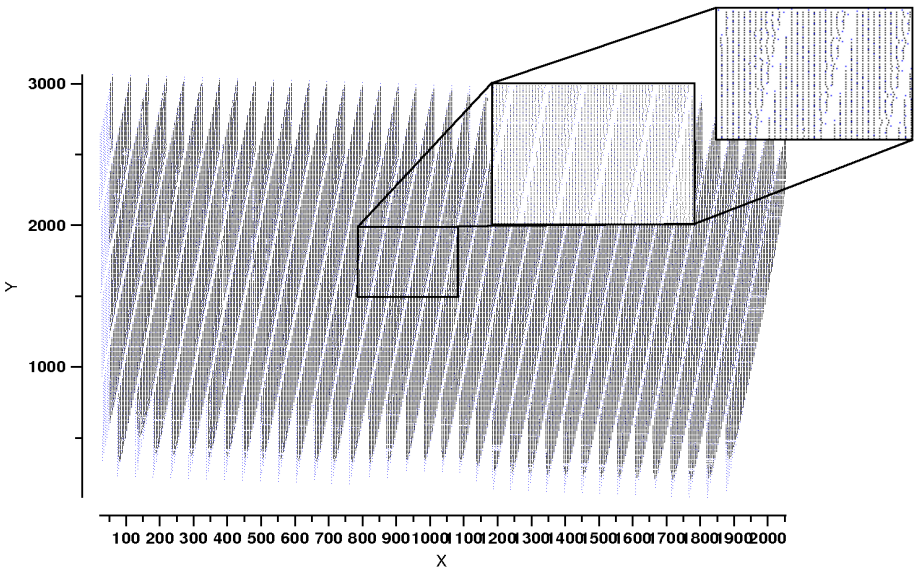

FIGURE 2.6— Identification of the light maxima over a Tungsten flatfield exposure. Blue dots indicate the real maxima of the image, whereas black dots are those used by XSAURON for the mask fitting and should perfectly overlap with the blue ones. Each line association corresponds to a single spectrum from the same lens. The insets show deviations at the edges of each spectrum, where the S/N ratio is too low due to an optical filter placed before the spectrograph; the corresponding spectral regions are cut from the final data to assure a safe spectral range for the analysis.

The goodness of the mask extraction and wavelength calibration is then checked with several tests, such as the one presented in Figure 2.7: since a sky flatfield captures the same solar spectrum for each spaxel, the corresponding velocity distribution should be flat and with a constant value around $\sim$10 km s^{-1}, due to the combined effect of the heliocentric velocity and the Sun's velocity with respect to a rest frame for the observing night. The final velocity map shown in Figure 2.7 still presents a gradient of $\sim$10 km s^{-1}, i.e., 15% of the pixel size; this value is within the expected error tolerance for the reduction process.

The next step is to correct the data from the sky flatfield, which provides information on the effects introduced by the dispersor element, and from the Tungsten flatfield, which indicates pixel-to-pixel variations on the CCD. Dome instead of Tungsten flatfields can be also used, and slight differences appear in the final reduced data; the analysis presented in this thesis (Chapters 4 and 5

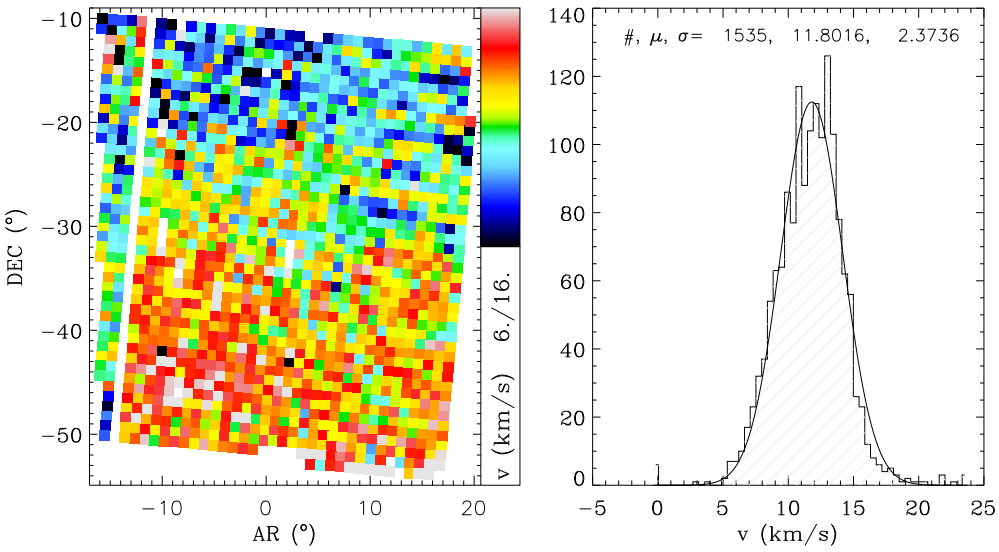

FIGURE 2.7— LOS velocity map (left panel) and distribution (right panel) for a sky flatfield exposure. A correct extraction and wavelength calibration should provide the same velocity value for all the spaxels of the sky flatfields. Our final reduction process is affected by a gradient of $\sim$10 km s^{-1} in the velocity distribution, in agreement with the expected results since it represents a 15% of the pixel size. The velocity distribution is centred at $\sim$10 km s^{-1} due to the heliocentric and Sun's velocities for the observing nights.

have been completely performed with the two corrections and the final results correspond to the reduction with the dome flatfields.

The spectra are then cleaned from cosmic rays and homogenized to the same spectral resolution, which is estimated as 8.4 Å (FWHM, σ $\sim$96 km s^{-1}) attending to the resolution map derived from the sky flatfield and shown in Figure 2.8. Next, the sky subtraction is performed thanks to the spectra taken with the sky lenses devoted to this purpose. We flux-calibrate the data with the observed EG131 white dwarf standard star, and we align and sum up the spectra from different exposures in order to create a single, high S/N cube for each galaxy, which is finally converted to the standard Euro3D FITS format (Kissler-Patig et al., 2004) for its later analysis. It is important to note that the final spectra are also cut to a safe spectral range from 4825 to 5280 Å, which prevents the problems related to a bad extraction of the regions at the spectral edges.

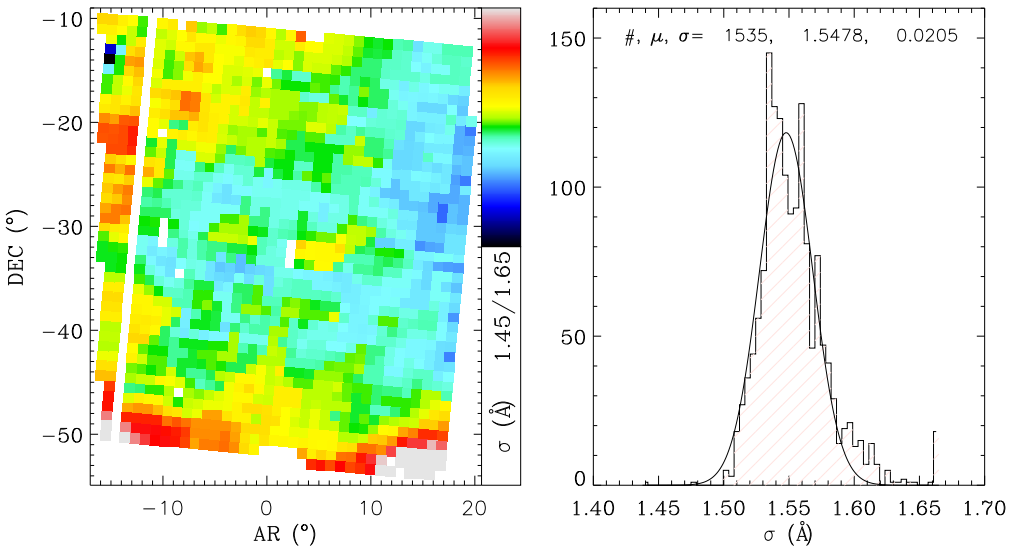

FIGURE 2.8— Determination of the spectral resolution of the SAURON data, measured as the LOS velocity dispersion over the sky flatfields. Left panel represents the resolution (σ) spatial distribution for the sky flatfield, while the right panel shows the corresponding histogram, i.e., the number of spaxels with a specific spectral resolution. We finally estimate a value of σ =1.62 Å, which means 8.4 Å (FWHM) or $\sim$96 km s^{-1}, Although there are a few lenses with lower values of the spectral resolution, these are not taken into account because they are located at the edges of the CCD, where the quality of the data drops, as expected.

In order to assure the minimum S/N ratio required for our analysis, we bin spatially the final datacubes using the Voronoi 2D binning algorithm of Cappellari & Copin (2003) which accomplishes the three main requirements of a valid spatial binning: the topological requirement (the whole FoV is covered without holes or bin overlapping); the morphological requirement (the bins are compact and well associated with a particular spatial region); and the uniformity requirement (the scatter in the S/N rations among bins is as small as possible). Thus, we create compact bins with a minimum S/N of $\sim$ 60 per spectral resolution element, which allows us to measure the higher order moments of the line-of-sight velocity distribution (hereafter LOSVD), h_3 and h_4. Note however that the spectra corresponding to the central regions of the galaxies have already S/N values well above 60 Å^{-1} (see Table 2.1), so they remain unbinned.

2.3.2 EMMI spectra

The EMMI spectra are reduced using mainly standard IRAF[1] routines. The data are first overscan and bias subtracted and flatfield corrected. As with the SAURON data, two types of flatfields are used: the sky flatfields, to address blendings or variations due to the slit configuration, and the dome flatfields, to correct for the pixel-to-pixel changes on the CCD The bad pixels and columns of the EMMI CCD are interpolated before the wavelength calibration, which is performed using Helium-Argon calibration spectra. Cosmic ray removal is a critical step since any residual might affect the spectral lines measured to derive the properties of the stellar populations. It was performed with the REDUCEME package (Cardiel, 1999), which assures a careful and accurate inspection and interpolation of the spectra. We checked that the wavelength rebinning was done properly by computing the difference between the measured and predicted wavelengths (Osterbrock et al., 1996) for the brightest night-sky emission lines in the observed spectral ranges. The resulting accuracy in the wavelength calibration is better than 5 km s^{-1}.

The spectra taken along the same axis were co-added using the centre of the stellar continuum as reference. The contribution of the sky was determined from the outermost regions at the two edges of the resulting spectra, where the galaxy light was negligible, and then subtracted, giving a sky subtraction better than 1%. A one-dimensional sky-subtracted spectrum was obtained for each kinematical template star. The sky-subtracted spectra were flux calibrated using the observed spectrophotometric stars as a reference. Neither extinction nor dust corrections were applied for the blue spectra since the wavelength coverage is short and we are not interested in colour measurements.

Finally, the galaxy spectra were binned along the spatial direction in order to assure a minimum S/N ratio of $\sim 20\,\text{Å}^{-1}$, sufficient for the kinematic analysis performed in this work for NGC 357, which is restricted to the study of the velocity and velocity dispersion profiles. This minimum S/N ratio is reached only in the outermost radial bins, as it increases at smaller radii reaching a maximum S/N$\sim 60\,\text{Å}^{-1}$ in the radial bin corresponding to the galaxy centre. The spatial binning procedure was carefully carried out in order to assure the separation of the different structural components of NGC 357 (i.e., the bulge, inner, and outer bar) and thus achieve the goals of the present thesis.

[1]Imaging Reduction and Analysis Facilities (IRAF) is distributed by the National Optical Astronomy Observatories which are operated by the Association of Universities for Research in Astronomy (AURA) under cooperative agreement with the National Science Foundation.

3

A look into the photometry

Her mind is Tiffany-twisted,
she got the Mercedes bends
Hotel California (The Eagles)

Inner bars were first discovered through the photometric analysis of optical and near-infrared images, as explained extensively in Chapter 1. Length, strength, position angle, or ellipticity are important parameters for bar characterisation, and they can be obtained easily by ellipse-fitting to the surface brightness distribution of a barred galaxy. For the present study we have made use of the catalogue of double bars of Erwin (2004), who also provides the relevant information derived from photometric studies collected in Chapter 2. Our brief and minor contribution to the photometric analysis has two very particular motivations: for the SAURON sample, we just aim at exploring the capability of the spatial information provided by the integral-field data, dealing with the collapsed spectra as if they were optical images. In the case of NGC 357, we perform ellipse-fitting in order to study in detail the profiles of the photometric parameters, necessary for the discussion of Chapter 6 on the structural composition of this double-barred galaxy.

3.1 Photometric analysis on the integral-field spectra

The main property of integral-field data is that they contain not only the spectral but also the spatial information from the galaxies (see Section 1.5 for a review on this topic). However, the *images* taken from the integral-field data are usually hampered by poor spatial resolution or a very restricted FoV, so it is not common to use them in photometric studies, for which more suitable

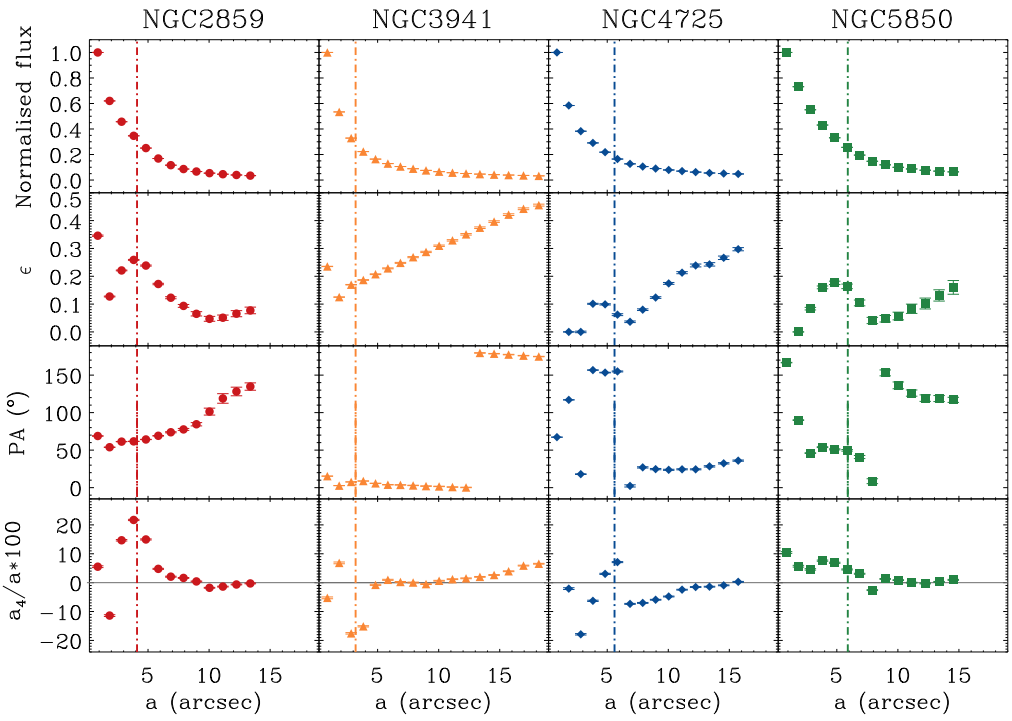

FIGURE 3.1— Normalised flux (top panels), ellipticity (second panels), PA (third panels), and the fourth cosine Fourier coefficient (a_4; bottom panels) profiles resulting from fitting ellipses to the isophotes of the reconstructed flux map for the four double-barred galaxies: NGC 2859, NGC 3941, NGC 4725, and NGC 5850 (from left to right). The x-axes represent the semi-major lengths of the fitted ellipses. The dot-dashed vertical lines indicate the inner bar lengths as given by Erwin (2004).

high resolution images are used. However, in order to probe the high-quality of our integral-field spectroscopic data and explore their capabilities, we have performed this kind of analysis over the flux maps recovered after stacking our spectra in the wavelength direction for the four double-barred galaxies. For this purpose we have taken advantage of the Kinemetry program (Krajnović et al., 2006), which calculates the best fitting ellipses in the same way is done for typical surface-photometry analysis. The resulting normalised flux, PA, ellipticity, and the fourth cosine Fourier coefficient (a_4) profiles are shown in Figure 3.1. As mentioned in Chapter 2, the SAURON FoV is smaller than the main bars except for NGC 3941, which is completely mapped with SAURON. Even so, the requirements for ellipse fitting do not allow us to reach the limit of the outer

bar in the photometric profiles.

The PAs and maximum ellipticities of the inner and outer bars, as well as the inner bar lengths recovered with the photometric analysis performed on the integral-field spectroscopic data, are consistent with the results obtained by Erwin (2004) with high-quality images. NGC 2859, NGC 4725, and NGC 5850 show the typical peak in the ellipticity profile due to the presence of the inner bar, and the two last galaxies also show the discontinuity in the PA profile at the same location. The presence of the inner bar in NGC 3941 is difficult to appreciate in this analysis due to its small size and ellipticity.

The a_4 parameter also tends to peak at the position of the inner bar; a_4 is a measurement of the deviation of the isophotes from pure ellipses, so positive values correspond to discy isophotes whereas negative values indicate boxy isophotes (Jedrzejewski, 1987; Kormendy et al., 2009). Two of the four galaxies, NGC 2859 and NGC 5850, are mainly shaped by discy isophotes especially at the inner bar end. NGC 4725 shows boxy isophotes in the inner 5 arcsec, and NGC 3941 presents boxy isophotes only at the inner bar edge.

3.2 Photometry of NGC 357

The structural composition of NGC 357 has revealed itself to be very intriguing and complex, as it has to account for all the observational results derived from the kinematics and stellar population analysis presented in Chapter 6, where we also discuss different possibilities for the shaping of this galaxy. As a first approach for disentangling the morphology of NGC 357, we perform an ellipse fitting over a NICMOS2 (Near Infrared Camera and Multi-Object Spectrometer) F160W image taken from the Hubble Legacy Archive (Prog. Id. 7330, PI John Mulchaey). NICMOS covers a FoV of $\sim 52 \times 52\,\mathrm{arcsec}^2$ at a dispersion of $\sim 0.1\,\mathrm{arcsec\,pixel}^{-1}$, so it maps the whole galaxy including both the inner and outer bars. In this case we use the IRAF task ELLIPSE, which follows the procedure outlined by Jedrzejewski (1987).

Figure 3.2 shows the resulting profiles of ellipticity, PA, and the fourth cosine Fourier coefficient, a_4. Again, the presence of the bars causes two sharp changes in the ellipticity and PA parameters: one peak at ~ 3 arcsec related to the inner bar, and a discontinuity at ~ 25 arcsec due to the outer bar. These two values are in agreement with the bar lengths estimated by Erwin (2004), as well as the PAs and maximum ellipticities (see also Aguerri et al., 2005). The a_4 profile also shows two peaks at the locations of the two bars; they present discy isophotes, as in the case of the SAURON sample. Further implications of

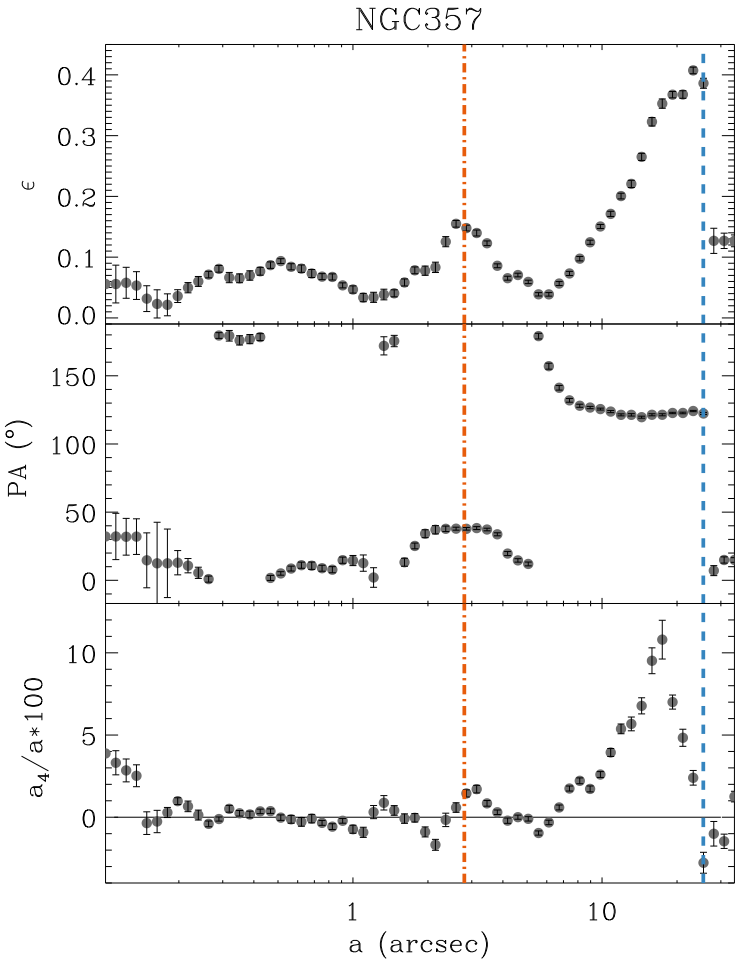

FIGURE 3.2— Ellipticity (top panel), position angle (middle panel), and fourth cosine Fourier coefficient (bottom panel) profiles that result from fitting ellipses to the isophotes of NGC 357 in the NICMOS2 F160W image. The semi-major axes of the fitted ellipses are given on a logarithmic scale. The vertical orange dot-dashed and blue dashed lines indicate the lengths of the inner and outer bars, respectively.

this analysis will be discussed in Chapter 6.

4

Stellar and gas kinematics

Busca busca maravalla,
que el que busca siempre halla

Part of the results presented in this Chapter have already been published in:
de Lorenzo-Cáceres et al. 2008, The Astrophysical Journal, Vol. 684, Issue 2, pp. L83-L86

How the stars and gas which shape a galaxy move is important evidence for understanding its present morphology and structure and, at the end, constraining its evolution. Moreover, line-of-sight kinematics can be derived in a very accurate way from high-quality observations, thus providing a unique and powerful tool for studying the characteristics of the galaxy and identifying relevant signatures. In this Chapter we completely characterise the stellar kinematics of the four double-barred galaxies observed with SAURON and presented in Chapter 2. We will put special emphasis on the discovery of the so-called σ-*hollows*, the only known kinematical signature of the presence of inner bars. Finally, we will show some results for the kinematics of the ionised gas content of the four galaxies, which also shows very interesting and motivating results.

4.1 Stellar kinematics

The stellar kinematics is extracted by performing a full-spectrum fitting over the stellar spectra, as described in e.g., Falcón-Barroso et al. (2006). The potential emission lines included in the SAURON spectral range (i.e., Hβ, [OIII]5007 and [NI]) are masked in order to work with the pure absorption contribution. We make use of the penalized pixel fitting (hereafter pPXF) routine developed

by Cappellari & Emsellem (2004), based on a χ^2 minimisation algorithm which fits each stellar spectrum with a linear combination of a well-selected set of templates. Traditionally, spectra of velocity standard stars observed during the same run as the galaxies were used as templates for this kind of fitting, with the advantage that these spectra already include the variations and properties linked to the instrumental setup. However, Falcón-Barroso et al. (2003) demonstrated that stellar population synthesis models (hereafter SSPs) are a better choice for the full-spectrum fitting, since they help to alleviate the *template mismatch* problem, related to the lack of stars sampling the whole metallicity regime.

For this work we selected a subsample of the single stellar population models (SSPs) of Vazdekis et al. (2010), with evenly sampled ages and metallicities. The number of templates is limited to around 40 SSPs in order to avoid having too many free parameters in the fitting, which could prevent the convergence of the minimisation algorithm. The SSPs of Vazdekis et al. (2010) are developed from the MILES stellar library (Sánchez-Blázquez et al., 2006) and cover the whole spectral range, from 3540 to 7410 Å, at a constant resolution of 2.51 Å (Falcón-Barroso et al., 2011).

The SSPs are first convolved with a LOSVD, which is parametrized by an expansion in Gauss-Hermite functions (Gerhard, 1993; van der Marel & Franx, 1993). We therefore recover the four lower-order moments of the LOSVD: velocity (v), velocity dispersion (σ), h_3, and h_4. We do not derive h_5 and h_6 due to the demanding S/N requirements. h_3 and h_4 are measurements of the asymmetric and symmetric deviations of the LOSVD from the pure gaussian behaviour, respectively.

The spatial distribution of the four stellar kinematical parameters measured for the four double-barred galaxies, namely velocity, velocity dispersion, h_3, and h_4, can be seen in Appendix A, which collects all the maps derived for each galaxy. In the following Sections we will study in detail the main results revealed by those maps, showing the specific Figures for each case.

4.1.1 The stellar σ-hollows

The stellar velocity dispersion maps of the four double-barred galaxies shown in Figure 4.1 reveal some interesting features not seen in other morphological types of galaxies. The values measured are at a maximum at the centres of the galaxies (as seen in most E/S0 galaxies) but, instead of smooth negative velocity dispersion gradients towards the outer parts, we find two symmetrical regions where the velocity dispersion values drop significantly compared to their surroundings. These *σ-hollows* are located exactly along the major axes of the inner bars and they extend out to the edges, as we checked with several tests.

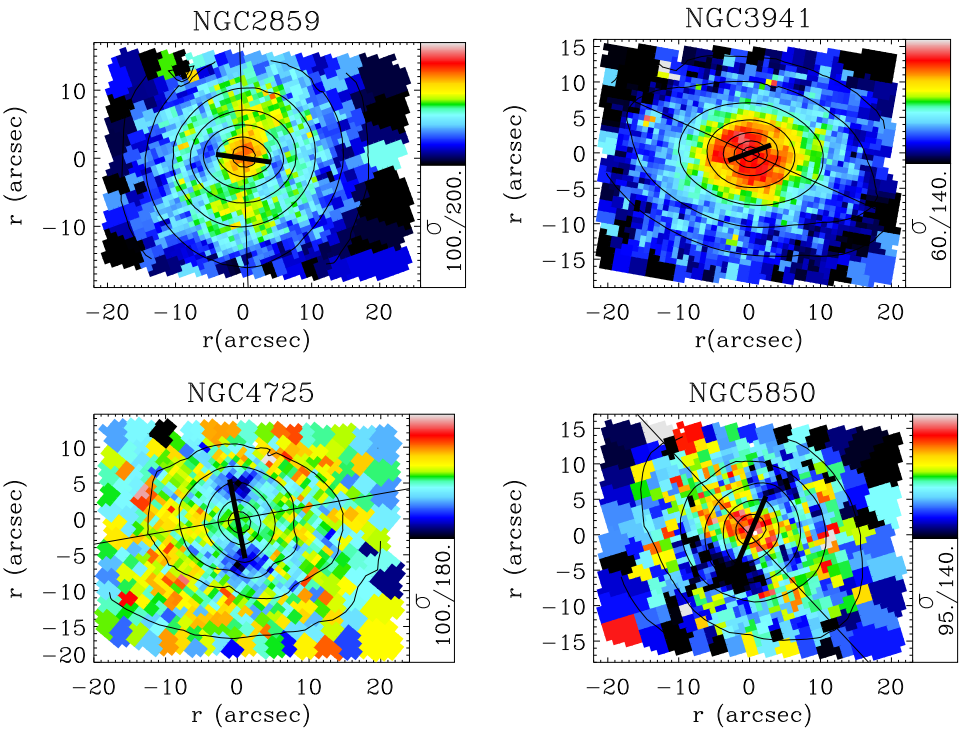

FIGURE 4.1— Stellar velocity dispersion maps (in km s^{-1}) for the four double-barred galaxies: NGC 2859, NGC 3941, NGC 4725, and NGC 5850. The length and position angle of the inner and outer bars are indicated by a thick and a thin lines, respectively. We have also overplotted the contours of the reconstructed total intensity maps. The σ-hollows are clearly seen at the edges of the four inner bars, as two spots with bluer colours (i.e., lower values) than the surroundings.

The amplitude of the hollows varies between 10 and 40 km s^{-1}. Interestingly, neither the Hβ or [OIII] emission-line maps (discussed in Section 4.2 and shown in Appendix A) present any distinct features at the same locations of the inner bars. The stellar velocity dispersion map for NGC 5850 was previously shown by Moiseev et al. (2004), but no hollows are seen in there, probably because the smaller FoV of the `MPFS` instrument used in those observations.

4.1.2 The origin of the σ-hollows

Since the σ-hollows of the four galaxies are observed exactly at the ends of the inner bars, it seems that they are related to the inner bar itself and not to any other structural or kinematical component. In order to investigate the origin of

the σ-hollows, we discuss in this Section some possible explanations for these observations.

The presence of an inner disc

Stellar inner discs could, in principle, explain a decrease in velocity dispersion in the central regions of galaxies, as happens with the σ-drops seen in Emsellem et al. (2001, see Section 1.4.3 in Chapter 1 for a description of these σ-drops). However, the observed alignment of the σ-hollows with the major axis of the inner bar cannot be accounted for by the presence of an inner disc whose major axis is usually well aligned with the main photometric major axis of the galaxy. Moreover, the decrease in velocity dispersion in our galaxies does not occur at the same locations as the σ-drops seen by Emsellem et al. (2001); in fact we find that the velocity dispersion reaches a maximum value at the centre. The possibility of a gaseous inner disc is discarded because the effect we see in our data is purely stellar.

A young stellar population component

A young stellar component that has acquired the kinematics of the cold gas it was formed from could also explain the decreases in the velocity dispersion values. This young population might not necessarily be associated with a different structural component (e.g., a nuclear star forming ring). The stellar populations analysis performed in Chapter 5 will show there is no any evidence for the presence of a particularly young stellar population at the σ-hollows locations.

A matter of contrast

Finally, we focus on the immediate surroundings of the inner bar. The four double-barred galaxies have central velocity dispersion values $\sigma > 140\,\mathrm{km\,s^{-1}}$, indicating that they contain classical, pressure-supported bulges. Therefore, in the central parts of these galaxies we have the combination of a component with typically high velocity dispersion (i.e., the bulge) and the inner bar with its ordered motion and thus a low σ. We propose that the presence of the σ-hollows is due to the contrast between the velocity dispersion of these two components. Since the velocity dispersion profile and the luminosity profile of the bulge decreases outwards, we can only see this effect in the outer parts of the inner bar, where the bulge is not totally dominating the flux. Therefore the amplitude of the hollows will depend on the relative contribution of the bulge to the total luminosity at the extremes of the bar and on the difference of velocity dispersions between the bulge and the inner bar. Irrespective of the relative luminosity of the two components at the edges of the inner bar, if there were

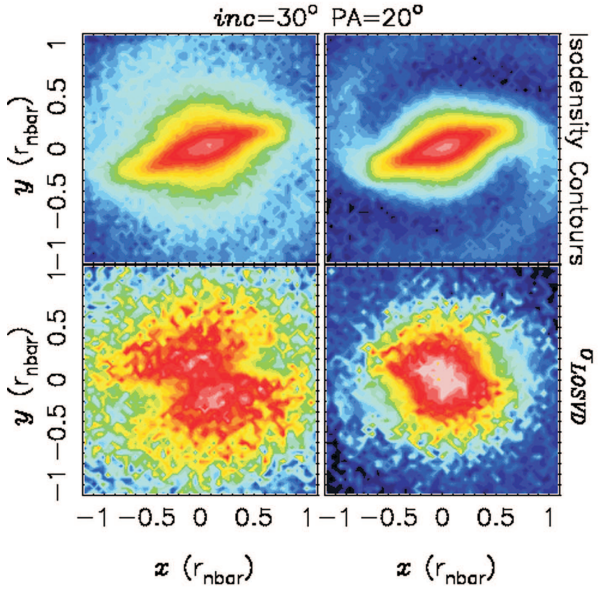

FIGURE 4.2— Numerical simulations including a bulge, a bar and a disc. Top panels: isodensity contours; lower panels: stellar velocity dispersion from the LOSVD. On the left is the case for a bulge big enough to match the size of the bar: the corresponding velocity dispersion map shows clearly the σ-hollows. On the right is the case of a very small bulge, whose luminosity drops quickly with radius such that its contribution is not relevant at the ends of the bar. The σ-hollows in this case become difficult to detect.

no differences between the velocity dispersions we would not be able to find any σ-hollows. Assuming that there is a significant difference in the σ values at these points, a very extended bulge may have the inner bar embedded in it, so we would expect very deep σ-hollows in this case. On the contrary, if the bulge were less extended these σ-hollows would not show up.

To test this idea we used the code FTM 4.4 (updated version) from Heller & Shlosman (1994) to perform N-body self-consistent three-dimensional numerical simulations starting with a classical-like bulge and an exponential disc. First, we relax the bulge, in order to have a *quiescent* start, and then we introduce an exponential self-graviting rotating disc. The bulge proceeds to evolve almost steadily, contrary to the disc, which develops a bar instability. Here, we use simulations with a single bar to mimic the main components in the region of interest: the central kiloparsec. This simple approximation is enough to reproduce the σ-hollows: they appear at the ends of the bar for the cases in which the contrast is sufficient. These σ-hollows last as long as the bar stays with a

low σ. Stellar bars in general could be heated-up by the buckling instability, which is milder in the presence of gas (Berentzen et al., 1998, 2007) and in weak bars (Martinez-Valpuesta & Shlosman, 2004). Since the four observed inner bars presented here are not very strong (Erwin, 2004, see Chapter 3) and there is some gas in these regions, most likely they will not buckle. Therefore, we expect the σ-hollows to be long-lived structures.

In Figure 4.2 we illustrate two of our models: one case of a bulge large enough to match the length of the bar, where we are able to reproduce the σ-hollows, and one case with a smaller, less extended bulge where the velocity dispersion profile is almost unchanged. The simulations shown here use a galaxy inclination of 30° (as a representative case of our observations) and a position angle of 20° for the bar. However, we repeated the tests with different observational conditions, getting similar results in all cases. Note however that other numerical simulations of double-barred systems (e.g., Shen & Debattista, 2009) do not show any evidence of the presence of the σ-hollows in their velocity dispersion maps. A possible explanation for this absence is the fact that in those simulations there is not the necessary velocity dispersion difference between the resulting structural components, since they do not include a sufficiently dynamically hot component (i.e., classical bulge).

4.1.3 Some important remarks on the nature of the σ-hollows

The importance of the σ-hollows lies in that they are signatures of the presence of inner bars, which indicates that they must have significantly lower velocity dispersions than the surrounding, classical bulges. This means that inner bars are cold systems, and are not related to triaxial bulges (Kormendy & Kennicutt, 2004). Moreover, these results put constraints on the degree of rotational over pressure support for these structural components. Finally, since the σ-hollows are not due to other structural or kinematical components (e.g., inner discs), they may be used to identify inner bars from a purely stellar kinematic analysis. In fact, in Chapter 6 we will show that they appear also in the velocity dispersion profile of the fifth double-barred galaxy of our sample, NGC 357, who has been studied in a very different and complementary way to the SAURON data.

The σ-hollows have not been previously found in other works devoted to the study of the stellar kinematics of double-barred galaxies probably due to the precise requirements needed for their observation. In fact, most existing observations of double-barred galaxies rely on long-slit spectroscopy along the major axis of the disc (e.g., Corsini et al., 2003). Only Emsellem et al. (2001) position the slit along the direction of the inner bar, but the S/N in their case is not good enough to distinguish the hollows in the velocity dispersion profile. Better suited integral-field spectroscopy has been used by Moiseev et al. (2004)

with the MPFS instrument. However, their FoV ($16 \times 15\,\mathrm{arcsec}^2$) is significantly smaller than the SAURON FoV, and prevents the observation of the σ-hollows in their galaxy sample. Therefore, our results refute the conclusions of Moiseev et al. (2004) about the influence of inner bars on the kinematical parameters, since we do find signatures of the presence of these structures in the velocity dispersion distributions; note however that, as in the analysis by Moiseev et al. (2004), the velocity maps seem not to be affected by the double-barred system (see Section 4.1.4 for details).

Additionally, we want to stress that none of the galaxies presented in this work show a central σ-drop. The σ-drop is a local velocity dispersion minimum that appears at the centre of many spiral galaxies; the possible explanations for the appearance of σ-drops are already explained in Chapter 1, but to summarise they are usually related to a cold, newly formed stellar component, such as an inner disc. Given the high frequency of σ-drops in spirals and barred galaxies in particular (Falcón-Barroso et al., 2006, and references in Section 1.4.3 of Chapter 1), the fact that none of the four double-barred galaxies shown here presents this signature is particularly remarkable.

4.1.4 Kinematically decoupled inner discs

The stellar velocity maps of the four double-barred galaxies resemble those expected for unbarred galaxies: they do not seem to be affected by the presence of the inner nor the outer bars, and just show the rotation along the major axis of the main galaxy disc, as pointed out by Moiseev et al. (2004). However, for the three cases highlighted in Figure 4.3 (NGC 2859, NGC 4725, and NGC 5850), two local velocity maxima and minima appear at a few arcseconds from the galaxy centre, aligned also with the kinematical major axis. These decoupled structures are rotating faster than their surroundings and are probably due to the presence of stellar inner discs. This hypothesis is supported by the h_3 maps also included in Figure 4.3, which shows a clear anticorrelation with respect to the stellar velocities exactly at the locations of those features, as expected in the case of discs (Bureau & Athanassoula, 2005). Note also that these features found in the velocity and h_3 maps cannot be related in any case to the inner bars, since they have completely different position angles.

Therefore, although the four double-barred galaxies do not present σ-drops at their centres, they do show signatures of the presence of inner discs, thus backing the hypothesis that most of barred galaxies contain a disc-like central component (Pérez et al., 2009).

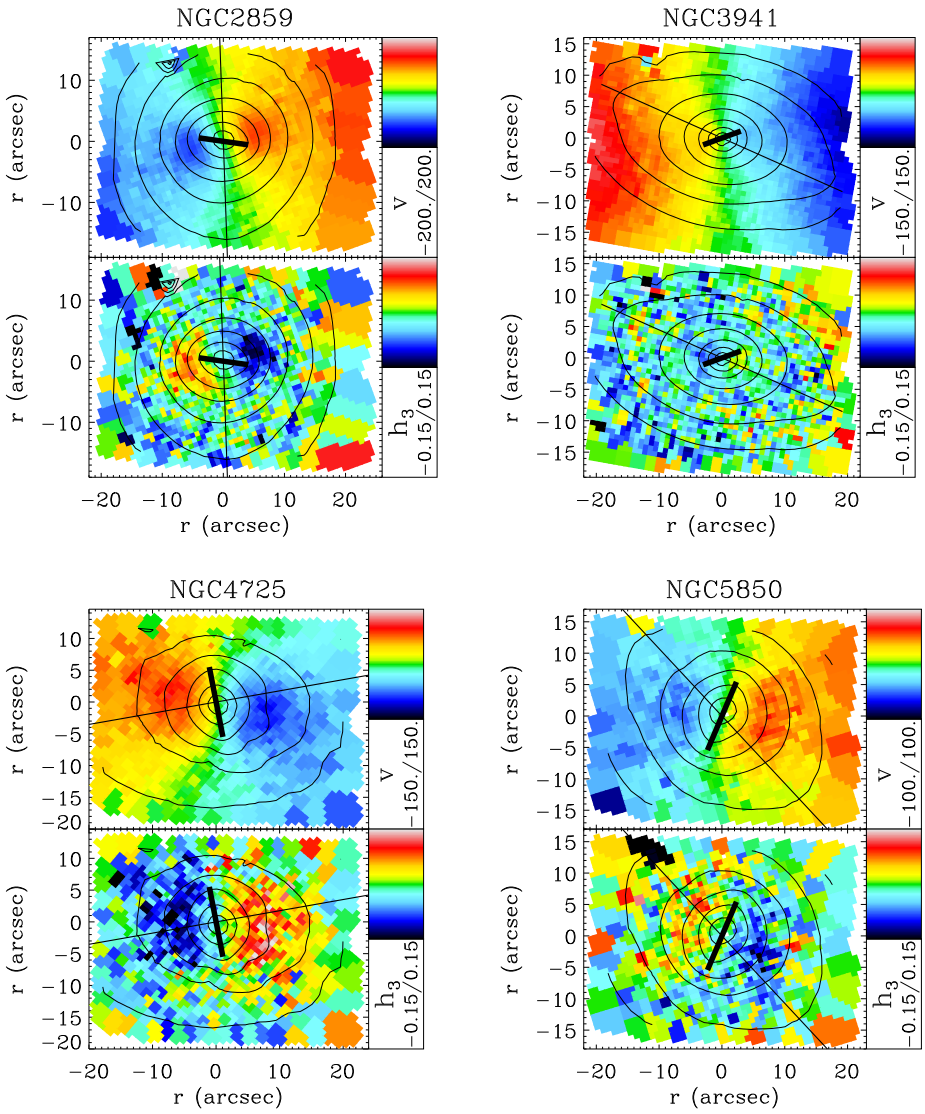

FIGURE 4.3— Stellar LOS velocity (in $\mathrm{km\,s^{-1}}$; top panels) and h_3 (bottom panels) maps for the double-barred sample. Three out of the four galaxies, NGC 2859, NGC 4725, and NGC 5850, show evidences of a kinematically decoupled, corotating inner disc, seen as two local velocity maximum and minimum in the velocity fields at a few arcseconds from the centres, with an anticorrelated counterpart at the same locations in the h_3 maps. None of these signatures appears for NGC 3941. For the sake of clarity, we have overplotted the position angle and length of the inner (thick line) and outer (thin line) bars, and the contours of the reconstructed total intensity map.

4.2 Gas kinematics

Apart from the stars, the galaxies contain ionised gas which produces emission lines, some of which fill in the absorption features in the observed spectra. Therefore, the two contributions have to be carefully separated in order to analyse the stellar or gas content of the galaxies. Our four double-barred galaxies have turned out to present significant amounts of gas, which we have recovered by using the GANDALF code, as described in Sarzi et al. (2006). GANDALF is based on the full-spectrum fitting method and works in a similar way to pPXF. However, instead of masking the spectral regions which are probably affected by emission, it uses the kinematics derived with pPXF as an initial guess and then fits simultaneously the stellar and gaseous contributions. For this purpose it is necessary to include in the set of templates used for the fitting as many Gaussians as potential emission lines might be in the spectra. In the SAURON spectral range, this means mainly Hβ, and the [OIII]4959,5007 and [NI]5198,5200 doublets. The fitting of the whole spectrum is then performed so the amplitudes and kinematics of the emission lines are derived. Some examples of the fittings for the four double-barred galaxies are presented in Figure 4.4.

The analysis of the gas presented in this work comes from the two most prominent emission lines: Hβ and [OIII]5007. Both lines are fitted independently, i.e., they are not forced to have the same kinematics. The gas distribution and kinematics obtained from the two fittings are equivalent for all the galaxies except for NGC 5850, which is discussed in Section 4.2.4. The maps in Appendix A include the gas intensity, velocity, and velocity dispersion distributions derived from the two features, but in the following Sections we mostly show those coming from [OIII]5007, which is the most prominent emission line within the SAURON spectral range.

4.2.1 Possible evidence for gas inflow to the central regions

The gas intensity maps for the four double-barred galaxies reveal interesting spiral structures, specially evident for NGC 2859 and NGC 3941. Moreover, the velocity maps also seem to be disturbed by these spirals, as their zero isovelocity curves appear twisted with respect to the kinematical minor axes. Figure 4.5 highlights the distortion of the velocity fields in comparison with the gas intensities. It is notable the case of NGC 5850, for which this effect appears particularly related to the inner bar, as the distortion in the velocity field make it points at the extremes of the bar.

The spiral structures and the twisting of the velocity fields suggest there are gas streaming motions towards the central regions of these double-barred

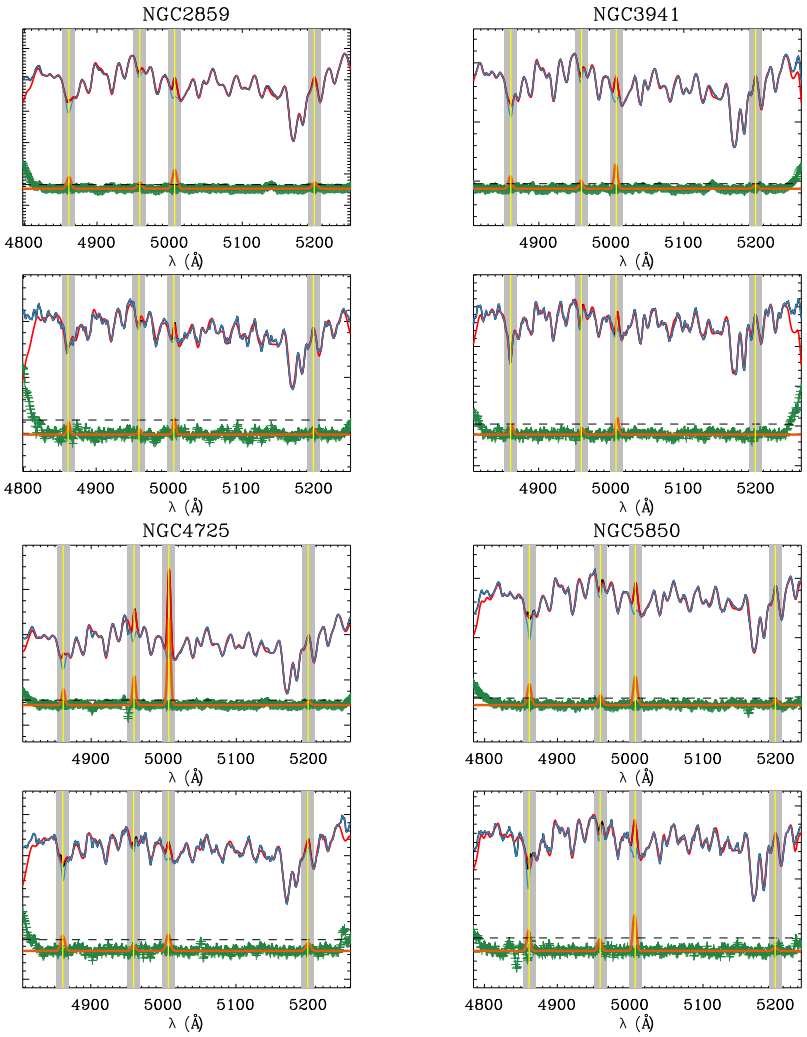

FIGURE 4.4— Examples of full-spectrum-fitting performed with pPXF+GANDALF over the galaxy spectra. For each galaxy, the top panel represents a fitting of the central spectrum, while the bottom panel is a fitting of an outer spectrum with rather lower S/N ratio. The original spectrum is plotted in black whereas the best fit is overplotted in red. Green crosses represent the residuals and the emission spectrum is plotted in orange. The black dashed line indicates the 4σ value of the residuals, taken as a threshold for the emission: only features above this limit are taken into account and subtracted from the data to get a pure stellar or *neat* spectrum, plotted in blue. Vertical yellow lines indicate the position of the potential emission lines and the grey regions are the ranges previously masked when fitting the kinematics with pPXF.

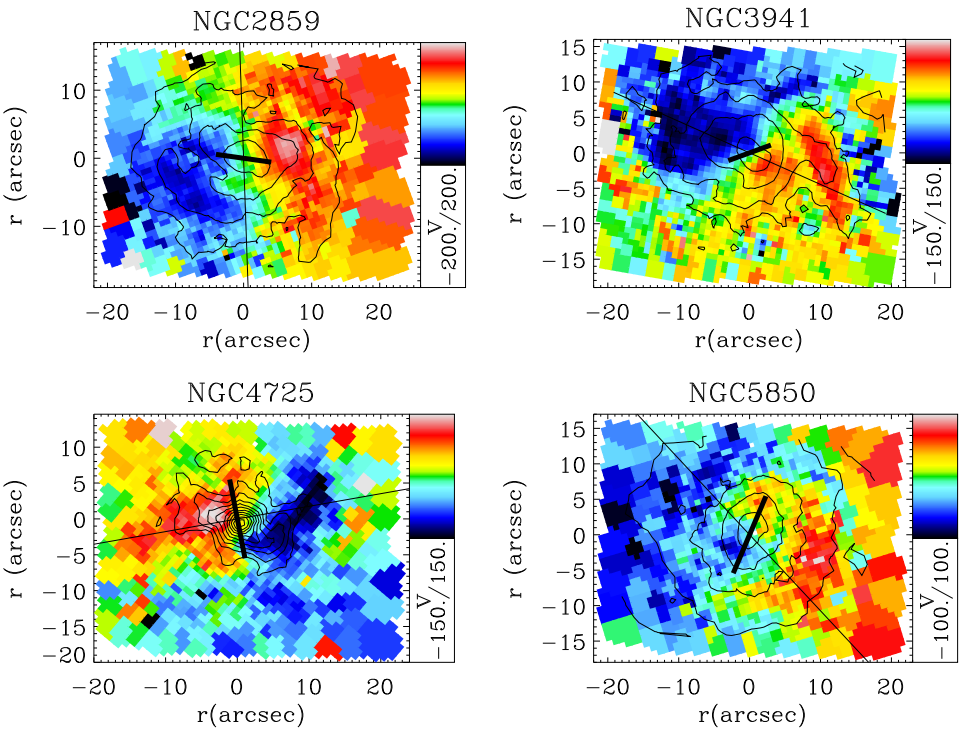

FIGURE 4.5— Gas velocity maps (in km s^{-1}) produced using the [OIII]5007 emission line for the four double-barred galaxies. The zero isovelocity curves are clearly twisted with respect to the kinematical minor axes. The isodensity contours of the [OIII]5007 intensities are overplotted in order to emphasize the distortion of the velocity fields due to the spiral gas distributions. The lines indicate the position and size of the inner (thick line) and outer (thin line) bars.

galaxies. It is also remarkable that, in general, the gas spirals seem to not be related to the main bars of our sample; it is known that ionised gas usually traces dust lanes, which tend to lie parallel to the major axis of the bar in barred galaxies (Athanassoula, 1992; Patsis & Athanassoula, 2000, note also that no dust lanes are expected along inner bars, as shown by Shlosman & Heller, 2002), so it is expected that ionised gas should also be more concentrated along the four outer bars. Although a quick inspection of the results presented here does not support this, it is important to take into account that probably the effect of the twisting towards the inner bars and the restricted SAURON FoV, which prevents the observation of the whole outer bar except for NGC 3941, are masking the general structure of the ionised gas. Moreover, the curvature of the dust lanes is

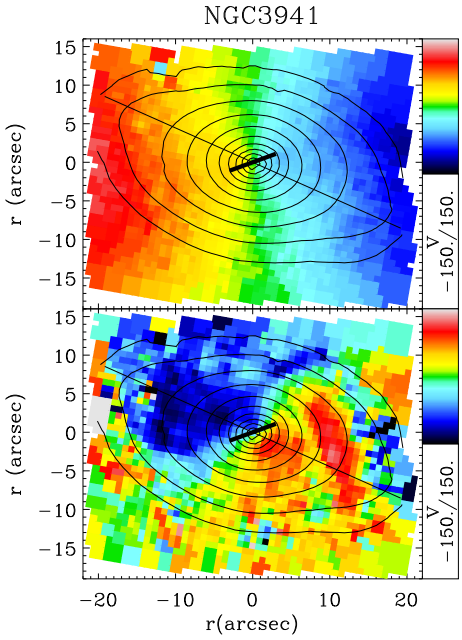

FIGURE 4.6— Stellar (top panel) and gas (bottom panel) velocity maps for NGC 3941, in $\mathrm{km\,s^{-1}}$. We have overplotted the position angle of the inner bar (thick line), the outer bar (thin line), and the contours of the reconstructed total intensity map. The gas in NGC 3941 is clearly counter-rotating with respect to the stars.

anticorrelated with the strength of the bar (Athanassoula, 1992; Comerón et al., 2009), and the two stronger bars of our sample, NGC 4725 and NGC 5850, are precisely those for which the spiral structure is more dilluted.

Unlike the case of the stellar kinematics, the gas velocity dispersion maps for the four galaxies are quite flat and show no signatures of the presence of the inner or the outer bars, as can be seen in the Figures in Appendix A.

4.2.2 Counter-rotating gas in NGC 3941

Figure 4.6 compares the velocity fields corresponding to the stars and gas in NGC 3941, showing that the two components are clearly decoupled and almost-counter-rotating. This counter-rotation is not an unusual feature, as Bertola

et al. (1992) estimate that between 10 and 20 % of S0 galaxies have a counter-rotating gaseous component. Subsequent studies have found even higher values (above 20%) for this fraction (e.g., Pizzella et al., 2004; Bureau & Chung, 2006, among others). However, the case for stars is different: less than ∼10% of S0 galaxies show significant counter-rotating stellar components (Kuijken et al., 1996; Emsellem et al., 2011). It therefore seems that the counter-rotation tends to inhibit the star formation, although there are some interesting cases as that shown in Coccato et al. (2011) for NGC 5719, which presents both gaseous and stellar counter-rotating discs.

The counter-rotation in NGC 3941 was already noticed by Fisher (1997), who suggests that it is probably the result of a merger event or accretion of gas with opposite angular momentum. In fact, merging is one of the most extended explanations for the presence of this kind of structures (Ciri et al., 1995; Barnes, 2002), even in the case of stellar discs (Eliche-Moral et al., 2011). However, there are other possibilities, such as the appearance of *anomalous orbits* within a triaxial and tumbling potential such as that of a bar (Emsellem & Arsenault, 1997; Falcón-Barroso et al., 2004). These anomalous orbits are a family of close, stable, and retrograde orbits, which are tilted with respect to the equatorial plane. Therefore, they can capture the ionised gas thus forming the counter-rotating disc. Given that the kinematical major axis of the gas in NGC 3941 seems to be aligned with the main bar, this last explanation is more likely for its counter-rotating gas disc.

4.2.3 [OIII]/Hβ ratios as tracers of potential star forming structures

In order to study if the four double-barred galaxies present active star forming structures, Figure 4.7 shows the distributions of the [OIII]/Hβ line ratios for the sample. The [OIII]/Hβ is, together with other line ratios, a tracer of the star formation. Although a proper interpretation of the ratio map shown in Figure 4.8 would depend on the comparison with equivalent maps for other line ratios, such as [NII]/Hα (as in the well known BPT diagrams, Baldwin et al., 1981), it is possible to analyse just the presence of structures by considering the relative values. In fact, the four galaxies show pretty flat [OIII]/Hβ distribution with rather high ratio values; hence, within the SAURON FoV none of the galaxies present distinct structures which may be potential star-forming structures, with the notable exception of a very limited region in NGC 5850, discussed in Section 4.2.4.

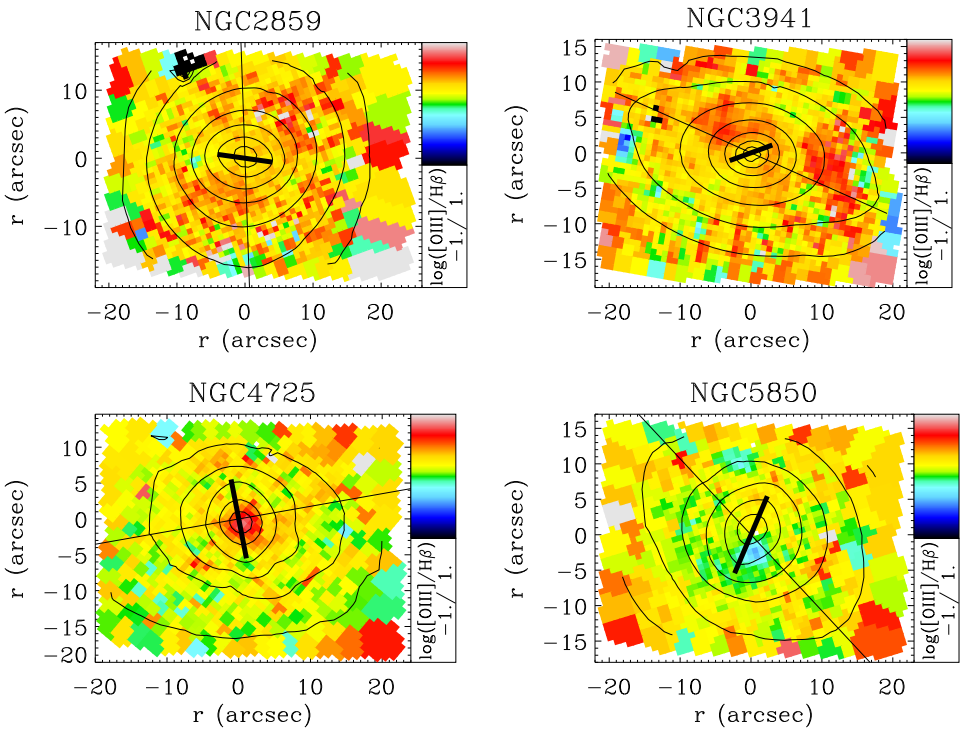

FIGURE 4.7— [OIII]/Hβ ratio maps for the double-barred sample. We have overplotted the position angle and length of the inner (thick line) and outer (thin line) bars, and the contours of the reconstructed total intensity map. The four galaxies show quite a flat distribution and slightly high values for the [OIII]/Hβ ratio, thus indicating there is no relevant star formation taking place in these galaxies.

4.2.4 Hβ vs. [OIII]5007 gas distributions in NGC 5850

NGC 5850 is the only galaxy of the sample for which the gas distributions derived from the [OIII]5007 and Hβ emission lines are different. The corresponding maps are shown in Figure 4.8: whereas the [OIII]5007 distribution matches well with the stellar intensity distribution, the Hβ map shows the maximum off-centred with respect to the stellar isodensity contours. However, this difference is not translated into kinematical differences, since the gas velocity and velocity dispersion maps obtained from the two emission lines are very similar.

The position of the Hβ emission peak in NGC 5850 corresponds to a small potential star-forming region, as indicated by the [OIII]/Hβ ratio map also shown in Figure 4.8 and already introduced in Section 4.2.3. As mentioned, the relative values of the [OIII]/Hβ distribution may indicate the presence of

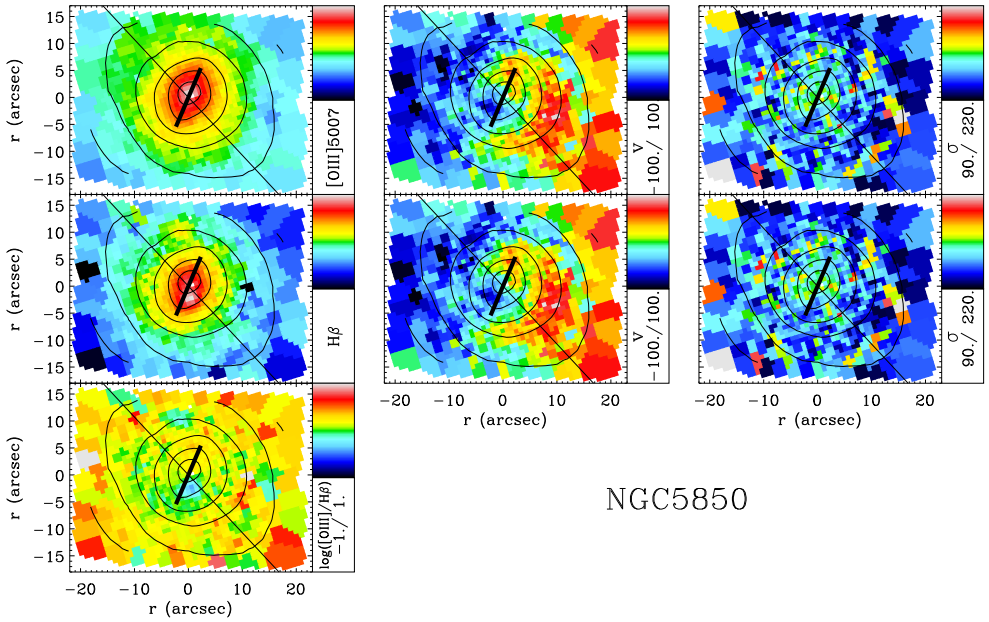

FIGURE 4.8— Gas intensity (arbitrary units; left column), velocity (in $\mathrm{km\,s^{-1}}$; middle column), and velocity dispersion (in $\mathrm{km\,s^{-1}}$; right column) maps derived from the [OIII]5007 (top row) and the Hβ (middle row) emission lines for the galaxy NGC 5850. The gas intensity distributions are different, with the Hβ peak off-centred with respect to the stellar intensity which is highlighted through its isodensity contours. The left-bottom panel shows the [OIII]/Hβ ratio for the same galaxy, which presents a small potential star-forming region at the position of the maximum Hβ emission. The lines indicate the position and size of the inner (thick line) and outer (thin line) bars.

potential star-forming regions, although an absolute interpretation of the results would require the measurement of other line ratios. The very small region which shows up in the flat, high [OIII]/Hβ map of NGC 5850 presents lower ratio values, thus indicating that it might be forming new stars, whereas the rest of the galaxy presents no signatures of relevant star formation structures.

5

Stellar populations

An archaeologist is the best husband a woman can have.
The older she gets the more interested he is in her
Agatha Christie

The main novelty introduced by this work is the detailed study of the stellar population properties of the double-barred sample. As explained in Chapter 1, high-quality spectra and a careful analysis using relevant state-of-the-art techniques are necessary to derive the age, metallicity, and abundance distributions of such structurally complex objects, and only this kind of analysis can shed light on the formation and evolution of double-barred galaxies. In the present Chapter we show the stellar populations results obtained from the SAURON data and we will discuss the implications of the observational evidence in the framework of the different formation scenarios of double bars and the role of inner bars in secular evolution.

5.1 Measurement of the line-strength indices

In order to investigate which stellar populations are shaping double-barred galaxies, we measure the most relevant absorption line-strength indices over the emission-cleaned spectra covering the full SAURON FoV. First of all, it is necessary to homogenise all the spectra to the same resolution, so it will be possible to later compare the results from the different bins and galaxies. Therefore, we degrade the data to a total width of 8.4 Å (FWHM), thus matching the LIS-8.4 Å system proposed by Vazdekis et al. (2010). This new LIS system introduces several advantages with respect to the traditional Lick/IDS spectral system (Worthey et al., 1994): it allows us to choose between three possible

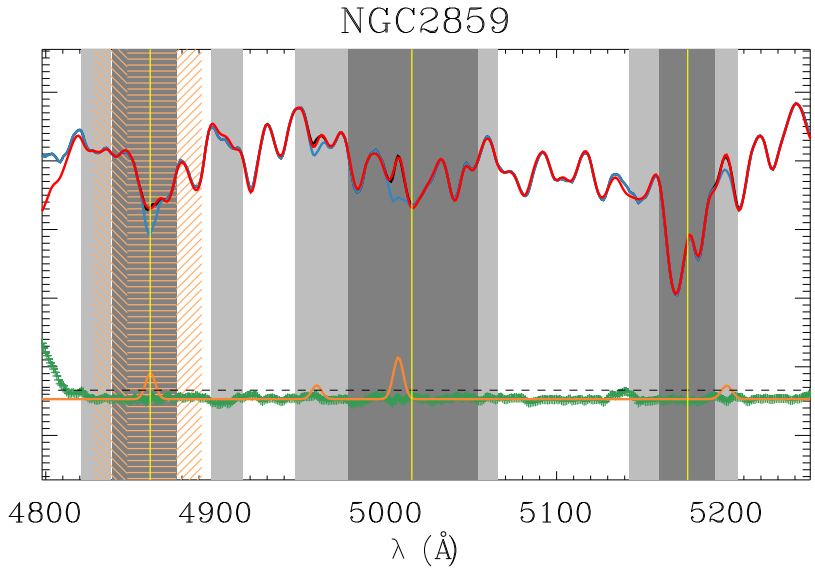

FIGURE 5.1— Full-spectrum fitting for the central spaxel of the galaxy NGC 2859, indicating the definitions of the indices measured in this work. The central bandpasses of the Lick indices Hβ, Fe5015, and Mgb are shaded in dark gray from left to right, respectively, whereas their corresponding pseudocontinua are coloured in light gray. The definition of the Hβ_o index is shown by the hatched orange regions: horizontal lines indicate the central bandpass whereas the angled lines are the pseudocontinua. Yellow vertical lines indicate the central position of each feature (4861Å for Hβ, 5015Å for the corresponding Iron index, and 5177Å for Mgb). Black and blue lines represent the original and the neat spectra, respectively, whereas the red spectrum is the best fit. The green crosses are the residuals and the emission contribution is overplotted in orange.

resolutions (5.0,8.4, and 14 Å), depending on the intrinsic velocity dispersion of the object under study (globular clusters, dwarf and intermediate-mass galaxies, and massive galaxies, respectively); moreover, it avoids the well-known problems with the wavelength dependence of the resolution and the correction to the instrumental response curves of the Lick/IDS system (Worthey & Ottaviani, 1997).

In particular, we calculate the age-sensitive Hβ and the metallicity-sensitive Mgb and Fe5015 indices, following the Lick definitions given by Trager et al. (1998). In addition, we also measure the Hβ_o index defined by Cervantes & Vazdekis (2009); this index shows greater ability to disentangle ages and thus helps to split the age-metallicity degeneracy. Figure 5.1 shows the definitions of the different indices measured for this work on one of the galaxy spectra.

To estimate the total metallicity, we compute the [MgFe50]′[1] index, defined by Kuntschner et al. (2010). [MgFe50]′ has been proved to be a good metallicity indicator, almost insensitive to the [Mg/Fe] overabundance; the use of this index has been growing, especially by users of the SAURON spectrograph (see for example Ganda et al., 2007), since it does not need the measurements of the Fe5270 and Fe5335 indices which lie out of the SAURON spectral range.

5.2 Line-strength maps

The maps showing the Hβ, Hβ_o, Mgb, and Fe5015 line-strength indices for the double-barred sample in the LIS-8.4 Å system are included in Appendix A, but one age-sensitive (Hβ_o) and one metallicity-sensitive ([MgFe50]′) indices are shown for each galaxy in Figure 5.2. We note that the two metallicity-sensitive indices, Mgb and Fe5015, present slightly higher values in the regions of the inner bars. This suggests that inner bars might be more metal-rich than their surroundings, as confirmed by the total metallicity indicator [MgFe50]′ maps shown in Figure 5.2. Further evidence in favour of this result will be given in Section 5.3.

Concerning the age-sensitive indices maps, Hβ and Hβ_o, they also show weak evidence of a distinct structure corresponding to the inner bar for the four galaxies. In fact, the inner bar regions seem to present higher Hβ and Hβ_o values than the surroundings, which indicates they are slightly younger. As for the metallicity, a detailed study of the age distribution such as that performed in Section 5.3 is needed to better analyse this parameter.

5.3 Mean luminosity-weighted age and metallicity distributions

Assuming that each galaxy spectrum corresponds to a single-age and single-metallicity stellar population, it is possible to derive these parameters by comparing the line-strength measurements with the corresponding predictions from the SSP models. Of course, the single-age and metallicity derived in this way are mean luminosity-weighted values; this approach represents a good method to constrain the formation and evolution of the galaxies, as younger components are highlighted even if their contribution in mass is not so important when compared to the older, underlying population. Therefore, such an analysis allows us to distinguish between a passive evolution and a more complex star formation history of the galaxies.

As for the kinematics, in the stellar population analysis we use the stellar population models of Vazdekis et al. (2010), built from the MILES stel-

[1] $[\mathrm{MgFe50}]' = \frac{0.69 \times \mathrm{Mg}b + \mathrm{Fe5015}}{2}$

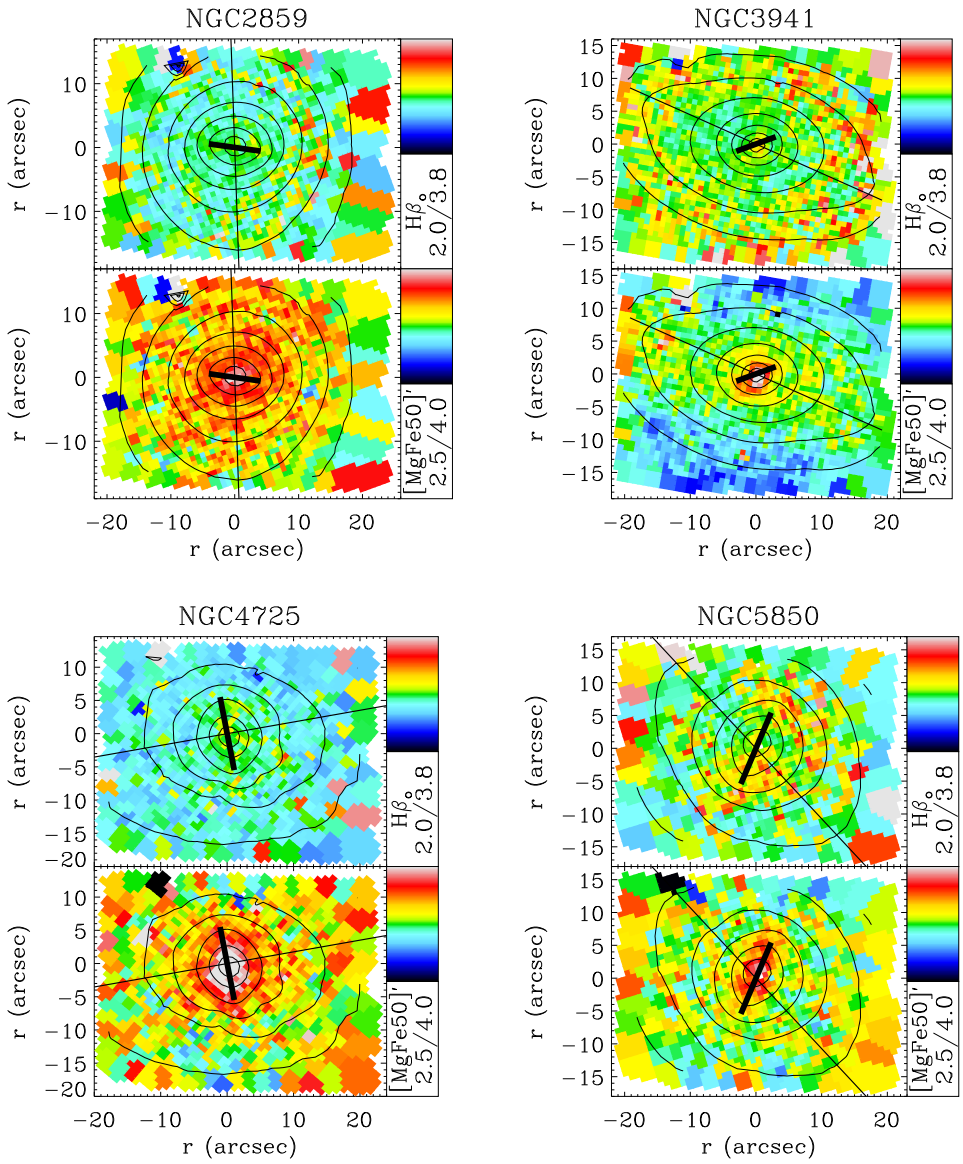

FIGURE 5.2— Hβ_o (top panels) and [MgFe50]′ (bottom panels) index distributions for the double-barred sample (from left to right and from top to bottom: NGC 2859, NGC 3941, NGC 4725, and NGC 5850). The higher values that both indices present in the inner bar regions indicate that they are younger and more metal-rich than their surroundings. The lengths and position angles of the inner and outer bars are indicated by thick and thin lines, respectively. We have also overplotted the contours of the reconstructed total intensity maps.

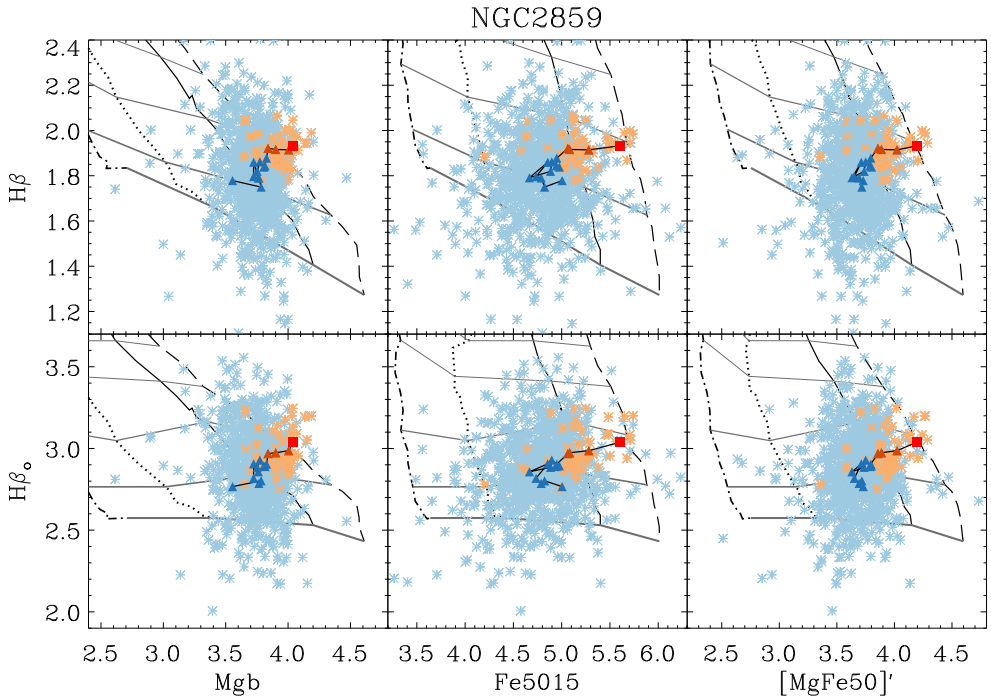

FIGURE 5.3— Age indicators Hβ and Hβ_o (from top to bottom) versus the metallicity indicators Mgb, Fe5015, and [MgFe50]′ (from left to right). The grids correspond to the SSP models by Vazdekis et al. (2010). The solid lines represent different ages increasing from top to bottom (2.5, 3, 5.6, 10, and 18 Gyr, respectively), whereas the almost vertical lines indicate different metallicities increasing from left to right ([Z/H]= -0.7, -0.4, 0.0, and 0.2, respectively). The asterisks are the measurements for all the spectra of NGC 2859, distinguishing the bins corresponding to the inner bar (orange asterisks) and the bins corresponding to the outer bar (pale blue asterisks). The triangles represent the measurements over ellipses of the same position angle and ellipticity as the inner bar (orange triangles), and the outer bar (blue triangles). The red square corresponds to the innermost ellipse, with a semi-major axis of just 1 arcsec. Both model and galaxy measurements are done in the LIS-8.4 Å system.

lar library (Sánchez-Blázquez et al., 2006), and with a spectral resolution of 2.51 Å (FWHM), constant over the whole spectral range (Falcón-Barroso et al., 2011). As with the data, the model spectra were previously smoothed to match 8.4 Å (FWHM), so all the measurements are performed in the same LIS-8.4 Å system.

By plotting the SSP predictions for an age indicator versus those for a metallicity indicator, we derive model grids such as those shown in Figures 5.3, 5.4, 5.5, and 5.3 for each galaxy. These grids are not perfectly orthogonal due to the

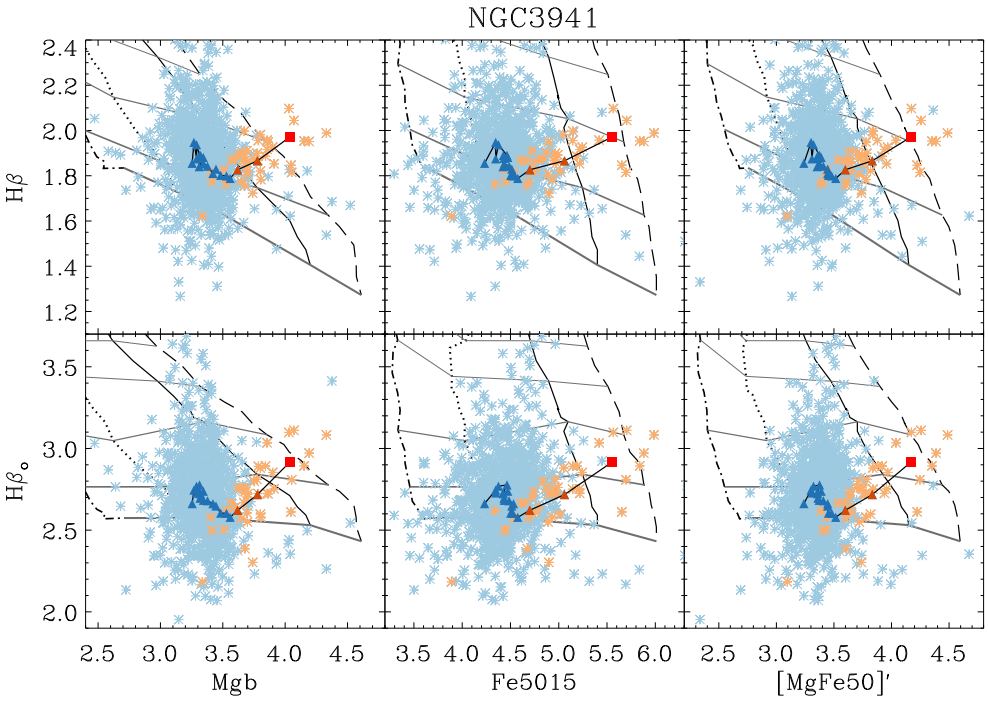

FIGURE 5.4— Same as Figure 5.3 but for NGC 3941.

age-metallicity degeneracy, which means that each index, although more sensitive to one parameter, is always dependent on both age and metallicity. The stellar population content of the galaxies can be then estimated by overplotting their corresponding line-strength measurements..

Figures 5.3, 5.4, 5.5, and 5.6 show the analysis for NGC 2859, NGC 3941, NGC 4725, and NGC 5850, respectively. The measurements corresponding to the inner bar and the surroundings, i.e., the outer bar, are highlighted in different colours. Since SAURON obtains over 1000 spectra in total, we use the Kinemetry program (Krajnović et al., 2006) in order to extract the line-strength measurements over the most suitable ellipses, which are fixed by providing their PAs and ellipticities to Kinemetry. In particular, we select the PA and ellipticity of the inner bar within its semi-major axis length, and the PA and ellipticity of the main bar further out. The results are then overplotted in Figures 5.3, 5.4, 5.5, and 5.6.

The four double-barred galaxies present a trend outwards towards greater ages and lower metallicities. This gradient is specially notable for the central

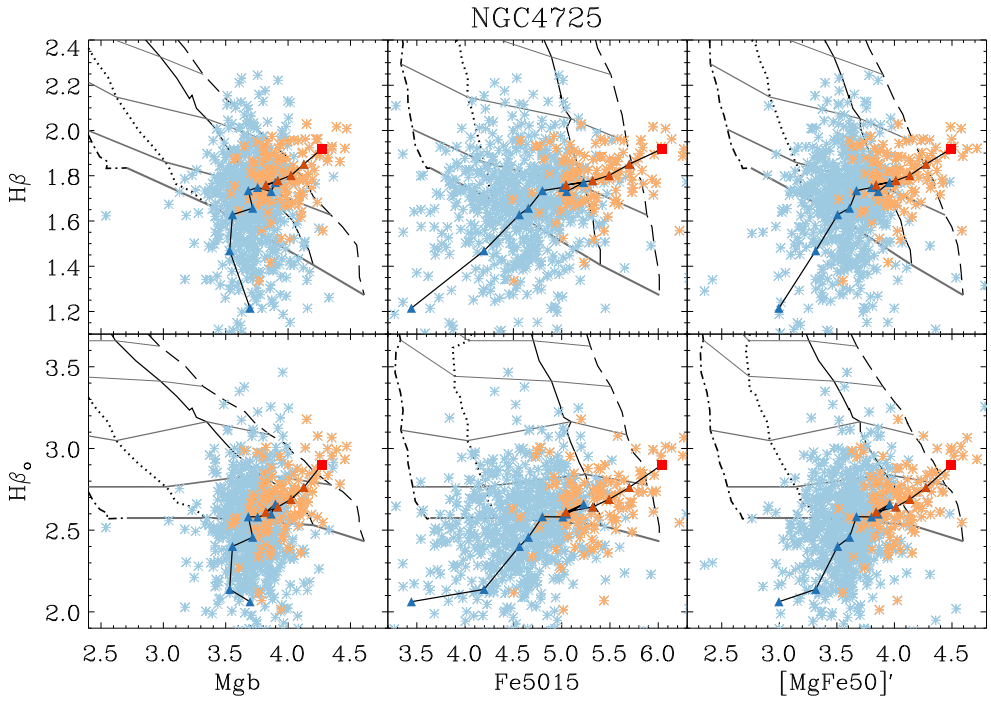

FIGURE 5.5— Same as Figure 5.3 but for NGC 4725.

regions, in particular for the ellipses corresponding to the inner bar. The central ellipse is always the youngest and the most metal-rich, whereas the points belonging to the outer bar present more similar ages and metallicities among them. The only exception is the case of NGC 4725, for which the gradient in age is extended towards the edge of the FoV.

Since double-barred galaxies are structurally complex and the two dimensional information is crucial, we also create age and metallicity maps to investigate the distribution of the stellar populations. Therefore, we adapted the rmodel[2] code (Cardiel et al., 2003), specifically developed for this kind of stellar population analysis, in order to perform a bivariate interpolation of the Hβ versus [MgFe50]$'$ grids included in Figures 5.3, 5.4, 5.5, and 5.6. The resulting age and metallicity maps for the four double-barred galaxies are shown in Figure 5.7. The four inner bars appear slightly younger and more metal-rich than their surroundings, thus confirming the results obtained from the previous analysis.

[2]Available at www.ucm.es/info/Astrof/software/rmodel/rmodel.html

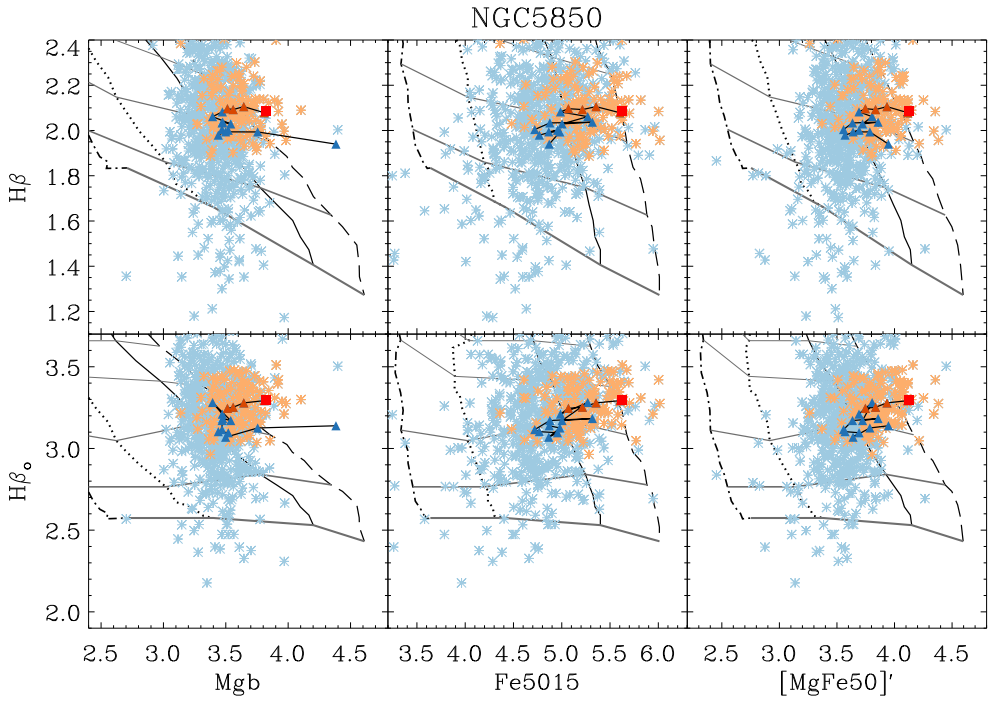

FIGURE 5.6— Same as Figure 5.3 but for NGC 5850.

The implications of this distinct stellar population content for the inner bar are discussed in Section 5.6.

5.4 [Mg/Fe] overabundance distributions

[Mg/Fe], [CN/Fe], and other similar abundance ratios are fundamental parameters in a stellar population analysis, as they act as chemical clocks and allow us to infer the formation timescales of the bulk of the stellar population and constrain the assembly history of the galaxies. In fact, the α elements, such as Mg, are created in type II supernovae, which explode on short timescales after the formation of their host stars; on the contrary, the Iron-peak elements are ejected by type Ia supernovae, on typical scales of around 1 Gyr.

In an analogous way as done in Section 5.3 for the [MgFe50]′ index, it is possible to derive the Mgb and Fe5015 metallicity distributions from the interpolation of the corresponding Hβ vs. Mgb and Hβ vs. Fe5015 model grids also shown in Figures 5.3, 5.4, 5.5, and 5.6. The [Z_{Mgb}/Z_{Fe5015}] ratio

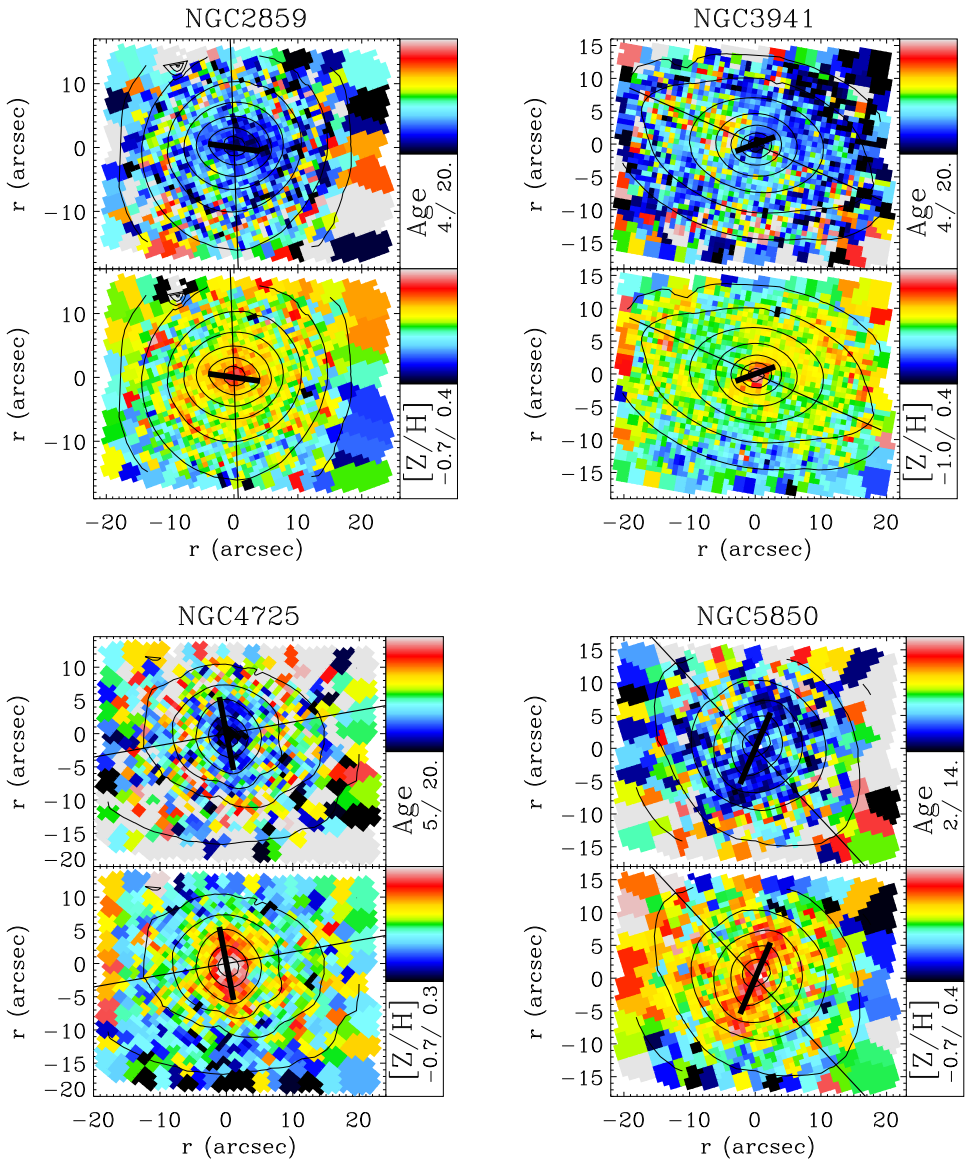

FIGURE 5.7— Age (in Gyr; top) and metallicity (bottom) maps for NGC 2859, NGC 3941, NGC 4725, and NGC 5850 (from left to right and top to bottom, respectively). The maps are the result of interpolating the Hβ versus [MgFe50]$'$ grids shown in Figures 5.3, 5.4, 5.5, and 5.6. For the sake of clarity, we have overplotted the position angle and length of the inner (thick line) and outer (thin line) bars, and the contours of the reconstructed total intensity map. The inner bars appear clearly younger and more metal-rich than their surroundings.

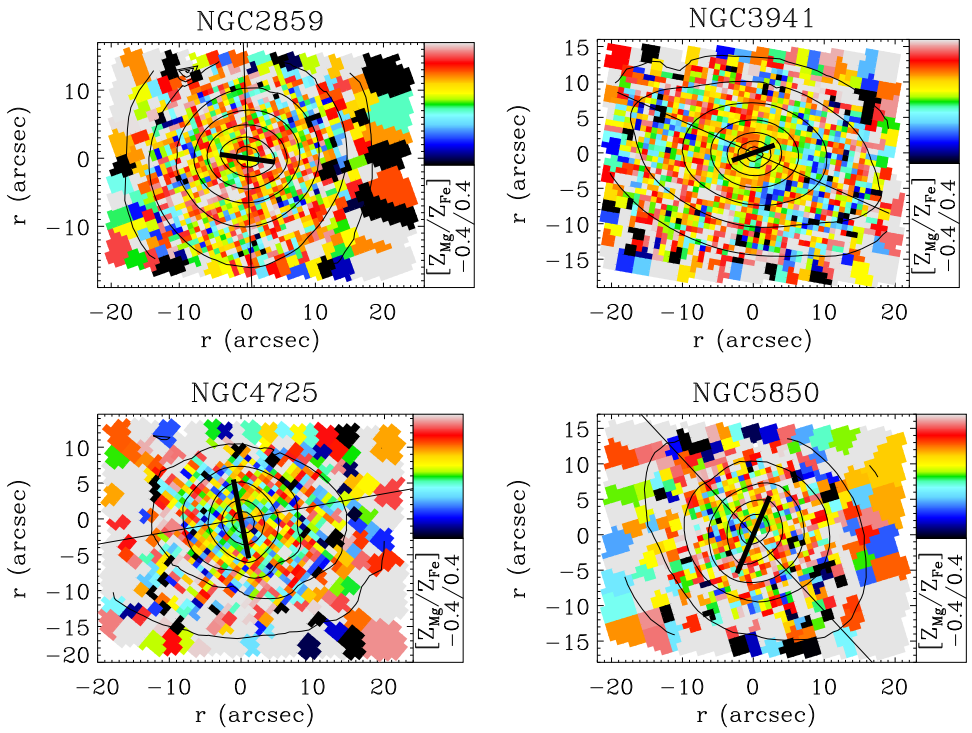

FIGURE 5.8— $[Z_{Mg}/Z_{Fe}]$ maps derived in a heuristic way by subtracting the Hβ vs. Mgb and the Hβ vs. Fe5015 metallicity maps. The position angle and length of the inner and outer bars are indicated as a thin and thick lines, respectively. We have also overplotted the contours of the reconstructed total intensity map. The $[Z_{Mg}/Z_{Fe}]$ distributions show no significant structures, nor correlations with the inner or outer bars regions.

distribution can be then obtained in a heuristic way by subtracting the two metallicity maps. $[Z_{Mgb}/Z_{Fe5015}]$ can be considered a proxy of the [Mg/Fe] overabundance, as a linear relation between the two ratios is expected (Peletier et al., 2007; Vazdekis et al., 2010); note however that the absolute values of this $[Z_{Mg}/Z_{Fe}]$ measurements are not the same as those used by other authors, who usually take combined Iron-indices, such as Fe3[3] (e.g., Thomas et al., 2011; de La Rosa et al., 2011). In the following, we will refer to our [Mg/Fe] estimate as $[Z_{Mg}/Z_{Fe}]$.

Given the short dynamical range of the [Mg/Fe] parameter, which typically acquires values between 0.0 (i.e., solar abundance) and 0.4, this kind of maps are naturally noisier than single index maps. The final $[Z_{Mg}/Z_{Fe}]$ overabundance

[3] $\mathrm{Fe3} = \frac{\mathrm{Fe4383+Fe5270+Fe5335}}{3.}$

distributions for the four double-barred galaxies are shown in Figure 5.8. They present flat distributions dominated by supersolar values. Moreover, we find no significant structures inside the inner nor the outer bar regions. As expected, the overabundance maps show a rather high scatter so an analysis such as that performed in Section 5.4.1 and Section 5.5, in which we calculate the $[Z_{Mg}/Z_{Fe}]$ radial profile and then integrate this parameter in the regions of interest, provides clearer results.

5.4.1 Radial profiles of the stellar population properties

In order to study the behaviour of the stellar population parameters from the inner to outer regions, we have also derived the age, metallicity, and $[Z_{Mg}/Z_{Fe}]$ radial profiles of our four double-barred galaxies. For this purpose we recover the PAs, ellipticities, and semi-major axes of the best fitting ellipses to the flux maps calculated in Chapter 3, and run Kinemetry again over the age, metallicity, and $[Z_{Mg}/Z_{Fe}]$ maps of Figure 5.7 and Figure 5.8 in order to get the mean values of those parameters around the isophotes. Figure 5.9 shows the resulting radial profiles: the four double-barred galaxies present a positive gradient in age outwards, whereas the metallicity gradient is negative, with the notable exception of NGC 3941 which shows the same gradients inside the inner bar regions but its profiles are quite flat along the outer bar.

Pérez et al. (2009) obtain the mean age and metallicity gradients along the main bars for a sample of 20 barred galaxies, 8 of them being double-barred systems with one, NGC 2859, in common with our present sample. As explained in Chapter 1, they find out that main bars show both positive and negative age and metallicity gradients with no correlation between the two parameters, although there is a trend for bars with negative metallicity gradients to show positive age gradients, as in the general case of the galaxies presented here. Even among the double-barred galaxies of the Pérez et al. (2009) sample there are no clear correlations, with 50% of their double-bars showing positive age gradients, and also 50% with positive metallicity gradients. Although the variety of possibilities obtained by Pérez et al. (2009) is in contrast with our findings, which show a homogeneous trend so the four double-barred galaxies have the same type of gradients, both results are in full agreement when taking into account the stellar velocity dispersion of the galaxies. In fact, Pérez et al. (2009) find a correlation between the metallicity gradient and the maximum central velocity dispersion values of the galaxies: negative gradients tend to appear in galaxies with the lowest central stellar velocity dispersions. They put the limit at $\sigma \sim 170$ km s^{-1}. Figure 4.1 shows that our four double-barred galaxies have maximum central velocity dispersion values ranging between 140

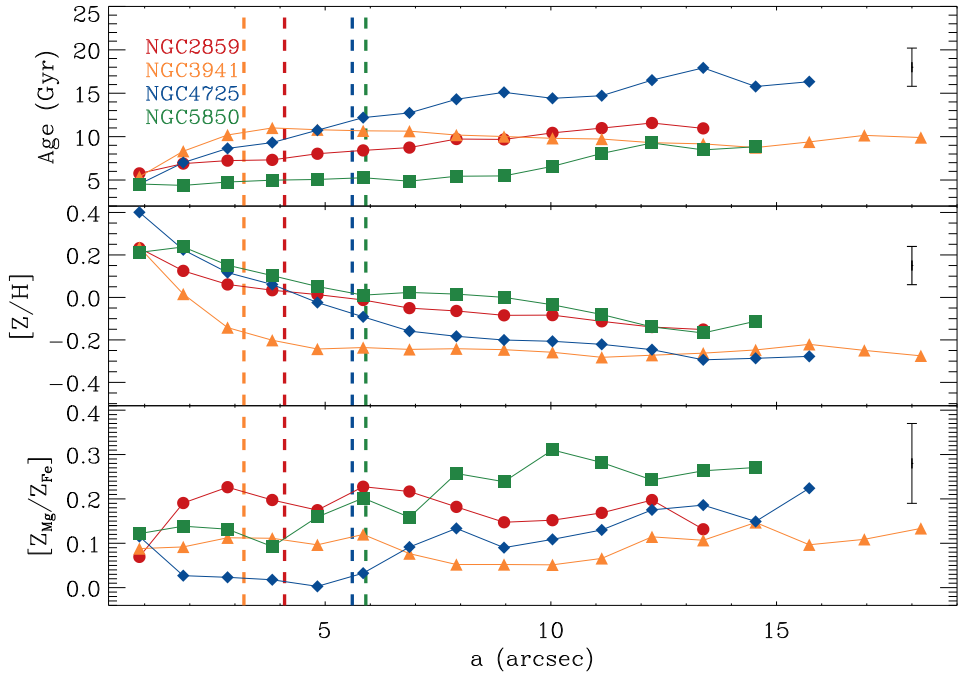

FIGURE 5.9— Mean age (top panel), metallicity (middle panel), and $[Z_{Mg}/Z_{Fe}]$ (bottom panel) profiles measured over the best fitting ellipses of the corresponding intensity map. The x-axis represents the semi-major axes of the ellipses. Different colors and symbols correspond to different galaxies: NGC 2859 (red circles); NGC 3941 (yellow triangles), NGC 4725 (blue diamonds), and NGC 5850 (green squares). Vertical dashed lines indicate the length of the inner bar, as given in Table 2.1 in Chapter 2. The mean error bar of each parameter is represented in the top right corner of each panel; note that the actual error for the inner ellipses is in fact lower than the plotted bar. The positive and negative gradients outwards in age and metallicity, respectively, are evident, whereas the $[Z_{Mg}/Z_{Fe}]$ profile shows a slight trend towards lower values in the very central regions.

and 160 km s^{-1}, except NGC 2859 which shows a central σ slightly above 170 km s^{-1}. It is also worth noting that the radial profiles shown by Pérez et al. (2009) for NGC 2859 are fully consistent with those of Figure 5.9.

The $[Z_{Mg}/Z_{Fe}]$ ratio radial profiles are rather flat with values ranging between 0.0 (i.e., solar abundance) and 0.3 dex, also in agreement with the results of Pérez et al. (2009). The galaxies show a slight trend towards a positive gradient, so the central regions present lower values of the $[Z_{Mg}/Z_{Fe}]$ overabundance. This feature is not present in the $[Z_{Mg}/Z_{Fe}]$ maps, proving the importance of analysing the data in different ways. The implications of this finding will be discussed in Section 5.6.

5.5 The stellar populations of each structural component

The last approach we have made use of to analyse the stellar population content of the double-barred galaxies is to obtain the mean luminosity-weighted age, metallicity, and $[Z_{Mg}/Z_{Fe}]$ values in three regions of interest: a central region defined as a circle of radius 1 arcsec; the inner bar, defined as an ellipse with the corresponding PA, ellipticity, and semi-major axis characteristic of each inner bar (the corresponding values are given in Table 2.1 in Chapter 3) and the outer bar region, which is defined as an ellipse with the PA and ellipticity of the corresponding outer bar as given in Table 2.1 (Chapter 3) and a semi-major axis that is 5 arcsec longer than the semi-major axis length of the inner bar. With this last criterion we ensure that the outer bar region is inside the SAURON FoV and we avoid the outermost bins that present lower S/N ratio. Figure 5.10 shows the mean values of the parameters in the bins inside each region of interest, with the corresponding dispersion represented by the error bars. Note that the general trends shown in Section 5.4.1 appear also among structural components, the inner structures being always younger and more metal-rich than the outer ones, as seen in the age and metallicity maps of Figure 5.7. This conclusion is also true for NGC 3941, which shows flat age and metallicity radial profiles along the outer bar; moreover, this galaxy presents the smallest inner bar so Figure 5.10 confirms the general conclusion which is more difficult to appreciate in the age and metallicity maps.

The $[Z_{Mg}/Z_{Fe}]$ ratios for the central, inner bar, and outer bar regions also show the previously observed trend towards lower values in the central structures. Note that the four galaxies have a central abundance ratio almost solar, with $[Z_{Mg}/Z_{Fe}] \sim 0.05$ dex. It is known that ellipticals tend to have enhanced abundance ratios (e.g., Worthey et al., 1992), and that bulges of many early-type spirals mimic the α-enhancement of ellipticals with the same velocity dispersion (e.g., Jørgensen, 1999; Kuntschner, 2000; Vazdekis et al., 2004; Carretero et al., 2004). Following this relation, early-type spirals with central stellar velocity dispersions of 140-180 km s^{-1} should present [Mg/Fe]$\sim$ 0.2-0.4 dex, above the central values found for our double-barred sample and closer to the mean abundance ratios of the bars.

5.6 The significance of these results...

5.6.1 ... for the formation of inner bars

The formation of double-barred galaxies has been a matter of discussion since two decades ago. In Chapter 1 we review the previous work addressing this issue, showing that most of it is based on numerical simulations which usually require the presence of a dissipative component, i.e., gas content, which is dy-

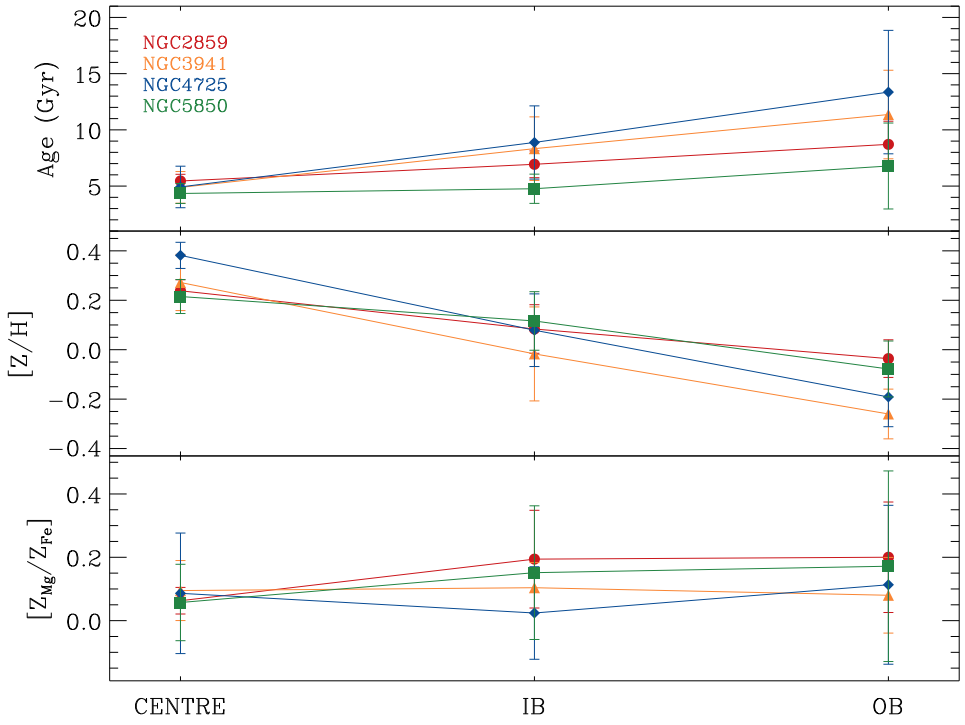

FIGURE 5.10— Mean age (top panel), metallicity (middle panel), and $[Z_{Mg}/Z_{Fe}]$ (bottom panel) values for the regions corresponding to a central circle with a 1 arcsec radius (CENTRE), the inner bar (IB), and the outer bar (OB), taken as an ellipse with the characteristic ellipticity and position angle of the outer bar and a semi-major axis 5 arcsec longer than the semi-major axis of the inner bar. Different colors and symbols correspond to different galaxies: NGC 2859 (red circles); NGC 3941 (yellow triangles), NGC 4725 (blue diamonds), and NGC 5850 (green squares). The error bars indicate the dispersion of the values inside each region. The positive and negative gradients outwards in age and metallicity, respectively, are evident. The $[Z_{Mg}/Z_{Fe}]$ distribution shows a slight trend towards lower values at the centre.

namically disturbed in order to form the inner bar. In fact, Friedli & Martinet (1993) try to develop double-barred systems with numerical simulations including only a purely collisionless component; they conclude that the presence of the gas is needed in order to form the two bars. Once the gas is included, they obtain two different types of models, one in which the two bars form simultaneously, the other in which the inner bar is formed after (and due to) the main bar. These two bars rapidly decouple and rotate with different pattern speeds, as has been confirmed by observations (Corsini et al., 2003). However, the final systems are not long-lived since at least the inner bar is diluted after

just 1-2 Gyr.

Since 1993, several studies have succeeded in simulating double-barred systems: Heller et al. (2001); Shlosman & Heller (2002); Rautiainen et al. (2002); Englmaier & Shlosman (2004); Heller et al. (2007). Their simulations are all gas-rich and create the inner bar after the main bar, because the gas flows along the outer bar and is captured by its x_2 orbits, subsequently decoupling and shaping the inner bar. Within this scenario, it is predicted that inner bars should be younger and probably more metal-rich than their surroundings.

The evidence presented in this work seem to support the bulk of the simulations which need gas to form the inner bars. In Chapter 4 we present the analysis of the emission lines of the four double-barred galaxies, which reveals that they contain gas and that this is probably flowing towards the central regions. Moreover, our inner bars have turned out to be slightly younger and more metal-rich than their surroundings (i.e., the outer bar), which is compatible with an scenario in which the inner bar is formed from material that flew along the outer bar to the inner regions. The metallicity gradients found along the inner bars also support a recent formation of these structures: Friedli et al. (1994) investigate through numerical simulations the influence of gas flowing along stellar bars on the distribution of the elements, finding out that this kind of structures redistribute the angular momentum so any abundance gradient tends to be flattened. Assuming this prediction, the presence of metallicity gradients inside the inner bar region implies these structures have been formed recently. Note however that our inner bars are not really young systems, since they have ages ranging from 4 to 8 Gyr; these intermediate ages imply that inner bars are steady, long-lived systems, as expected from the high frequency of double-barred systems found in the Universe (Erwin & Sparke, 2002; Laine et al., 2002, see also Chapter 1).

In opposition to most other numerical studies, Debattista & Shen (2007) are able to create inner bars without the presence of any dissipative component. In order to achieve this goal they need the presence of a disc and a rapidly rotating bulge as initial guesses for their N-body simulations. Debattista & Shen (2007) create purely stellar inner bars prior to the main bars; however, they remark that this time sequence is a consequence of their initial conditions and state that in the real Universe most likely outer bars are formed first. The results for the double-barred galaxies presented in this work do not discard the Debattista & Shen (2007) scenario, since we find evidence for a rapidly rotating structure in three out of the four galaxies (i.e., the kinematically decoupled inner discs) and the results of the stellar population analysis are also compatible with this theory.

5.6.2 ... for the role of inner bars in galaxy evolution

Bars are non-axisymmetric components that redistribute the angular momentum of a galaxy, allowing the flow of material among them. As explained in Chapter 1, inner bars are thought to be key systems to transport gas to the very central regions, where they help to trigger the star formation and contribute to the creation of spheroidal structures. If this hypothesis is correct, double-barred galaxies are outstanding systems from a secular evolution point of view, since they promote the formation of bulges. Moreover, it has been theoretically demonstrated that inner bars allow the material to get to the innermost regions, where the gas flowing along a single bar is not able to reach (Boone et al., 2007, see also Chapter 1). Within this scenario, inner bars also contribute to the fueling of the AGNs (Shlosman et al., 1989, 1990, but see also Ho et al., 1997; Márquez et al., 2000).

As mentioned above and studied in Chapter 4, we have found evidence of gas content and flow towards the central regions, where it is likely that some star formation is taking place. This hypothesis is also backed by the fact that the centres of our four double-barred galaxies present somewhat lower [Mg/Fe] values than the inner bars and outer regions, which points towards a progressive, time-extended formation of these innermost regions. Nevertheless, this star formation seems to be not efficient nor strong enough to be determining the secular evolution of these four double-barred galaxies. In fact, the stellar populations of the bulge are not clearly distinguished from the stellar populations of the inner bar, and there is no really young stellar content in any of the galaxies. If inner bars were playing a major role in the formation of new structures at the central regions, these new structures should show up in a stellar population analysis such as that performed in this study. Moreover, the [OIII]/Hβ ratio maps shown in Figure 4.7 in Chapter 4 reveal flat distributions with slightly high values, indicating that there is no relevant star formation taking place in these galaxies. The only exception is a small and limited star-forming region in NGC 5850 (see Section 4.2.4 in Chapter 4 for details), but this is not of importance for the global picture. We therefore conclude that these four inner bars are not actually playing a major role in the secular evolution of their host galaxies.

From the four double-barred objects of this sample, only NGC 3941 and NGC 4725 are classified as Seyfert 2 galaxies (Véron-Cetty & Véron, 2006), whereas NGC 2859 and NGC 5850 present no signs of nuclear activity (see Chapter 2). In our analysis, we do not find differences between the galaxies which do or do not host an AGN, so we are not able to shed light on the role of inner bars in fueling the AGNs. The influence of the environment in double-barred gala-

xies is an analysis beyond the scope of this work, and this is the reason why the four objects were selected to be almost isolated, with NGC 2859 and NGC 3941 being field galaxies, and NGC 4725 and NGC 5850 belonging to a group. The results suggest there are no special correlations between the environment, the nuclear activity and the stellar populations of these double-barred objects.

6

The interesting case of NGC 357

...and it's been the ruin of many a poor boy,
and God, I know, I'm one
The house of the rising Sun (traditional American folk song)

The results presented in this Chapter have already been published in:
de Lorenzo-Cáceres et al. 2012, Monthly Notices of the Royal Astronomical Society, Volume 420, Issue 2, pp. 1092-1106

The fifth galaxy of the present double-barred sample, namely NGC 357, has turned out to show some structural differences compared to the rest of the galaxies, revealed only by the study performed here. Coincidentally, NGC 357 is the only galaxy of the sample observed with long-slit spectroscopy (see Chapter 2) and therefore its analysis has been carried out in a separate way and has been used to test and explore different state-of-the-art techniques. Given all these circumstances, we have devoted the present Chapter to describe the kinematics and stellar population analysis of NGC 357, including a discussion on the results and properties which convert it into the *ugly duckling*, or maybe the swan, of our sample.

6.1 Stellar kinematics

For NGC 357, we have focused on the kinematics of the stars, since the main goal of this thesis is to fully understand the behaviour and evolution of the stellar double-barred systems. Moreover, the long-slit data miss the spatial information, so it is not possible to explore the spiral structures in the gas for the case of this galaxy. Given the possibilities offered by the high-quality and

the large spectral range achieved due to the observations with both the red and blue arms of the EMMI spectrograph, we have taken advantage of this extremely good data to exploit and compare different analysis techniques thus reinforcing the accuracy of the results.

6.1.1 Measuring the line-of-sight velocity and velocity dispersion

Two different techniques were used to derive the velocity and velocity dispersion profiles of NGC 357: a cross-correlation in the Fourier domain and a full spectrum fitting in wavelength space. The cross-correlation procedure (e.g., Tonry & Davis, 1979) is as follows: among the observed velocity standards, we select those that are spectroscopically most similar to the galaxy. After correcting them to rest frame, we combine the stellar spectra to create an artificial velocity standard star spectrum that will be used as a template for the cross-correlation. This standard spectrum is then broadened to several different velocity dispersions and the results are correlated with the original star, obtaining for each case a cross-correlation peak with its full width half maximum (FWHM). Thus, we create a calibration table that provides the FWHM we expect if a spectrum with a given velocity dispersion is cross-correlated with our stellar template, so we can obtain the dispersion of the galaxy spectra by correlating them with the star. The line-of-sight velocity is a direct product of the correlation since the template is at rest.

For the full spectrum fitting we have made use of the pPXF routine developed by Cappellari & Emsellem (2004) and already introduced in Chapter 4. The spectral regions which are potentially affected by emission lines are previously masked on each galaxy absorption spectrum, which is then fitted with a linear combination of a well-selected subsample of the single SSPs of Vazdekis et al. (2010), previously convolved with a LOSVD. This LOSVD is parametrized by an expansion in Gauss-Hermite functions (Gerhard, 1993; van der Marel & Franx, 1993). Since the S/N requirements for this procedure become more demanding as the order of the desired LOSVD moments increases, we decided to focus only on the velocity and velocity dispersion to avoid the loss of spatial resolution caused by a wider radial binning.

The two methods used for deriving the kinematics of NGC 357 are completely independent and even work in different parameter spaces. In order to enhance the differences between the two techniques, we explore two different ways that offer complementary advantages: whereas the SSPs help to alleviate the template mismatch problem (Falcón-Barroso et al., 2003), the artificial template was obtained from stellar spectra, which were observed and reduced exactly in the same way as the galaxy spectra, thus minimising the possibility

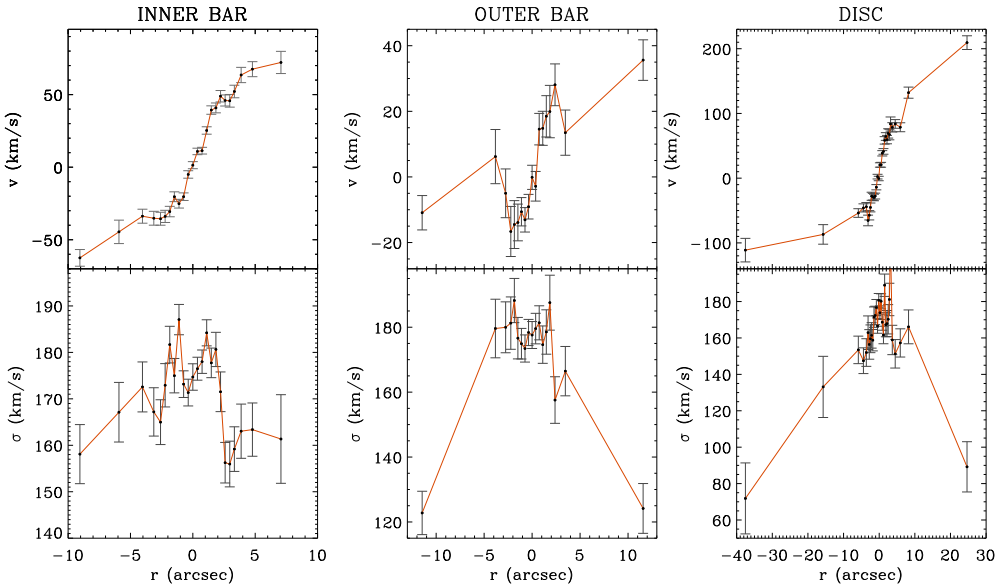

FIGURE 6.1— Line-of-sight velocity (after the systemic velocity subtraction; top panels) and velocity dispersion (bottom panels) profiles as a function of the radius for the spectra obtained along the major axis of the inner bar (left panels), outer bar (middle panels) and disc (right panels) of NGC 357.

of introducing instrumental effects.

The results obtained from both methods are fully consistent, with differences smaller than the corresponding error bars. These differences range from a few $\mathrm{km\,s^{-1}}$ in the central regions to a maximum of $10\,\mathrm{km\,s^{-1}}$ in the outermost observed radii. Figure 6.1 shows the final line-of-sight velocity (after subtracting the systemic velocity) and velocity dispersion profiles obtained with pPXF along the major axis of the inner bar, outer bar, and disc.

6.1.2 Revealing the inner and outer bars

The presence of the inner bar is clearly unveiled by the shape of the rotation curve (Figure 6.1, left panels), which follows the same characteristic *S*- or *double-hump* profile previously observed for inner bars by Emsellem et al. (2001). This profile is characterised by an inner steep slope so the rotation reaches a local maximum, it drops slightly to a local minimum and then it rises again slowly further out. Since the two bars of NGC 357 are almost perpendic-

ular, with the inner one almost parallel to the major axis of the galaxy, we can conclude that the double-hump profile in Figure 6.1 is completely due to the presence of the inner bar. This kind of rotation curve was derived theoretically by Chung & Bureau (2004) and Bureau & Athanassoula (2005) by means of N-body simulations of single-barred galaxies. In the latter article, the authors show that the double-hump structure is more enhanced in galaxies with strong bars seen end-on, whereas the effect is weakened for larger viewing angles or weaker bars. Although the double-hump rotation curve is clearly visible in the case of the inner bar of NGC 357, suggesting that the bar is strong, the maximum isophotal ellipticity is only $\epsilon_{max} \sim 0.15$, which indicates that it is actually a very weak bar. Indeed, the maximum ellipticity of the isophotes in a bar region correlates well with the bar strength (Laurikainen et al., 2002), although it is worth noting the degeneracy between ellipticity and length inherent in the bar strength estimate (see Chapter 1).

The velocity dispersion profile along the inner bar shows three local minima: a central drop corresponding to the so-called *σ-drop* of Emsellem et al. (2001), and two symmetric decreases exactly at the edges of the bar (± 4 arcsec) which can be identified as the *σ-hollows* already noticed in the four SAURON galaxies analysed in Chapter 4. These hollows have an amplitude of $\sim$20 km s^{-1}, consistent with the findings for the rest of the double-barred sample, which present amplitudes ranging from 10 to 40 km s^{-1}. Further discussion on these features and their different origins in NGC 357 is found in Section 6.3. As expected, the velocity dispersion decreases outwards.

The outer bar of NGC 357 (Figure 6.1, middle panels) is almost perpendicular to the major axis of the galaxy, which we assume to be the kinematical line of nodes. This means that the line-of-sight velocity values along the outer bar are expected to be very low, as it is shown in Figure 6.1. However, a clear kinematically decoupled profile appears in the central region. This structure rotates faster than its surroundings and extends $\sim \pm 2$ arcsec, which corresponds to the radial region of the σ-drop observed in the velocity dispersion profile. A closer inspection to the inner bar velocity profile reveals the same decoupling, since two steep humps appear inside the double-hump profile, exactly at $\sim \pm 2$ arcsec. Unfortunately, the low S/N level of the spectra along the direction of the outer bar of NGC 357 allows us to analyse the kinematics only in the inner $\sim \pm 10$ arcsec, so we cannot explore the whole main bar to see if other signatures, such as for example σ-hollows or a double-hump profile, are present.

The kinematics along the major axis of the disc are shown in Figure 6.1 (right panels). In this case, we find, as expected, the maximum line-of-sight velocity values and the same central signatures found for the other directions:

the decoupling in the velocity profile and the σ-drop. In Section 6.3 we discuss the possible structures that might be causing these signatures.

6.2 Stellar populations

As for the SAURON data, the aim of this stellar population analysis is to recover the relative ages, metallicities, and formation timescales of the different structural components of NGC 357: bulge, inner bar, and outer bar. Unfortunately, the quality of the data, although very high, still is not sufficient to analyse the disc, which requires spectra taken with 10 m-class telescopes. To perform this detailed study, we have summed up the individual spectra, previously corrected for their kinematics (velocity and velocity dispersion), to reach the desired S/N ratio within each structural component. For this purpose, we add only those spectra corresponding to the regions where a given component is clearly dominating the total luminosity: the inner ± 1 arcsec for the bulge, from ± 2 arcsec to ± 4 arcsec for the inner bar, and from ± 4 arcsec to $\sim \pm 15$ arcsec (limited in this case by S/N requirements) for the outer bar. Since the spectra along the major axes of the two bars and the disc always cover the central region, we have two spectra for the bulge in the blue and red spectral range, respectively. However, the bars were observed only in the blue spectral range.

Again, we have chosen two methods to analyse the stellar populations: the line-strength indices and a full spectrum-fitting approach. Instead of using the Lick/IDS system, we have chosen to perform our line-strength analysis on the system imposed by the kinematics of the galaxy, as in Vazdekis et al. (2001) and Yamada et al. (2006). For the second approach, we use the cross-correlation technique employed by Vazdekis (1999) and Vazdekis & Arimoto (1999).

In both cases, comparisons with stellar population synthesis models are needed; as in the rest of the studies (see Chapters 4 and 5, and Section 6.1), we have used the empirical models of Vazdekis et al. (2010), built from the MILES stellar library (Sánchez-Blázquez et al., 2006). These models have a wide wavelength coverage (from 3525 to 7500 Å) and a resolution of 2.51 Å (FWHM), constant over the whole spectral range (Falcón-Barroso et al., 2011).

6.2.1 Emission line correction

As explained in Chapter 4, the ionised gas present in the galaxy leads to emission lines that contaminate the spectrum and fill in the absorption lines. Therefore, it is crucial to correct for this emission to get the properties of the stellar populations from the spectra. Indeed, if a proper separation of both contributions (the stellar absorptions and gaseous emissions) is not performed before the analysis, the measured ages will be artificially greater. For the EMMI data,

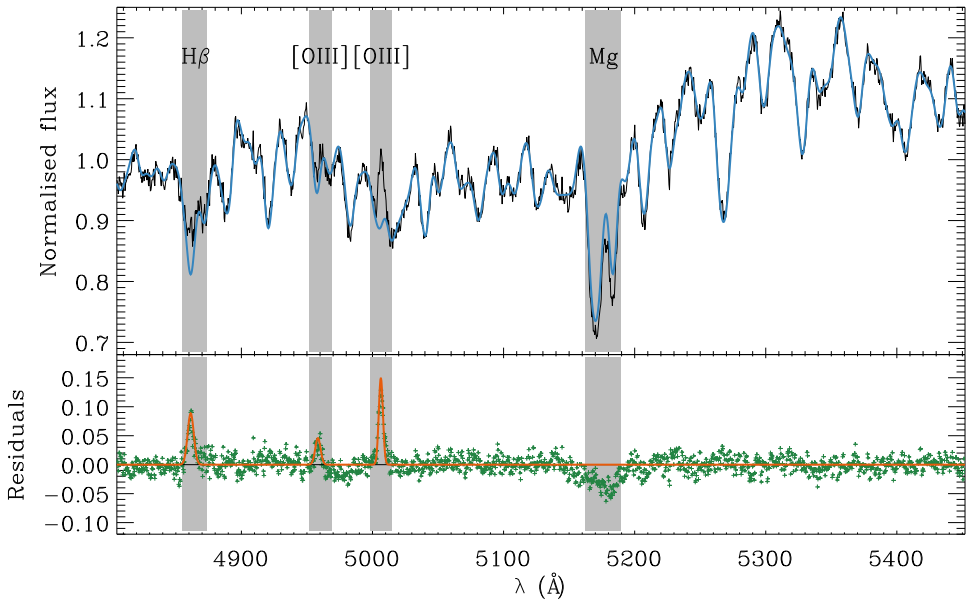

FIGURE 6.2— The correction of the emission lines in the red spectrum of the bulge of NGC 357 by means of ULySS. The observed and model spectra are plotted in black and blue, respectively in the upper panel. The shaded regions indicate the masking performed because of emission-line contamination (Hβ and [OIII]4959,5007 doublet) and α-enhancement (Mg). The residuals of the fit are shown in green in the lower panel. The Gaussians fitting the emission lines are plotted in orange.

we need to clean up the three Balmer lines included in our spectral range (Hβ, Hγ, and Hδ), and the Fe5015 and Mgb indices, which can be affected by the [OIII]4959,5007 and [NII]5198,5200 lines, respectively.

As a first approach for this correction we use the common procedure, which consists in masking the spectral region possibly contaminated by emission lines and, in turn, fitting the obtained spectrum with a set of stellar population models. For this purpose we use the ULySS[1] package (Koleva et al., 2009), which minimises the χ^2 between the observed spectrum and a model spectrum consisting of a linear combination of non-linear parameters (age and metallicity), corrected for the kinematics and multiplied by a polynomial to avoid flux calibration problems. We subtract the ULySS best fit spectrum to the original one in order to get the residuals plus the contribution of the emission lines. We then approximate each emission line with a Gaussian, considering only those features with an amplitude larger than three times the standard deviation of

[1] Available at http://ulyss.univ-lyon1.fr/.

the residuals.

Given the sensitivity of the emission correction, we double-check it by repeating it with the GANDALF package (Sarzi et al., 2006), as we did for the SAURON data in Chapter 4. The advantage of GANDALF is that it fits simultaneously the stellar and the gaseous contributions, by including emission lines as Gaussians in the set of stellar population models used as templates. Although GANDALF is also based on χ^2 minimisation, it differs from ULySS in that it fits the stellar contribution with a linear combination of models, while ULySS interpolates the grid of templates to look for the most appropriate single stellar population model.

There are many details to take care of when fitting the full spectrum, such as the initial guesses and the number and range of the masked regions. For example, in the case of the blue spectra of NGC 357, we are forced to mask the CN band as we find evidence of its α-enhancement (not included in the scaled-solar models of Vazdekis et al., 2010). When the amount of emission derived from the two routines is in agreement, we subtract it from the observed spectra and use the results for the analysis of the stellar populations. Figure 6.2 presents an example of the fitting performed with ULySS for the bulge red spectrum because it shows Hβ and [OIII]5007, which are the most prominent emission lines we observed.

6.2.2 Line-strength indices

A set of suitable absorption line-strength indices is measured in the emission-cleaned spectra of the bulge, inner bar, and outer bar, as well as in the spectra derived from the Vazdekis et al. (2010) models. In order to compare the results of the three components, the galaxy spectra and the SSPs are first degraded to their minimum resolution, given by the highest value of the velocity dispersion profile ($\sigma \sim$180 km s^{-1}). All the measurements are performed in the same system, i.e., the one defined by the kinematics of the galaxy in a consistent way. We plot the values obtained for an age indicator versus those of a metallicity indicator for the SSP models, in order to obtain model grids such as those shown in Figures 6.3 and in Sections 6.2.4 and 6.2.5. These grids are not perfectly orthogonal due to the age-metallicity degeneracy. The mean luminosity-weighted ages and metallicities of each structural component of NGC 357 can then be derived by simply overplotting the observed indices on these grids.

In particular, we computed all the Lick indices included in our spectral range, following the definitions given by Trager et al. (1998). It is important to emphasize that, although the index definitions are similar, our model measurements are not in the Lick/IDS resolution and IDS instrumental system, but at

TABLE 6.1— The definitions of the new Fe4383^{SR} and Lick/IDS Fe4383 (Trager et al., 1998) indices.

Index	Blue pseudo-continuum (Å)	Main bandpass (Å)	Red pseudo-continuum (Å)
Fe4383	4359.125-4370.375	4369.125-4420.375	4442.875-4455.375
Fe4383^{SR}	4359.125-4370.375	4369.125-4398.087	4419.328-4432.389

constant σ and with flux-calibration response curve imposed by the kinematics of the galaxy; this is also different to the LIS system used for the SAURON data in Chapter 5 (see Vazdekis et al., 2010, for the definition of the LIS system).

Since the red pseudo-continuum of the Fe4383 index falls partially out of our blue spectral range, we have defined a new Fe4383^{SR} index (named after *Short Red*) suitable for our spectral range requirements. Fe4383^{SR} keeps the blue pseudo-continuum of the Lick Fe4383 index, but modifies the range definitions for the main bandpass and the red pseudo-continuum. Table 6.1 presents the definitions of the new Fe4383^{SR} and the original Lick/IDS Fe4383 index.

This new index has been tested with the bulge of NGC 357, for which we have data in two spectral ranges so we can measure additional Iron indices. Figure 6.3 shows several age indicators plotted against Fe4383^{SR} and $\langle$Fe$\rangle$. The corresponding measurements for the bulge of NGC 357 are overplotted. The age and metallicity obtained from the two Iron index definitions are consistent. We therefore use Fe4383^{SR} for estimating the metallicity in our blue spectra.

For the bulge red spectrum, we compute the combined Iron-index $\langle$Fe$\rangle$ and total metallicity indicator [MgFe][2] (González, 1993). We avoid the use of the Fe5015 index, since it is highly contaminated by the prominent [OIII]5007 emission line.

In addition to the Lick age index-definitions for the Balmer lines (Hβ, Hγ and Hδ), we also measure the more powerful Hβ_o (Cervantes & Vazdekis, 2009) and Hγ_σ (Vazdekis & Arimoto, 1999) indices, which show great abilities to disentangle ages from metallicities. The use of indices with enhanced sensitivity to the age or metallicity represents an advantage to remove, at least partially, the degeneracy between these parameters.

[2] $\langle \text{Fe} \rangle = (\text{Fe5270} + \text{Fe5335})/2$, and $[\text{MgFe}] = \sqrt{\text{Mg}b \times \langle \text{Fe} \rangle}$

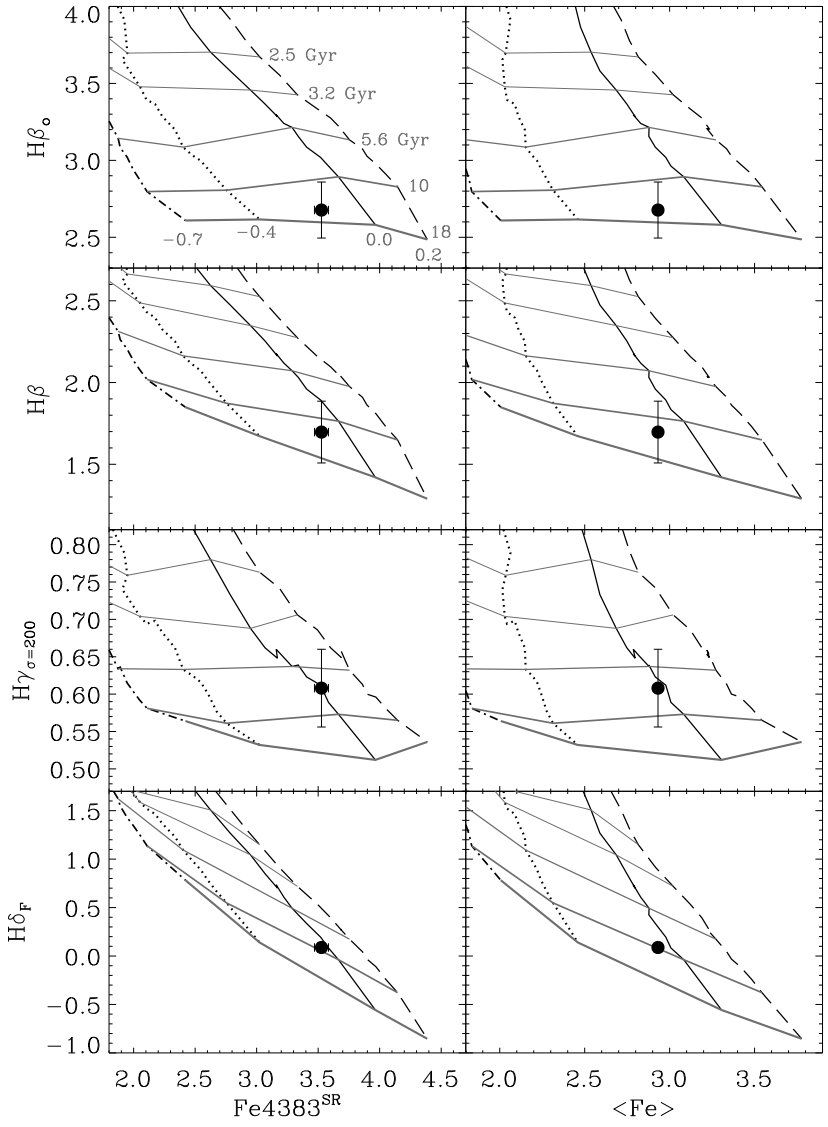

FIGURE 6.3— Comparison of the results obtained for the bulge of NGC 357 using as metallicity indicators the newly defined Fe4383^{SR} (left panels) and the ⟨Fe⟩ (right panels) indices, and several age-sensitive indicators (Hβ, Hβ_o, H$\gamma_{\sigma=200}$, and H$\delta_{\rm F}$, from top to bottom). The grids correspond to the SSP models of Vazdekis et al. (2010) once smoothed to match the resolution of the data ($\sigma \sim$180 km s^{-1}). The lines represent different ages increasing from top to bottom (2.5, 3.2, 5.6, 10, and 18 Gyr, respectively) and metallicities, which increase from left to right ([Z/H] = −0.7, −0.4, 0.0, and 0.2, respectively). Ages and metallicities for the grids are indicated in the first panel.

6.2.3 Cross-correlation analysis

The alternative technique we use to analyse the stellar populations of NGC 357 is to cross-correlate the galaxy spectrum with each SSP spectrum from the Vazdekis et al. (2010) model library. For this purpose the model spectra are previously prepared to match the spectral range, velocity dispersion, and spectral resolution of the data. Moreover, the galaxy and model spectra are rebinned logarithmically and normalised to remove the continua.

In order to optimize the cross-correlation method for disentangling different stellar populations, it is necessary to adequately filter the spectra and multiply them by a cosine-bell-like function (Tonry & Davis, 1979). The importance of choosing a suitable filter lies in the possibility of greatly reducing the noise in the spectrum; this purpose can be achieved by simply removing the largest wavenumbers, where the information about the shortest wavelength ranges is included. Therefore, the limit is imposed by the resolution of the data. On the other hand, shorter wavenumbers contain information about wider spectral ranges, so possible residuals of the continuum removal due to errors in the flux calibration might also be filtered. The drawback of this procedure is that it implies a power loss of the final cross-correlation function, specially when filtering small wavenumbers where most of the signal is included.

Apart from the filtering, it may be necessary to mask some regions in the original spectra, as is usually done in the full-spectrum fitting technique in wavelength space. We tested different masks trying to avoid those features that are not well reproduced by the models due to mismatched abundance ratios: the CN in the blue spectral range and the Mg and Hβ features in the red spectral range. Again, these features contain most of the signal of the power spectrum so the masks have to be chosen very carefully in order to not lose most of the information.

Finally, the peak height obtained for each correlation function is plotted against the model age and metallicity. Since the cross-correlation profile reaches a higher value when object and template are more similar (giving a maximum value of 1 if they are exactly the same and no filtering is applied), the maximum value in the final peak heights plot indicates which template best resembles the galaxy spectrum. This method takes advantage of the full information contained in the spectrum, instead of being constrained to certain features as in the case of the line-strength indices. This type of full-spectrum fitting technique works in the Fourier space and, as an additional advantage, it does not need a previous emission correction of the data. The application of this technique to the derivation of the stellar populations was introduced by Vazdekis (1999) and Vazdekis & Arimoto (1999) and in this study it is adopted to double-check the results obtained from the analysis of the line-strength indices.

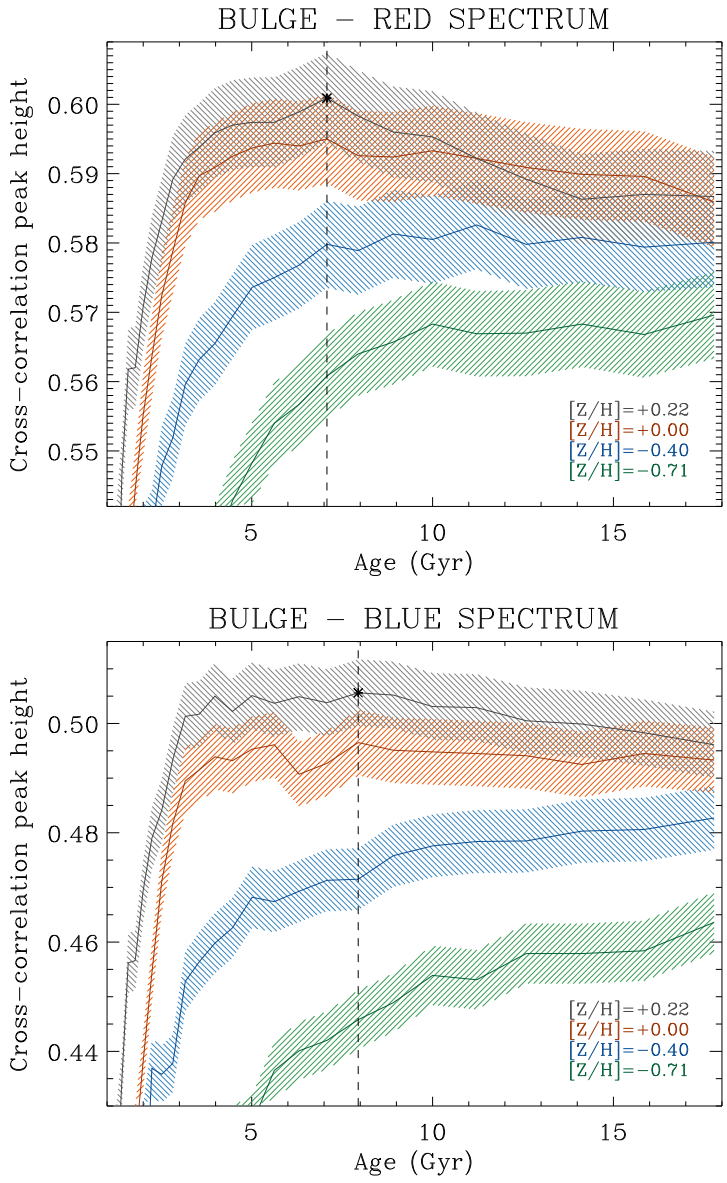

FIGURE 6.4— Cross-correlation peak heights from the analysis of the red (upper panel) and blue (lower panel) spectra of the bulge of NGC 357 with a set of SSP models of Vazdekis et al. (2010), once smoothed to match the spectral range, resolution, and dispersion of the data. The different coloured lines correspond to metallicities of [Z/H] = 0.2 (black), 0.0 (red), −0.4 (blue), and −0.7 (green) as a function of age. The width of the coloured region represents the 1-σ uncertainty derived from Monte Carlo simulations. The largest cross-correlation peak height value in each plot is marked by an asterisk and the corresponding age with a vertical dashed line.

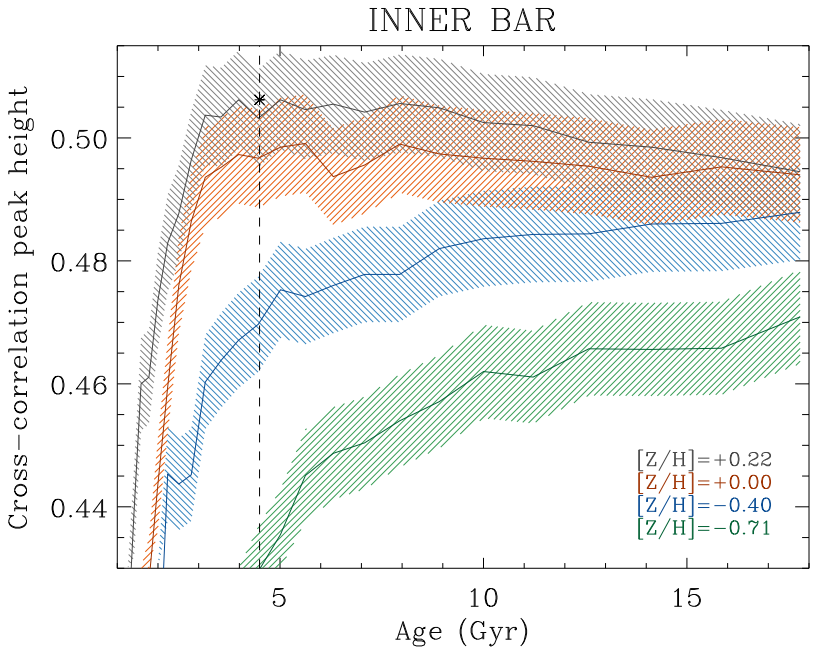

FIGURE 6.5— Same as in Figure 6.4 for the blue spectrum of the inner bar of NGC 357.

To compute the errors for the cross-correlation method we perform a set of 100 Monte Carlo simulations by randomly adding Gaussian noise to the data, keeping the original S/N ratio. The 1-σ regions are then overplotted on the cross-correlation peak height curves. The results for the bulge and the inner bar of NGC 357 are shown in Figures 6.4 and 6.5, and will be analysed in Sections 6.2.4 and 6.2.5, respectively.

In order to test the requirements of this method we run some simulations with the Vazdekis et al. (2010) models by artificially changing the different parameters involved: spectral resolution, spectral range, and S/N ratio, taking as a reference the values measured for our observed spectra. We find that the S/N of the data obtained for the outer bar is not enough to disentangle its age and metallicity, since the error bars for this case are too large. This is illustrated in Figure 6.6, where we show the results of applying the cross-correlation method to a model of 8 Gyr and solar metallicity, once cut and

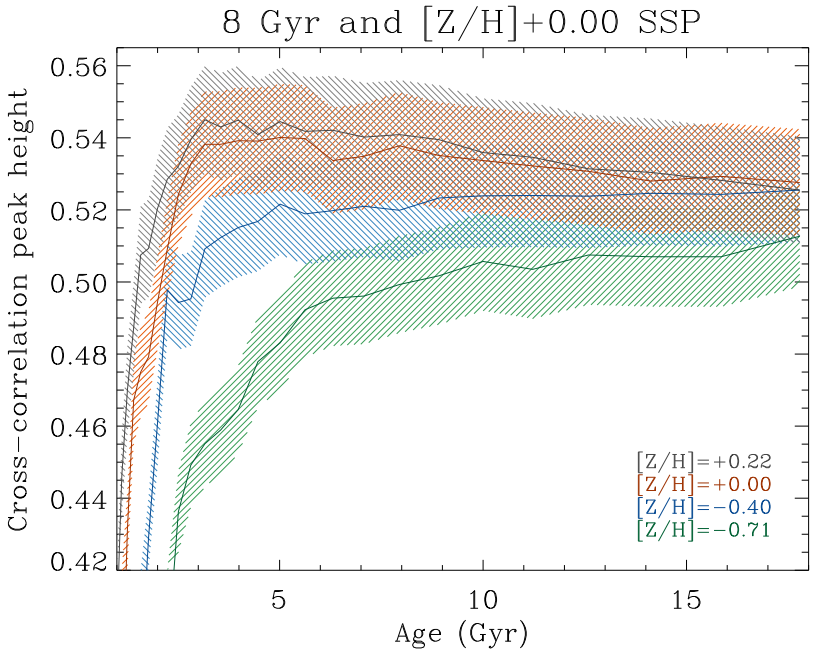

FIGURE 6.6— Same as Figure 6.4 for an SSP of 8 Gyr and solar metallicity from the Vazdekis et al. (2010) model library, once modified to match the spectral resolution, range, dispersion and S/N ratio of the data for the outer bar of NGC 357.

smoothed to mimic the observed spectrum for the outer bar. We also added gaussian noise to the model to match the S/N ratio of the data. The error regions are so large that, for ages above ∼3 Gyr the results for the solar and supersolar metallicity are completely mixed, which prevents us from providing a more constrained solution for the outer bar through the cross-correlation analysis. We have to note that the results obtained here are aimed to be complementary to those from the line-strength analysis. Therefore, we restrict the application of the cross-correlation to the bulge and inner bar.

6.2.4 A non-outstanding bulge

Figures 6.7 and 6.8 show the analysis of the line-strength indices of the bulge of NGC 357. Four age indicators are plotted against several well selected metallicity indicators and the *G*-band, using features from both the red and blue spectral ranges available for this component. Balmer lines might be affected by emission line contamination, although the amplitude of this emission decays

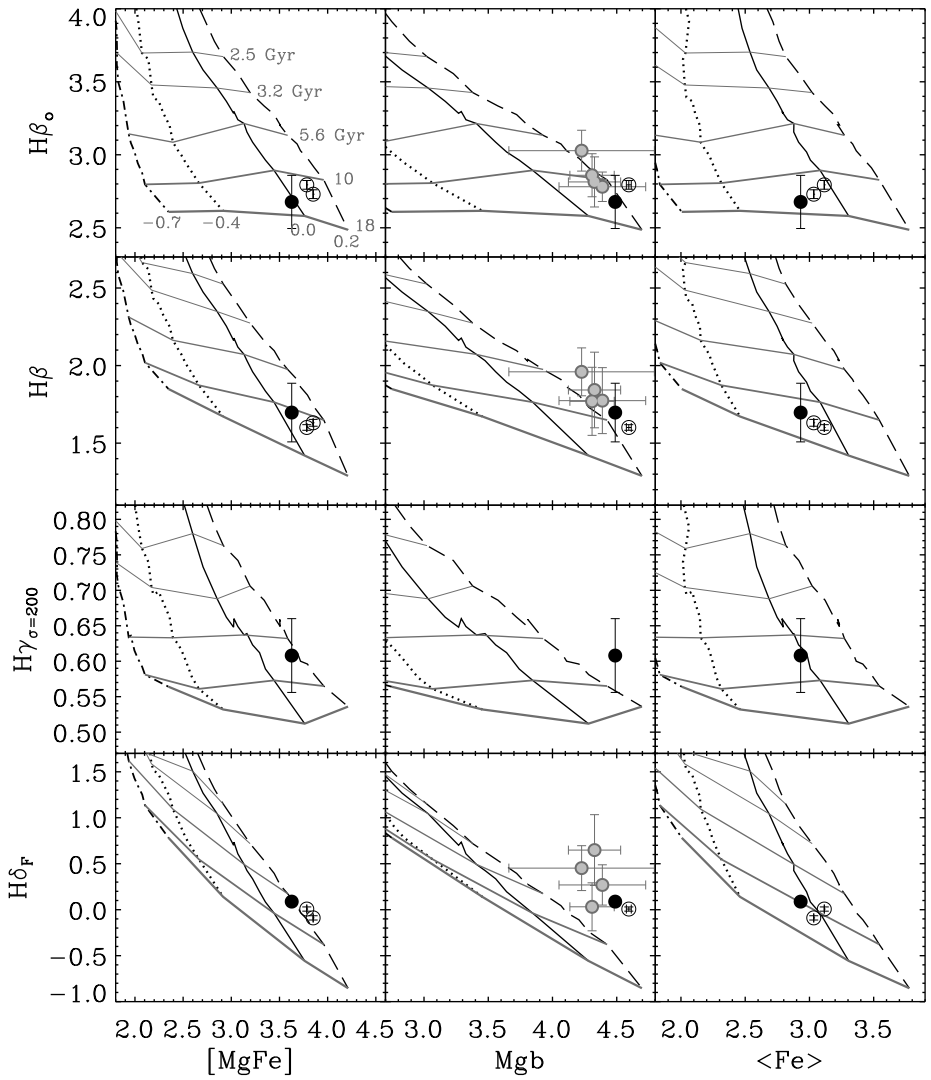

FIGURE 6.7— Age indicators Hβ_o, Hβ, H$\gamma_{\sigma=200}$, and Hδ_F (from top to bottom) versus the metallicity indicators [MgFe], Mgb, and $\langle$Fe$\rangle$ (from left to right). The grids correspond to the SSP models of Vazdekis et al. (2010) once smoothed to match the resolution of the data (σ ∼180 km s^{-1}). The lines represent different ages and metallicities increasing from top to bottom and from left to right, respectively. Ages and metallicities for the grids are indicated in the first panel. The black filled circle is the measurement for the bulge of NGC 357, whereas the grey filled circles are the mean values for the bulges of a subsample of barred galaxies from Pérez et al. (2009) and Pérez & Sánchez-Blázquez (2011). The open circles correspond to two elliptical galaxies in Virgo cluster from Yamada et al. (2006). All the reference galaxies have been selected to have a central velocity dispersion similar to that of NGC 357 (σ ∼180 km s^{-1}).

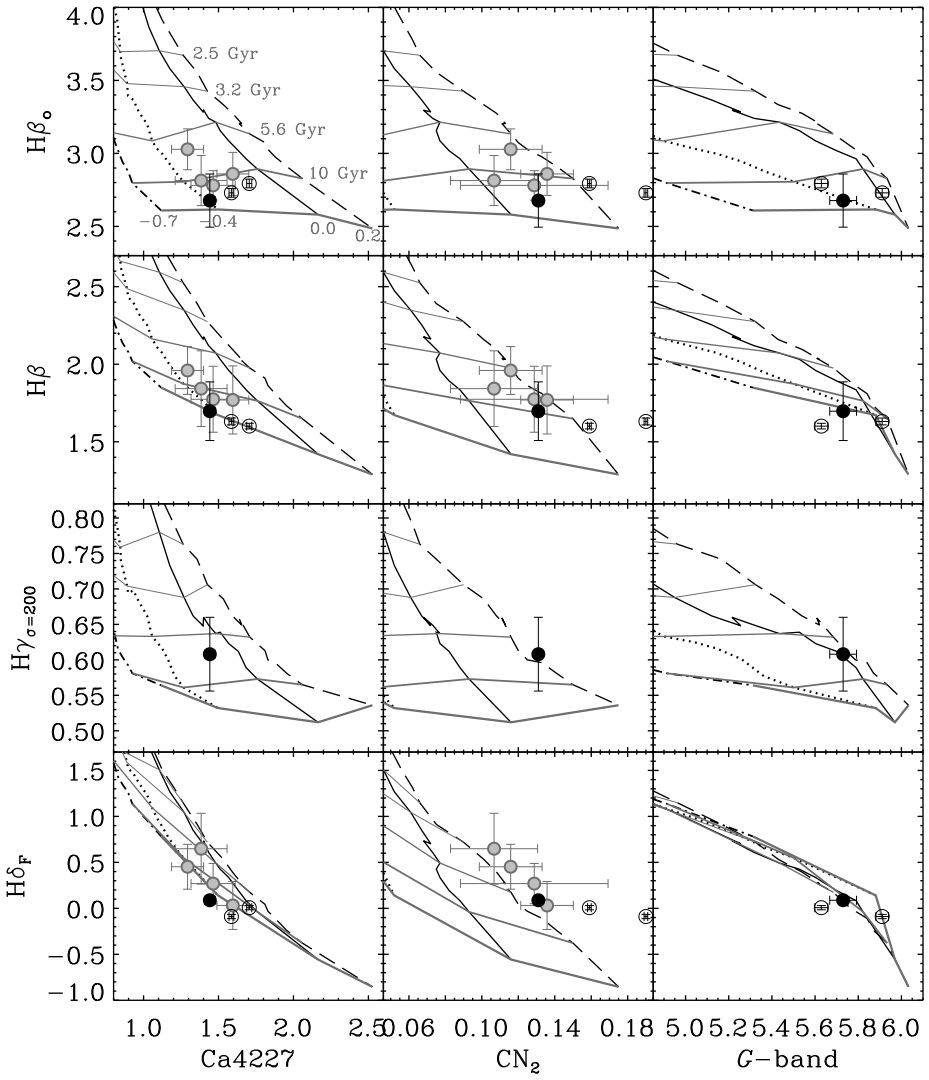

FIGURE 6.8— Same as Figure 6.7 but for the age indicators Hβ_o, Hβ, H$\gamma_{\sigma=200}$, and Hδ_F (from top to bottom) versus the metallicity indicators CN_2, and Ca 4227, and the G-band (from left to right).

from the top (Hβ_o and Hβ) to bottom (Hδ_F) indices of Figures 6.7 and 6.8. In fact, we find no emission in the Hδ feature for the bulge. For Hβ_o and Hβ, where the emission contamination is larger, we find some disagreements in the resulting ages with respect to those derived from Hγ and Hδ. Although the emission correction has been performed very carefully (see Section 6.2.1), these inconsistencies are probably due to an underestimate of the emission affecting the Hβ feature within the noise level. As an attempt to take this effect into account, the Hβ and Hβ_o error bars are obtained by computing the maximum and minimum (but not zero) 1-σ emission correction.

Moreover, we find subtle differences between the ages obtained with the Hβ_o and Hβ indices. These differences might be attributed either to the emission correction, which affects the two definitions differently, or to the greater sensitivity of Hβ_o to the α-enhancement in comparison to that of Hβ (Cervantes & Vazdekis, 2009). Indeed, these differences are more evident in the α-enhanced indicators (Mgb and CN_2), whereas the results from $\langle$Fe$\rangle$ or Ca 4227 are almost identical. Taking into account the error bars and the results from all the plots in Figures 6.7 and 6.8, we derive a mean luminosity-weighted age of $\sim$8 Gyr for the bulge of NGC 357.

From the first column in Figure 6.7, where the total metallicity indicator [MgFe] is plotted, we derive a supersolar metallicity $\sim$0.2 dex for the bulge of NGC 357. For this component we also measure the $\langle$Fe$\rangle$, Mgb, and CN_2 indices, so that it is possible to estimate the [$Z_{Mgb}/Z_{\langle Fe\rangle}$] and [$Z_{CN_2}/Z_{\langle Fe\rangle}$] ratios, which are calculated as the relative metallicity difference obtained when plotting the various metallicity indicators versus the Mg (Vazdekis et al., 2001). [$Z_{Mgb}/Z_{\langle Fe\rangle}$] and [$Z_{CN_2}/Z_{\langle Fe\rangle}$] are shown to be good proxies for the [Mg/Fe] and [CN/Fe] abundance ratios. In fact, [$Z_{Mgb}/Z_{\langle Fe\rangle}$] and [Mg/Fe] follow a linear relation, as shown in Vazdekis et al. (2010). These overabundances are important because they can be used to constrain the timescale for the formation of the bulk of their stellar populations: as introduced in Chapter 5, Mg (as well as other α elements) is the product of type II supernovae, which explode soon after the star formation; on the contrary, the Iron-peak elements are ejected by type Ia supernovae, on longer timescales of around 1 Gyr. In the meantime between those two cases, the low- and intermediate-mass stars enrich the interstellar medium with C and N. Therefore, the [$Z_{Mgb}/Z_{\langle Fe\rangle}$] and [$Z_{CN_2}/Z_{\langle Fe\rangle}$] values might help to put constraints on the assembly history of a galaxy. In the case of NGC 357, we find [$Z_{Mgb}/Z_{\langle Fe\rangle}$]=0.3-0.4 dex, which is the value expected for an E/S0 galaxy of σ $\sim$180 km s^{-1} according to the well-known correlation between [$Z_{Mgb}/Z_{\langle Fe\rangle}$] and σ for early-type objects (e.g., Jørgensen, 1999; Trager et al., 2000; Kuntschner, 2000; Vazdekis et al., 2004; Carretero et al., 2004). Note that an extrapolation of the grid is necessary to estimate the [Mg/H]

abundance, since the models do not extend beyond [Z/H]=0.2 dex. We also find a supersolar $[Z_{CN_2}/Z_{\langle Fe\rangle}]$ ratio for the bulge of NGC 357, that reaches $\sim$0.2 dex.

The bulge of NGC 357 shows subsolar values for the Ca 4227 index. This is the expected behaviour for galaxies of similar central velocity dispersion. In fact, rather than resembling other α elements such as the Mg, Ca tends to exhibit subsolar values (Vazdekis et al., 1997).

In order to find out if the formation of the bulge of NGC 357 has followed a process which is different due to the presence of the inner bar, we compare our results with those obtained for various elliptical galaxies and other spiral bulges. Thus, we have overplotted the index values for two Virgo ellipticals with a central $\sigma \sim$180 km s^{-1}, taken from the sample of Yamada et al. (2006). These measurements appear as two open circles in Figures 6.7 and 6.8. Moreover, we have selected a subsample of four early-type barred galaxies from the works by Pérez et al. (2007, 2009) and Pérez & Sánchez-Blázquez (2011) with central velocity dispersions similar to that of NGC 357. Two galaxies host a single bar (NGC 1169 and NGC 1358), and two are double-barred systems (NGC 2859, also included in our SAURON double-barred sample, and NGC 2962). For these objects, we have measured the mean line-strength indices inside the bulge region from the values at a resolution of $\sigma \sim$180 km s^{-1}. The results, when possible, are also shown in Figures 6.7 and 6.8 as grey filled circles. In general, the age, metallicity and α-enhancement obtained for NGC 357 resemble very closely those of the comparison bulges. The age and metallicity of the Virgo ellipticals are also in agreement with NGC 357, although they show a larger $[Z_{CN_2}/Z_{\langle Fe\rangle}]$ enhancement, with a mean value above $\sim$0.3 dex.

The results for NGC 357 from the line-strength analysis are also verified by the cross-correlation method. Figure 6.4 shows the peak heights resulting from cross-correlating the bulge spectra with SSPs of different ages and metallicities, following the methodology described in Section 6.2.3. From both spectral ranges, we obtain a supersolar value ([Z/H]$\sim$0.2 dex) for the mean luminosity-weighted metallicity, and a final age of 7-8 Gyr (although the error regions span a wider range). So far, the cross-correlation method alone is not able to clearly distinguish a mean luminosity-weighted stellar population above $\sim$5 Gyr, due to the flattening of the cross-correlation peak heights versus age profiles and the amplitude of the error bars. For smaller ages, Figure 6.4 shows that the curves are steeper, allowing us to disentangle different populations very efficiently. However, the fact that the results obtained from this procedure agree with the line-strength analysis, points to the potential power of this method. Note that the age-metallicity degeneracy is evident in Figure 6.4: the shoulder

of each metallicity curve (i.e., the point where there is a clear transition in the slope) occurs at older ages for lower metallicities.

6.2.5 Inner and outer bars: the general picture gets complicated

The relative ages and metallicities between bulge, inner bar and outer bar of NGC 357 are shown in Figure 6.9, where the age indicators Hγ_σ and Hδ_F are plotted against various metallicity indicators (including the new Fe4383^{SR} definition) and the *G*-band. In this case we are limited to indices in the blue range, since it is the only spectral range available for the two bars.

In the first panel of Figure 6.9 we plot Hγ_σ against Fe4383^{SR}, which provide the most orthogonal grid thanks to the age-disentangling power of Hγ_σ. We find that the bulge and inner bar show approximately the same mean luminosity-weighted age ($\sim$8 Gyr) and solar metallicity. The outer bar also presents a similar age as the inner structures, but it tends to be less metal-rich with [Fe/H]$\sim$-0.4 dex. However, the error bars are large due to the S/N requirements of the Hγ_σ index. For this reason it is necessary to complement these results with those from the less orthogonal Hδ_F versus Fe4383^{SR} grid, which confirms the previous estimates for the bulge and inner bar. The trend towards lower metallicites for the outer bar is also verified. In fact, the only difference we find between the two plots is that the outer bar seems to be slightly older when looking at the Hδ_F versus Fe4383^{SR} grid. However, taking into account the error bars and the results from the rest of the plots (particularly Hδ_F versus CN_2 and Hγ_σ versus Ca 4227), we must conclude that the three structural components of NGC 357 are nearly coeval.

Since we have measurements for the Fe4383^{SR} and CN_2 indices, we can use the [$Z_{CN_2}/Z_{Fe4383^{SR}}$] ratio as a proxy for the [CN/Fe] abundance, as we did in Section 6.2.4 with [$Z_{CN_2}/Z_{\langle Fe\rangle}$]. We find that, whereas the bulge and inner bar present an overabundance of [$Z_{CN_2}/Z_{Fe4383^{SR}}$]>0.2 dex, the outer bar has a more enhanced value above 0.4 dex.

To make a comparison with the age and metallicity of other main bars, we take into account the same galaxies we adopted as a reference in Figures 6.7 and 6.8. We compute the mean values of the line-strength indices along the main bar at a resolution of $\sigma \sim$180 km s^{-1} from the data of Pérez et al. (2009). These comparison values are shown in Figure 6.9 and the plotted errors take into account the variation of the line-strength indices along the main bar. As for the bulge, the outer bar of NGC 357 shows no particular features when compared to the other main bars. Indeed, its age and metallicity are within the ranges defined by the control sample.

We apply the cross-correlation method only to the inner bar spectrum since

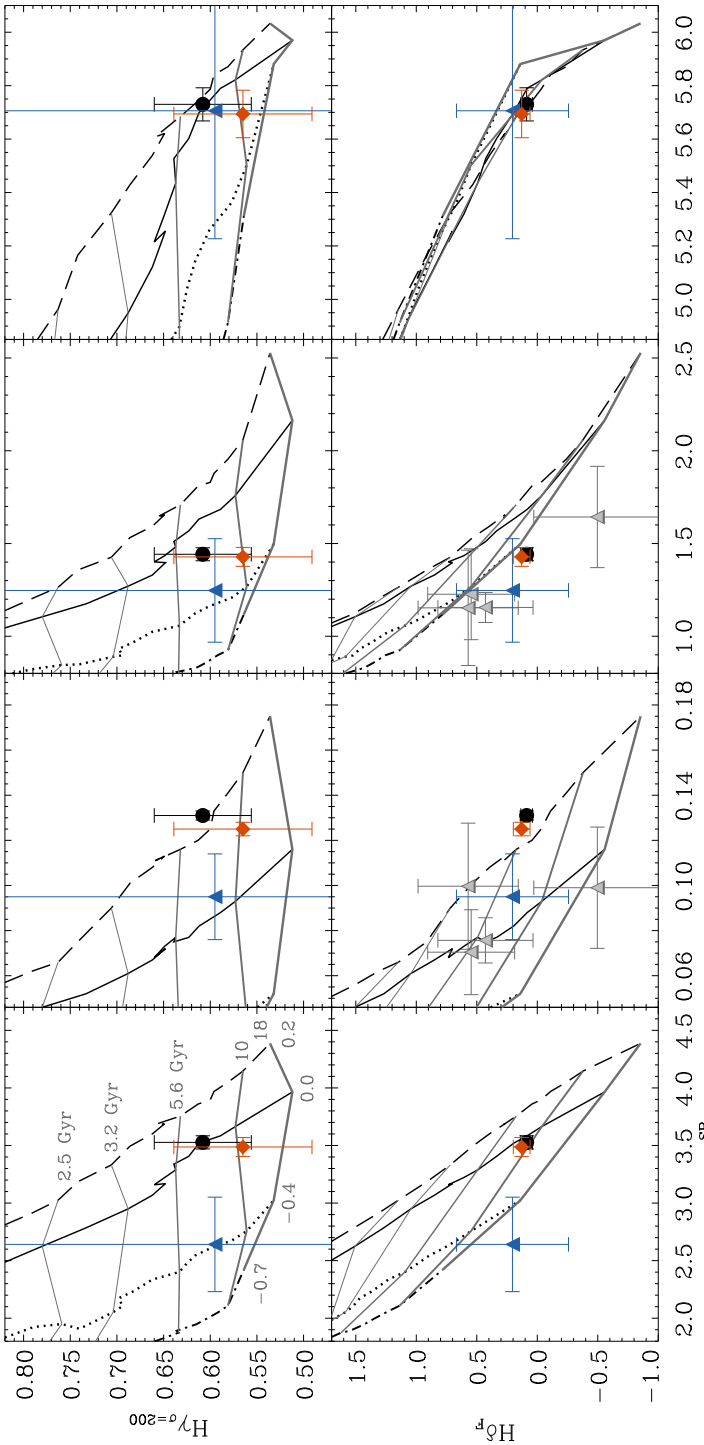

FIGURE 6.9— Age indicators $H\gamma_{\sigma=200}$ and $H\delta_F$ (top and bottom panels, respectively) versus the metallicity indicators $Fe4383^{SR}$, CN_2, and Ca 4227, and the G-band (from left to right). The model grids are the same as in Figures 6.7 and 6.8. The coloured symbols are the measurements for the different structural components of NGC 357: bulge (black circle), inner bar (orange diamond), and outer bar (blue triangle). The grey triangles are the mean values for the main bars of a subsample of galaxies from Pérez et al. (2009), selected to have a similar central velocity dispersion than NGC 357 ($\sigma \sim 180$ km s^{-1}).

that of the outer bar has too low a S/N ratio. The mean luminosity-weighted age and metallicity are consistent with those derived from the analysis of the line-strength indices. Figure 6.5 shows that although the maximum of the cross-correlation peak heights is obtained for ∼4.5 Gyr, the solution spans a wider range (from about 4 to 10 Gyr) when taking into account the error regions. The resulting metallicity, despite the partial overlapping between the solar and supersolar curves, is [Z/H]∼0.2 dex.

6.3 Putting the evidence together

The various pieces of evidence provided by the analysis performed on this galaxy lead to two main questions: what is the real structure of NGC 357, and how has this galaxy been formed? The study of the photometry (presented in Chapter 3) and kinematic constrains the structural composition of NGC 357, which reveals itself as a really complex galaxy. On the other hand, the analysis of the stellar populations provides surprisingly homogeneous results and sheds light on the most probable assembly process for our galaxy.

6.3.1 Shaping NGC 357: a disc, two bars, and...

Photometric studies have confirmed that NGC 357 is composed of, at least, four structures, namely bulge, inner bar, outer bar and disc (Erwin, 2004; Aguerri et al., 2005). The presence of the inner bar is also supported by the photometric and kinematical analysis performed in this thesis. In fact, the ellipticity and PA profiles presented in Figure 3.2 in Chapter 3, and the velocity and velocity dispersion profiles along the inner bar direction presented in Figure 6.1, show clear signatures of this small, secondary bar.

Interestingly, the analysis of the kinematics also shows evidence of an additional, inner component: a kinematically decoupled structure appears at the centre of NGC 357, rotating faster than its surroundings. This decoupling spans approximately ±2 arcsec and matches in size the observed central σ-drop. The different structures that shape NGC 357 have to account for all the signatures present in the kinematical profiles. In this Section we state the two possibilities that match the results obtained in this work.

... an inner disc and a classical bulge

The presence of a central velocity dispersion minimum in a spiral galaxy was first reported by Bottema (1989). Since then, the number of galaxies showing a σ-drop has increased significantly (see Section 1.4.3 in Chapter 1). The most accepted explanation for the formation of σ-drops in disc galaxies is the star

formation at their central regions: the new stars acquire the kinematical properties of the gas they are formed from; the dissipative nature of that gas is more efficient in the central regions because of the higher density and converts the gas into a cold stellar component, normally an inner disc, with a lower velocity dispersion than the surroundings. This scenario is in agreement with the N-body simulations of Wozniak et al. (2003) and Wozniak & Champavert (2006), who made use of bars to transport gas to the central regions.

NGC 357 seems to support this hypothesis since the central decoupling in velocity might be due to an inner disc whose low velocity dispersion would be the cause of the σ-drop. Therefore, NGC 357 is composed of at least five structures: bulge, inner disc, inner bar, outer bar and disc.

The σ-drop means a local minimum in the velocity dispersion with respect to the corresponding value for the bulge, which reaches $\sigma \sim$180 km s^{-1} or higher (the velocity dispersion profile should peak at the centre, where the σ-drop masks the velocity dispersion of the bulge). This high velocity dispersion value for the bulge implies it is pressure supported and classical. This result is supported by the work of Aguerri et al. (2005), who find that the bulge of NGC 357 lies in the same fundamental plane as the ellipticals or classical bulges of other early-type objects.

Within this context, the appearance of the σ-hollows at the edges of the inner bar in the velocity dispersion profile is also well understood, following the discussion presented in Chapter 4. By means of N-body simulations, we tested the possible scenarios that might give rise to these hollows, showing that their size and amplitude depend on two parameters: the relative contribution of the flux of the bulge to the total luminosity and the difference in the velocity dispersion of the two components. Therefore, a galaxy hosting a classical bulge with a high velocity dispersion and a colder, inner bar which dominates the total luminosity at its ends (where the light profile of the bulge has already decayed) will clearly show the two σ-hollows at the bar ends, as does NGC 357. In this scenario, the bulge is the hottest structural component of NGC 357 and the velocity dispersion decreases for the outer structures. Table 6.2 indicate the velocity dispersion values for each component. It is important to note that the true velocity dispersion of the inner disc is probably lower than the value given in Table 6.2, since the measured value includes the contribution of the bulge within the inner disc region.

There are two important drawbacks to this possible structural composition of NGC 357. First, the $a_4 > 0$ signature of the inner disc should be detected in the photometric analysis presented in Chapter 3. This is detected for the nuclear stellar discs observed in the centre of ellipticals and bulges (Morelli et al., 2010, and references therein). A careful inspection to the inner $\pm$2 arcsec

TABLE 6.2— Characteristic velocity dispersion values for the different structural components of NGC 357 within the context of the two possible scenarios. For the bulge and pseudobulge, these values represent their maximum velocity dispersion. For the outer bar and disc, the mean velocity dispersion values within the corresponding regions included in Figure 6.1 are provided.

	Scenario	(Pseudo)bulge	Inner disc	Inner bar	Outer bar	Disc
σ	(1)	$\geq$180	$\sim$170	$\sim$165	$\sim$145	$\sim$105
(km s^{-1})	(2)	$\sim$170	-	$\sim$180	$\sim$145	$\sim$105

(1) Classical bulge + inner disc + inner bar + outer bar + disc;
(2) Pseudobulge + inner bar + outer bar + disc.

in Figure 3.2 in Chapter 3 shows no evidence of discy isophotes. Second, the formation of the inner disc is usually related to recent star formation in the centre, but the analysis of the stellar populations for NGC 357 shows large ages for the central components; a significant young population such as that of an inner disc should be noticed when studying the mean luminosity-weighted age, even if it is mixed with an older, more massive component. Therefore, although this hypothesis seems promising, it does not explain all the properties found in this work.

... a pseudobulge

The second possibility for the structure of NGC 357 is that there is no inner disc. If this is the case, the central kinematical decoupling and the σ-drop have to be caused by the bulge itself, which therefore shows disc-like properties that indicate it is a pseudobulge rather than a classical one. This hypothesis is strongly supported by the Sérsic index (Sérsic, 1968) measured for the bulge of NGC 357 by Aguerri et al. (2005). They performed a photometric decomposition of an I-band image and obtained n=1.40$\pm$0.08, which is compatible with a pseudobulge. Indeed, Fisher & Drory (2008) study a sample of 77 galaxies and find that $\sim$90% of pseudobulges have n<2, whereas classical bulges have n>2.

Within this new context, the σ-drop is not actually a drop with respect to the higher velocity dispersion of the bulge, but the maximum velocity dispersion of the pseudobulge itself. Of course, the pseudobulge presents not so high a velocity dispersion, since it is rotationally supported, and therefore it can be colder than the inner bar. In this case, the two peaks of the velocity dispersion values at either sides of the centre have to be understood as signatures of the relatively hotter inner bar where this component dominates the total luminosity.

The σ-hollows appear where the bar ends and the light of the pseudobulge is the main contribution to the total flux. The surrounding structure, i.e., the outer bar, is also hotter than the outer parts of the pseudobulge and for that reason the velocity dispersion values increase again beyond the σ-hollows. The characteristic velocity dispersions for each structure are indicated in Table 6.2. This scenario is completely different from that proposed for the SAURON galaxies in Chapter 4. However, a basic conclusion about the origin of the σ-hollows remains as it is attributed to the contrast of velocity dispersions between components.

This hypothesis also explains the results from the analysis of the morphology of NGC 357: the ellipticity profile acquires approximately the same value at either sides of the peak due to the inner bar, suggesting that the centre and the surrounding regions are dominated by the same structure. Concerning the dynamical support of the bulge, we estimate $V_{\rm max}/\sigma$ $\sim$0.23 and ϵ<0.1 in the bulge region; therefore, the bulge is consistent with an oblate spheroid flattened by rotation (see Figure 1.4 in Chapter 1; Kormendy & Kennicutt, 2004). Nevertheless, the interpretation of the $V_{\rm max}/\sigma - \epsilon$ relation has to be carried out carefully, since a complex kinematical structure of the galaxy might lead to misleading results, as it is shown in Emsellem et al. (2011).

6.3.2 Formation of NGC 357

The analysis of the stellar populations of NGC 357 is focused on three single regions: bulge, inner bar and outer bar. The striking result obtained in this work is that the bulge and inner bar show very similar stellar population properties, indicating that they were formed in the same process or, at least, from the same source of stars. Moreover, the outer bar is also nearly coeval to the inner structures, although it presents a lower metallicity and a larger α-enhancement. This result points towards a faster assembly of the outer bar with respect to the bulge and inner bar. Finally, we compare the bulge and outer bar of NGC 357 with other bulges and main bars of single- and double-barred galaxies with similar central σ values (Pérez et al., 2009; Pérez & Sánchez-Blázquez, 2011), finding no significant differences among them.

The results obtained here for NGC 357 indicate that theories claiming that inner bars play a major role in secular evolution might not be suitable for this galaxy. If inner bars were the key to the transport of gas to the central regions and trigger star formation there, a gradient in age and metallicity from outer to inner structures would be expected, presenting a younger population in the galaxy centre. Although our galaxy has gas content and probably some star formation is taking place in it, the stellar population analysis indicates that this is not the main mechanism driving the evolution of NGC 357. Therefore,

these results lead to the question on how the structure of NGC 357 formed.

Numerical simulations have predicted different scenarios for the formation of nested bars systems, most of them requiring the presence of a dissipative component that is dynamically disturbed and generates the secondary bar (e.g., Friedli & Martinet, 1993; Heller et al., 2001; Shlosman & Heller, 2002; Englmaier & Shlosman, 2004). Within this scenario, the inner bar should be younger than the outer bar. However, the two bars of NGC 357 have similar population properties, so they were formed at the same time or, most likely, the existing stars from the outer bar or the disc redistributed and shaped the inner structures. Therefore, only those numerical works that do not need gas to generate the double-barred objects seem to be compatible with the observational evidences shown here for NGC 357. This is the case of the N-body simulations by Debattista & Shen (2007), who use a disc and a rapidly rotating bulge (such as a pseudobulge) to create a double-barred system. In these simulations, the inner bar appears first, but this is probably a consequence of the initial presence of the pseudobulge: in the real Universe, the outer bar most likely is formed first, so the pseudobulge would be generated from the gas flow along it. This scenario reinforces the hypothesis of the pseudobulge for the case of NGC 357, since the bulge rotation is an essential condition for generating the two bars within the Debattista & Shen (2007) gas-free framework.

There is one possibility to reconcile the classical secular approach with the observational results for NGC 357, and this is to assume a very fast formation of the central components: immediately after the outer bar was created, the gas flowed along it, triggered a quick star formation and formed the inner bar and the bulge. Within this scenario, the final ages of the three components would be very similar. The outer bar would be slightly older, but this is consistent with our results taking into account the error bars. In this scenario a positive metallicity gradient for the gas along the outer bar is required. Although this might be somewhat striking, from a stellar (not gaseous) point of view there is evidence for such gradients. Indeed, Pérez et al. (2009) study a sample of 20 barred galaxies and find that some of them tend to become more metal-rich at the ends of the main bars. Moreover, those objects have greater mean ages and higher central velocity dispersions than the rest of the sample, which is in agreement with the properties found for NGC 357. Unfortunately, the S/N ratio of our data is not enough to measure gradients along the main bar to check this possibility.

7

The new pieces of the puzzle: conclusions

... decedente, pax.

Double-barred galaxies are intriguing objects. Diverse hypothesis, backed by the results of a variety of numerical simulations, are suggested to explain them, and the astrophysical community is divided into those who consider double bars as the key systems responsible for the secular evolution of a major fraction of spirals, and those who simply think that inner bars are just another structure in the inner regions of galaxies without further implications for their hosts. The present thesis is conditioned by the interesting and often elegant scenarios implied by the former assumptions, but we have kept a critical posture so our main goal has been to constrain the actual role of inner bars in the evolution of galaxies. Therefore, we have carried out the first kinematical and stellar population analysis of a sample of five double-barred galaxies ever performed, thus accomplishing the goals proposed in Chapter 1 and finding two outstanding results:

- Contrary to previous claims, **stellar inner bars do affect the velocity dispersion distributions of their host galaxies, as they are responsible for the appearance of the so-called σ-hollows**. Never observed before, these stellar σ-hollows are the only known kinematical indicator of the presence of inner bars.

- **Inner bars are younger and more metal-rich than their surroundings** (i.e., the outer bar).

Apart from the two main observational evidences summarised above, this thesis provides other unique and very interesting results on the structure, kinematics, stellar populations, and formation and evolution of double-barred galaxies. All the contributions, both results and conclusions, are compiled in the following items:

- Double-barred galaxies present a great variety of stellar and gaseous kinematical structures in the central regions. Kinematically decoupled inner discs, counter-rotating gas, and spiral gas structures have been found in the inner parts of the sample. In particular, four out of the five galaxies show any evidence of the presence of a disc-like component in their centres, either σ-drops or kinematically decoupled discs revealed by the expected v-h_3 anticorrelation. None of these structures is backed by a counterpart in the stellar population analysis.

- Inner bars have a very slight influence on the LOS velocity distribution of the stellar component of double-barred galaxies. A velocity profile along the inner bar direction such as the one performed in the analysis of the `EMMI` data reveals the *double-hump* profile characteristic of barred structures, but its effect is so subtle that it is not evident from the corresponding `SAURON` spatial distributions.

- The origin of the σ-hollows is probably related to the contrast between the different velocity dispersion values of the inner bar and either the classical bulge (with higher velocity dispersion than the inner bar) or disc-like bulge (with lower velocity dispersion than the inner bar). σ-hollows are present only at the bar ends, where the low velocity dispersion structure is dominating the total flux. Within this framework, the amplitude and size of the σ-hollows would depend on the difference in velocity dispersion and the relative sizes and luminosity profiles of the two structural components involved. The nature of the σ-hollows is completely different from that of the σ-drops, and both features may coexist in the same galaxy, as in the case of NGC 357.

- Possible evidence of gas inflow through the inner bars towards the very central regions have shown up in the gas intensity and velocity distributions of the four double-barred galaxies observed with `SAURON`.

- NGC 357 is probably hosting a disc-like or pseudobulge, apart from the rest of structural components of a double-barred galaxy, namely inner bar, outer bar, and disc. The other four double-barred galaxies of the

sample, NGC 2859, NGC 3941, NGC 4725, and NGC 5850, are shaped by a classical bulge.

- Inner bars present ages around ∼7 Gyr so they are younger and more metal-rich than the outer bars. This result is clear for four out of the five galaxies observed (NGC 2859, NGC 3941, NGC 4725, and NGC 5850) and it is **compatible with a gas-rich formation scenario** in which inner bars are formed after the material has flowed along the main bars.

- Among the SAURON galaxies, NGC 2859, NGC 4725, and NGC 5850 present positive age and negative metallicity gradients along the inner and outer bars. NGC 3941 also shows the same gradients inside the inner bar region, whereas the profiles along the outer bar are almost flat. The [Mg/Fe] radial profiles are also rather flat with lower values at the very central parts, thus indicating a more time-extended star formation of these limited regions.

- The inner bar of NGC 357 is also more metal-rich than its outer bar, but the stellar population analysis indicate that both structures are almost coeval and with intermediate ages (∼8 Gyr, although the error bars are also compatible with an older main bar). Moreover, the main bar is more α-enhanced than the inner regions, indicating that it was assembled on shorter timescales. Hence, the formation of **NGC 357 has most likely followed a gas-free formation scenario**, so the inner bar is created by the redistribution of the existing disc stars, probably due to the presence of the central disc-like bulge.

- The five double-barred galaxies contain gas and probably some star formation is taking place in them. However, we find no evidences of relevant star-forming regions and the bulges or central components of the double-barred sample show no distinct stellar populations with respect to the inner bars. We therefore conclude that **these five inner bars are not playing a major role in the secular evolution of their host galaxies**.

8

Las nuevas piezas del puzle: conclusiones

Una isla es siempre interesante.
La preside el misterio de su formación y en ella la vida,
que emerge del mar o se fracciona de la tierra,
se concentra y se abre más lentamente,
pero con doble fuerza porque ha de vencer a su propia prisión.
José Manuel Guimerá
(Prólogo del libro "Estampas tinerfeñas", de Leoncio Rodríguez)

Las galaxias con dos barras son objetos fascinantes rodeados de una nube de hipótesis y teorías acerca de su estructura, formación y evolución. Tal es así que la comunidad astrofísica hoy en día se divide entre aquellos que consideran que las dobles barras son los sistemas clave en la evolución secular de las galaxias espirales y los que opinan que las barras internas no son sino otra estructura más en las regiones centrales de las galaxias, sin mayores implicaciones para sus anfitriones. Si bien la motivación de la presente tesis encuentra su origen en los interesantes escenarios propuestos por ese primer grupo de investigadores, la objetividad y mente crítica han sido una constante del trabajo aquí presentado, de modo que nuestro principal objetivo ha sido determinar el papel real que las barras internas juegan en la evolución de las galaxias. Para ello hemos llevado a cabo el primer análisis detallado jamás realizado de la cinemática y las poblaciones estelares de una muestra de cinco galaxias con dos barras; de esta forma hemos podido cumplir con los objetivos propuestos en el Capítulo 1, consiguiendo además dos resultados principales:

- **Las barras internas afectan a la distribución de dispersión de velocidades de sus galaxias anfitrionas, pues son responsables de la aparición de los llamados *σ-hollows*.** La presencia de estos *σ-hollows*, nunca antes observados, contradice las conclusiones obtenidas anteriormente para galaxias con dos barras. Además, los *σ-hollows* son las únicas señales cinemáticas conocidas de la presencia de barras internas.

- **Las barras internas son más jóvenes y metálicas que las estructuras circundantes** (barra externa, principalmente).

Además de estas dos evidencias observacionales destacadas, la presente tesis proporciona otros resultados únicos y muy interesantes acerca de la estructura, cinemática, poblaciones estelares, y formación y evolución de las galaxias con dos barras. Todas las contribuciones de este trabajo, desde los simples resultados hasta las conclusiones fruto de la discusión de diferentes hipótesis, se resumen a continuación:

- Las galaxias con dos barras presentan una gran variedad de estructuras cinemáticas, tanto estelares como gaseosas, en sus regiones centrales. Así, en nuestra muestra de galaxias hemos encontrado discos internos cinemáticamente desacoplados, gas contrarrotante con respecto a las estrellas y estructuras espirales de gas. En concreto, cuatro de las cinco galaxias muestran alguna evidencia de la presencia de una componente tipo disco en sus partes internas, bien en la forma de *σ-drops* o bien como discos desacoplados detectados a partir de la esperada anticorrelación entre la velocidad y el parámetro h_3. Ninguna de estas estructuras tiene contrapartida en el análisis de las poblaciones estelares.

- Las barras internas tienen una sutil influencia en la distribución de la velocidad de las galaxias con dos barras. Una curva de velocidad a lo largo de la dirección de la barra interna, como la elaborada en el análisis de los datos de `EMMI`, muestra el típico perfil con *doble joroba* característico de las estructuras con barra, pero su efecto es tan tenue que ni siquiera es evidente en los correspondientes mapas de velocidad elaborados a partir de los datos de `SAURON`.

- El origen de los *σ-hollows* está probablemente relacionado con el contraste entre los diferentes valores de la dispersión de velocidades de la barra interna y bien el bulbo clásico (con valores más altos de la dispersión de velocidades que la barra interna) o bien el bulbo tipo disco (con valores más bajos de la dispersión de velocidades que la barra interna). Los *σ-hollows* aparecen únicamente en los extremos de la barra, donde la

estructura con menor dispersión de velocidades domina el flujo total de la galaxia. En este contexto, la amplitud y el tamaño de los *σ-hollows* depende de la diferencia en dispersión de velocidades y en los tamaños y perfiles de luminosidad relativos de las dos componentes estructurales en juego. La naturaleza de estos *σ-hollows* es completamente diferente a la de los *σ-drops* y ambos pueden coexistir en la misma galaxia, como en el caso de NGC 357.

- Las distribuciones de intensidad y velocidad conrrespondientes al gas para las cuatro galaxias observadas con `SAURON` muestran posibles evidencias de flujo de gas hacia las zonas centrales.

- NGC 357 contiene probablemente un bulbo tipo disco además del resto de componentes estructurales de una galaxia con dos barras, a saber, barra interna, barra externa y disco. Las otras cuatro galaxias de la muestra, NGC 2859, NGC 3941, NGC 4725 y NGC 5850, tienen un bulbo clásico.

- Las barras internas muestran edades alrededor de 7 Gyr y son más jóvenes y metálicas que las barras externas. Este resultado es evidente para cuatro de las cinco galaxias observadas (NGC 2859, NGC 3941, NGC 4725 y NGC 5850) y es **compatible con un escenario de formación rico en gas** en el cual las barras internas son creadas a partir del material que fluye a lo largo de las barras externas hacia las zonas centrales.

- De las galaxias observadas con `SAURON`, NGC 2859, NGC 4725 y NGC 5850 presentan gradientes positivos de edad y negativos de metalicidad a lo largo de las barras interna y externa. NGC 3941 también muestra los mismos gradientes en la región de la barra interna, mientras que los perfiles son casi planos a lo largo de la barra externa. Los perfiles radiales de [Mg/Fe] son prácticamente planos con valores más bajos en las regiones centrales, que habrán sufrido por tanto una formación estelar más extendida en el tiempo.

- La barra interna de NGC 357 es más metálica que la barra externa, pero el análisis de poblaciones estelares indica que ambas estructuras son prácticamente coetáneas y con edades intermedias ($\sim$8 Gyr, aunque las barras de error son compatibles también con edades más viejas para la barra externa). Además, la barra externa presenta valores más altos de [Mg/Fe] que las regiones internas, indicando que fue constituída en escalas de tiempo inferiores. Así pues, **NGC 357 parece haber seguido un escenario de formación libre de gas**, de modo que la barra interna

es creada por la redistribución de las estrellas del disco ya existentes, probablemente gracias a la presencia del bulbo tipo disco central.

- Las cinco galaxias con dos barras contienen gas y por lo tanto es probable que tengan cierta actividad de formación estelar. Sin embargo, no encontramos evidencias de regiones con formación estelar relevante y las poblaciones estelares de los bulbos o las componentes centrales de la muestra son indistinguibles de las de las barras internas. Por lo tanto, hemos de concluir que **estas cinco barras internas no están desempeñando un papel importante en la evolución secular de sus galaxias anfitrionas**.

9

Still much to know. What comes next?

The most exciting phrase to hear in science,
the one that heralds the most discoveries,
is not "Eureka!" but "That's funny..."
Isaac Asimov

Motivating, striking, interesting, and promising, the several properties and conclusions achieved during this work prompt new questions about the structure, formation, and evolution of double-barred galaxies. Although we have advanced a step farther in elucidating the characterisation of these objects, there is still much to do, and the next actions are clear from the analysis performed during this thesis.

- **Gradients and outer regions.** In the present work we have been restricted to the central regions of double-barred galaxies (i.e., bulge, inner bar, and part of the outer bar), due to both S/N and FoV limitations. In fact, we have already analysed the age, metallicity, and abundance patterns around the inner bar region, but we are still lacking the corresponding results for the outer structures, which are essential to achieve a complete view of the formation of these objects. Integral-field and long-slit spectra provide complementary information and both are necessary to fully understand the outer regions of double-barred systems and check if particular features, such as the σ-hollows, appear also in the main bars.

  Despite the difficulty of obtaining such demanding observations, we already have at our disposal long-slit data of extremely high-quality for five

double-barred galaxies, some of them in common with the SAURON sample already analysed. These new spectra will allow us to recover the age, metallicity, and abundance gradients along the inner and outer bars, and even reach the transition region with the disc. Moreover, we will take advantage of the larger spectral range covered by these spectra with respect to the restricted SAURON wavelength range. We intend to measure a variety of abundance ratios, important because they put different constraints to the formation time-scales of the stellar populations.

- **SFHs.** Despite the high-quality of the data used in this work, we have been prevented from deriving the detailed SFHs of the double-barred sample mainly because of the restricted wavelength ranges of the SAURON and EMMI spectra. Although the mean-luminosity weighted age and metallicity distributions provide important constraints on the formation and evolution of these objects, SFHs studies are achieving relevance and robustness in astrophysical research and represent an obvious next step from the analysis presented here. We aim at deriving these SFHs with the long-slit data mentioned above, and at increasing the sample with additional long-slit and integral-field spectra fulfilling the requirements for the SFH analysis.

- **Statistical significance and comparison with singly barred and unbarred galaxies.** The detailed analysis of individual double-barred galaxies performed in this thesis is time-consuming, and the required high-quality data are not easily available. For these reasons, our study is limited to only five galaxies. In order to obtain statistical results and more robust conclusions, it is necessary to extend this analysis to a larger sample of double-barred systems and perform a comparison of the general conclusions with singly barred and unbarred galaxies. Specially useful for this purpose will be the role of several integral-field surveys now being designed or performed, such as *MaNGA* (*Ma*pping *N*earby *G*alaxies at *A*PO), a continuation of the Sloan Digital Sky Survey (SDSS) program planned for 2014, or *CALIFA* (*C*alar *A*lto *L*egacy *I*ntegral *F*ield *A*rea Survey; Sánchez et al., 2012), currently operative.

  The integral-field nature of the CALIFA survey and the wavelength range (3700 to 7000 Å) it provides are ideal for analysing the kinematics and stellar populations of barred galaxies. We intend to perform a search for inner barred structures in the CALIFA sample through the combination of two techniques explained in Chapter 1: the unsharp masking and the surface photometry decomposition. Once we have identified the potential double-barred objects, we will focus on the kinematical analysis in

order to check if σ-hollows are present in the velocity dispersion maps. We will then analyse the kinematic and stellar population properties of the final double-barred subsample and will compare the results with a well-selected subsample of single- and non-barred galaxies. Although the spatial resolution ($\sim$1 kpc) is a handicap for recovering structures inside the inner bar region, some of the results, such as the overall age distribution of the inner bar with respect to the outer bar, can be explored in the CALIFA data. CALIFA will also help to advance in our understanding of the ionised gas content in double-barred galaxies, a very atractive topic after the nice results obtained with `SAURON` in this thesis. For this latter purpose, it would be also interesting to exploit the advantages offered by other intruments specifically devoted to the analysis of the gas content, such as the Fabry-Perot `GHaFaS`, mounted on the WHT (La Palma, Spain).

- **The cosmological context.** The place of double-barred systems in the more general benchmark of the formation and evolution of the Universe will be provided by cosmological simulations which have to account for the observational results obtained during this work. In fact, astrophysical research requires the fusion of the knowledge and work of theoretical and observational groups in order to understand the behaviour of the Universe. A good example is the description and motivation of the *RAVET* (*R*eal *A*nd *V*irtual *E*arly-*T*ype Galaxies) project, which combines experience and research tools in complementary fields, such as stellar population synthesis and analysis, chemical evolution, cosmological simulations, and structural evolution of galaxies with cosmic time, from several Spanish groups and international collaborators. Unfortunately, the spatial resolution of these simulations in the central regions of galaxies is rather poor, but we can adapt our data to obtain integrated properties and compare them with cosmological results and go a step further in the understanding of the role of inner bars in the morphological transformation experimented by galaxies.

A

SAURON maps galaxy by galaxy

Lejos, lejos el mar, tras de los montes,
solo, quemándose en su azul parado
Rafael Alberti

In order to make easy the inspection of the results obtained in this thesis for each double-barred galaxy of the SAURON sample, and therefore allow the comparison of the different analysis (stellar and gas kinematics, and stellar populations) for the same object, this Appendix collects all the maps corresponding to each out of the four galaxies.

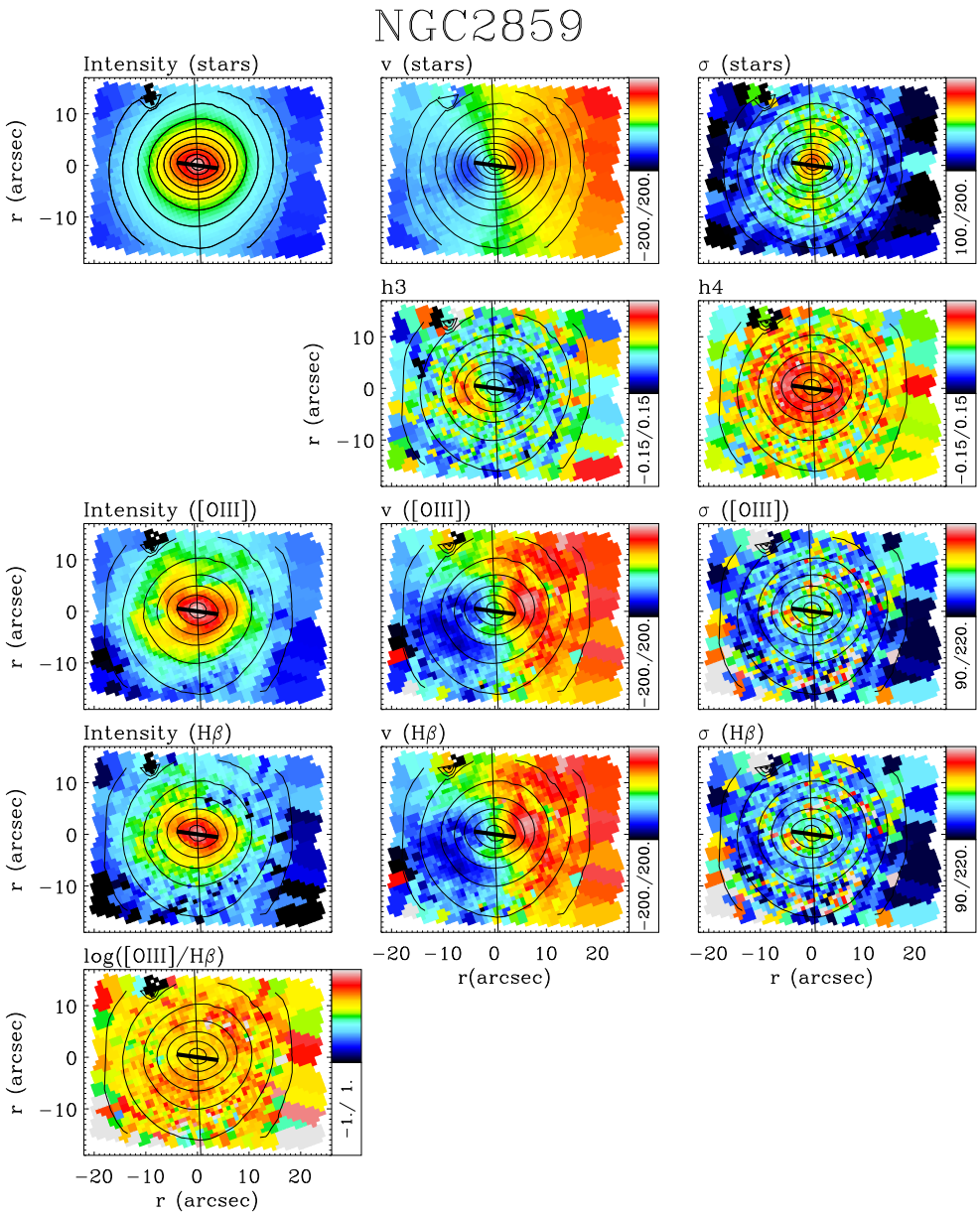

FIGURE A.1— Kinematical analysis of the double-barred galaxy NGC 2859. The two top rows contain the stellar kinematics; from left to right and from top to bottom: stellar intensity (in arbitrary units), LOS velocity ($\mathrm{km\,s^{-1}}$), velocity dispersion ($\mathrm{km\,s^{-1}}$), h_3, and h_4 maps. The third and four rows represent the gas kinematics derived from the [OIII] and Hβ emission lines, respectively; from left to right: line intensity (arbitrary units), velocity ($\mathrm{km\,s^{-1}}$), and velocity dispersion ($\mathrm{km\,s^{-1}}$). The bottom panel is the [OIII]/Hβ gas intensity ratio in logarithmic scale. For all the maps, we have overplotted the position angle and length of the inner bar (thick line), the position angle of the outer bar (thin line), and the contours of the reconstructed total intensity map. The scale is 1 arcsec $\sim$ 120 pc.

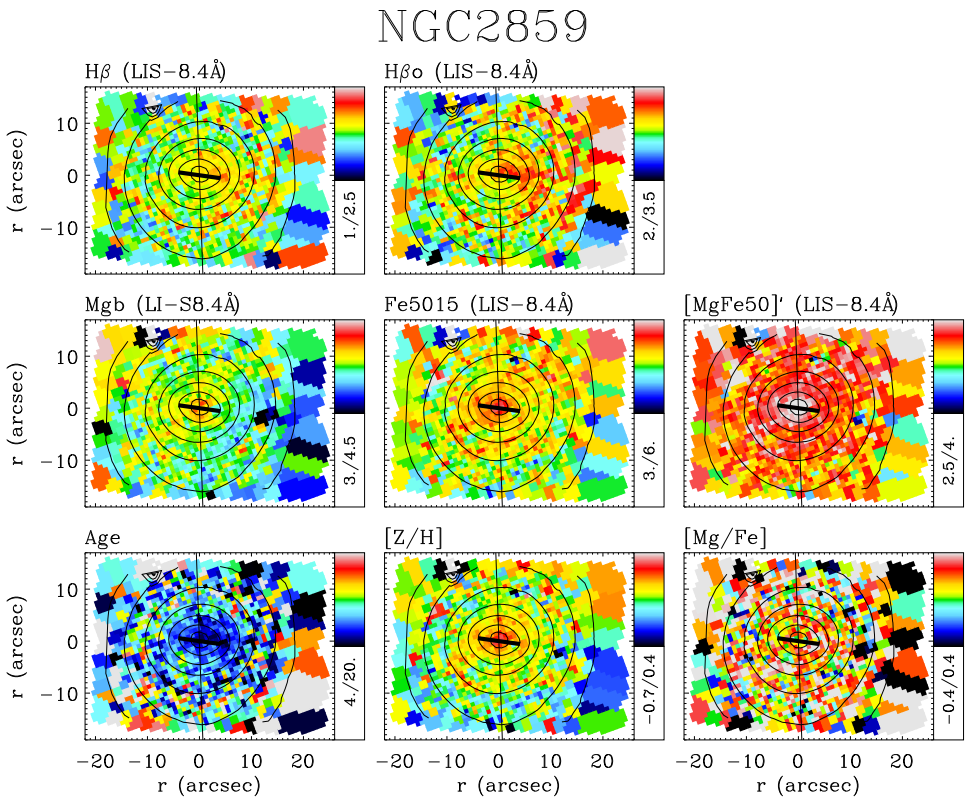

FIGURE A.2— Stellar population analysis for the double-barred galaxy NGC 2859. The first row include the maps of the age-sensitive indices Hβ and Hβ_o, whereas the middle row shows the maps corresponding to the metallicity indicators Mgb, Fe5015, and [MgFe50]$'$. All the indices are measured at a resolution of 8.4Å (FWHM), following the corresponding LIS system. The bottom row contains the age (in Gyr), metallicity, and α-enhancement distributions, from left to right, respectively. For all the maps, we have overplotted the position angle and length of the inner bar (thick line), the position angle of the outer bar (thin line), and the contours of the reconstructed total intensity map. The scale is 1 arcsec $\sim$ 120 pc.

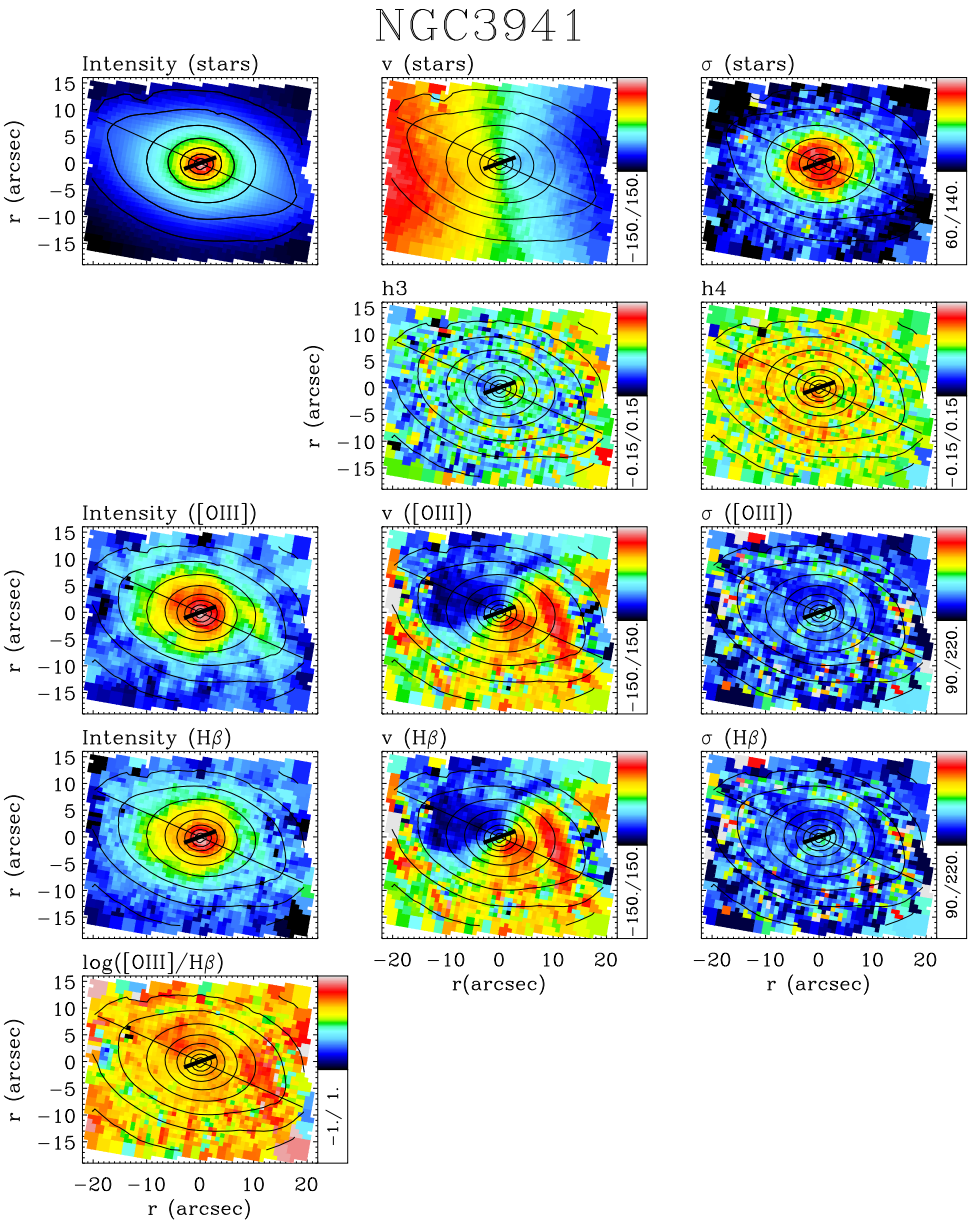

FIGURE A.3— Same as Figure A.1 but for NGC 3941. The scale is 1 arcsec ∼ 90 pc.

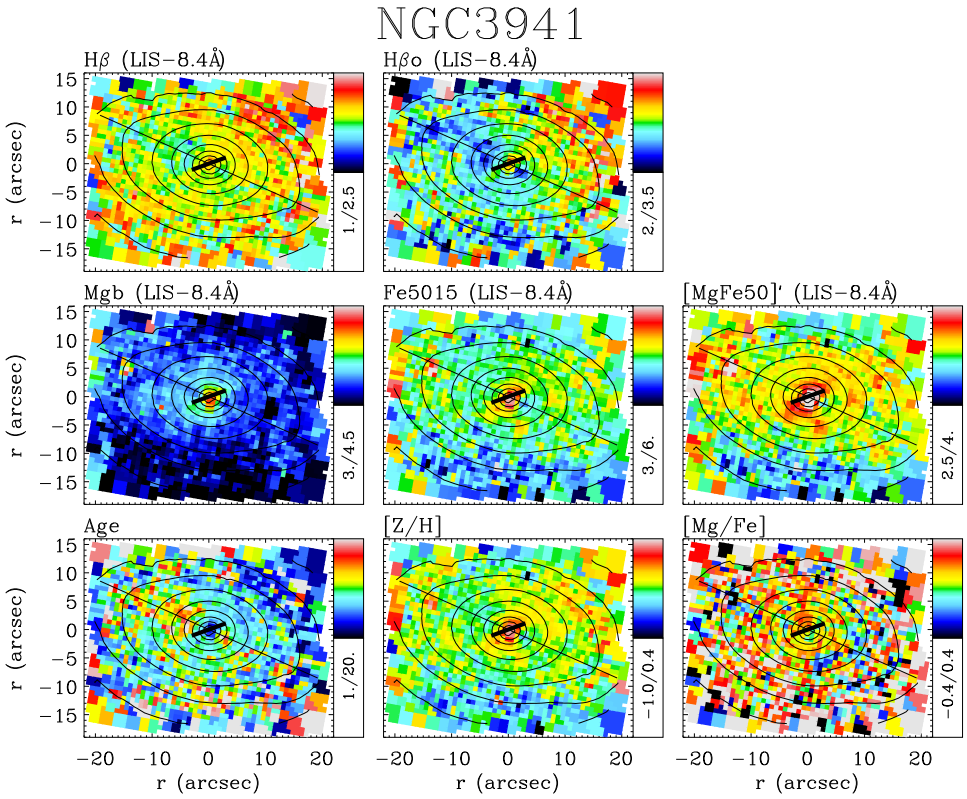

FIGURE A.4— Same as Figure A.2 but for NGC 3941. The scale is 1 arcsec ∼ 90 pc.

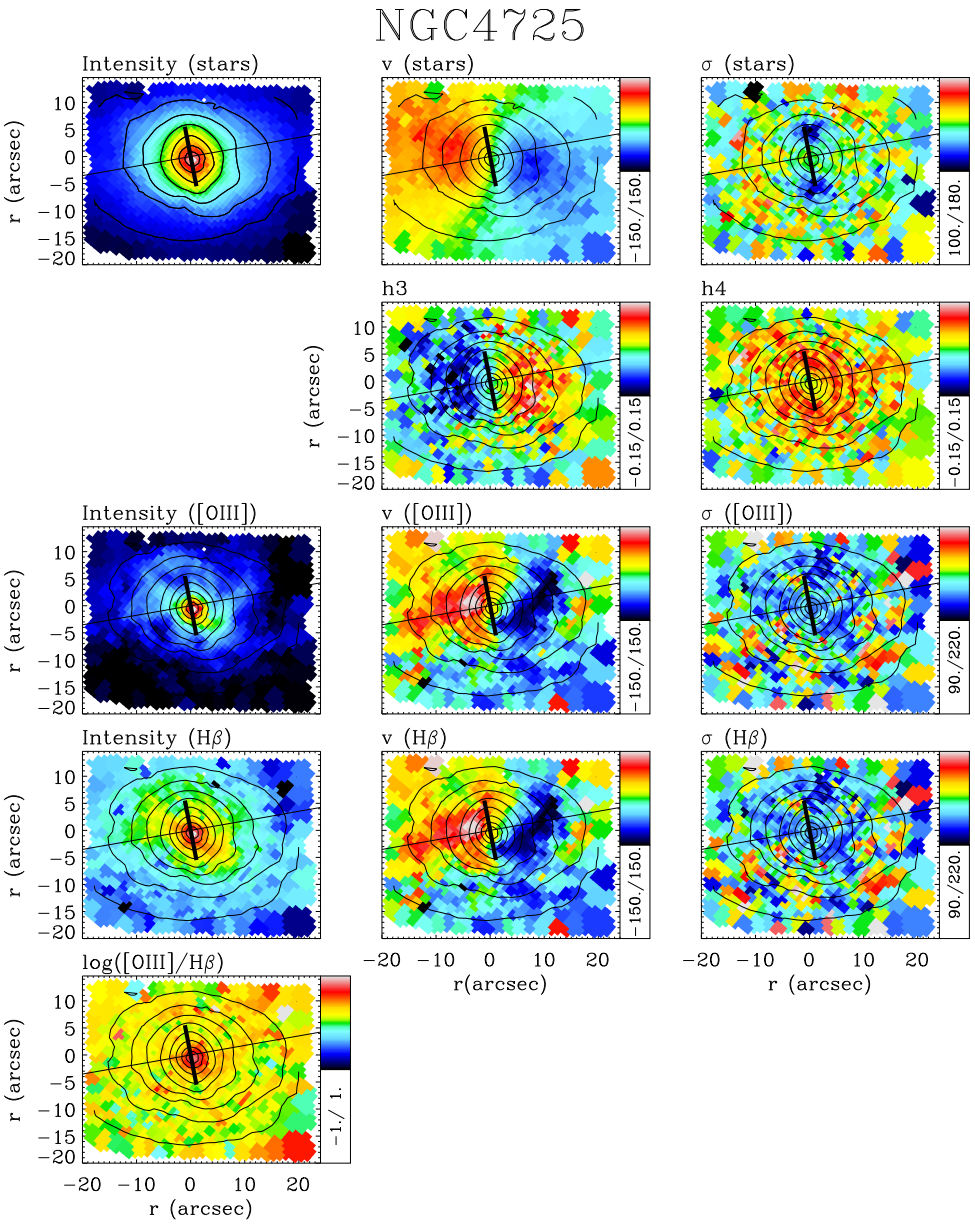

FIGURE A.5— Same as Figure A.1 but for NGC 4725. The scale is 1 arcsec ∼ 60 pc.

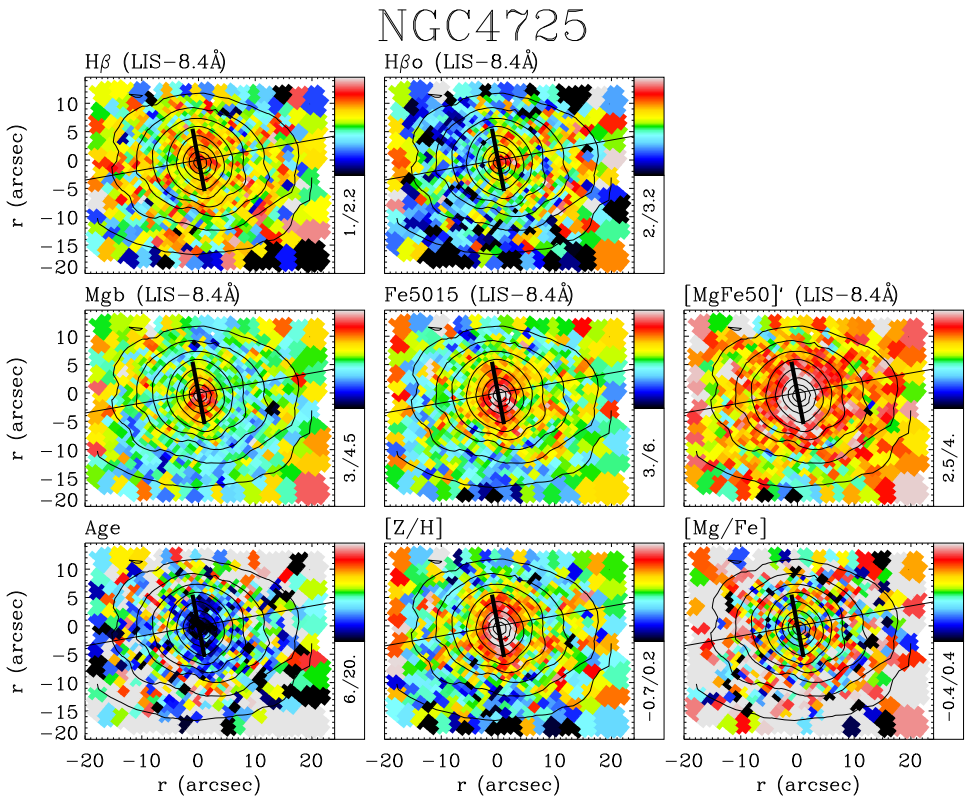

FIGURE A.6— Same as Figure A.2 but for NGC 4725. The scale is 1 arcsec ∼ 60 pc.

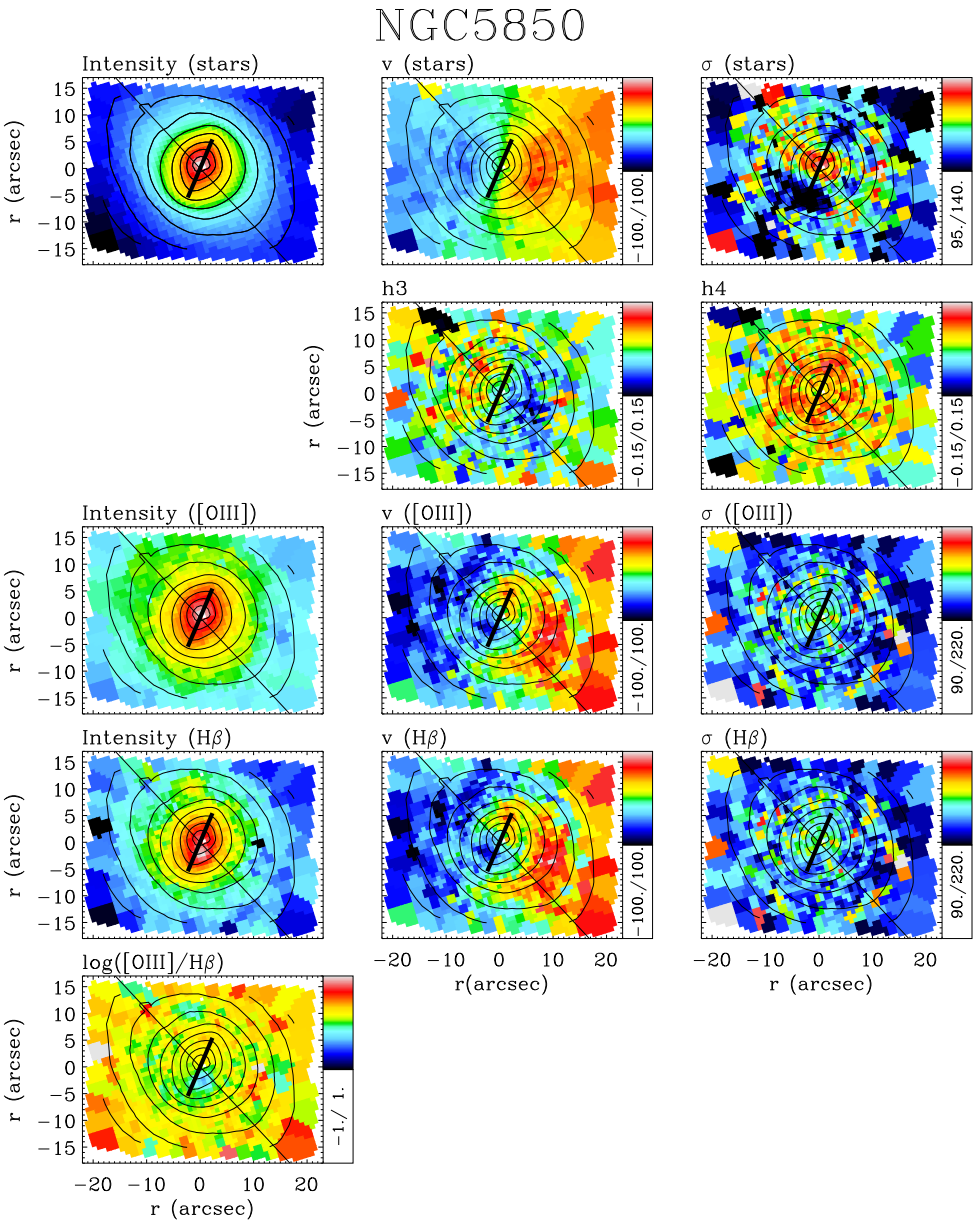

FIGURE A.7— Same as Figure A.1 but for NGC 5850. The scale is 1 arcsec ∼ 140 pc.

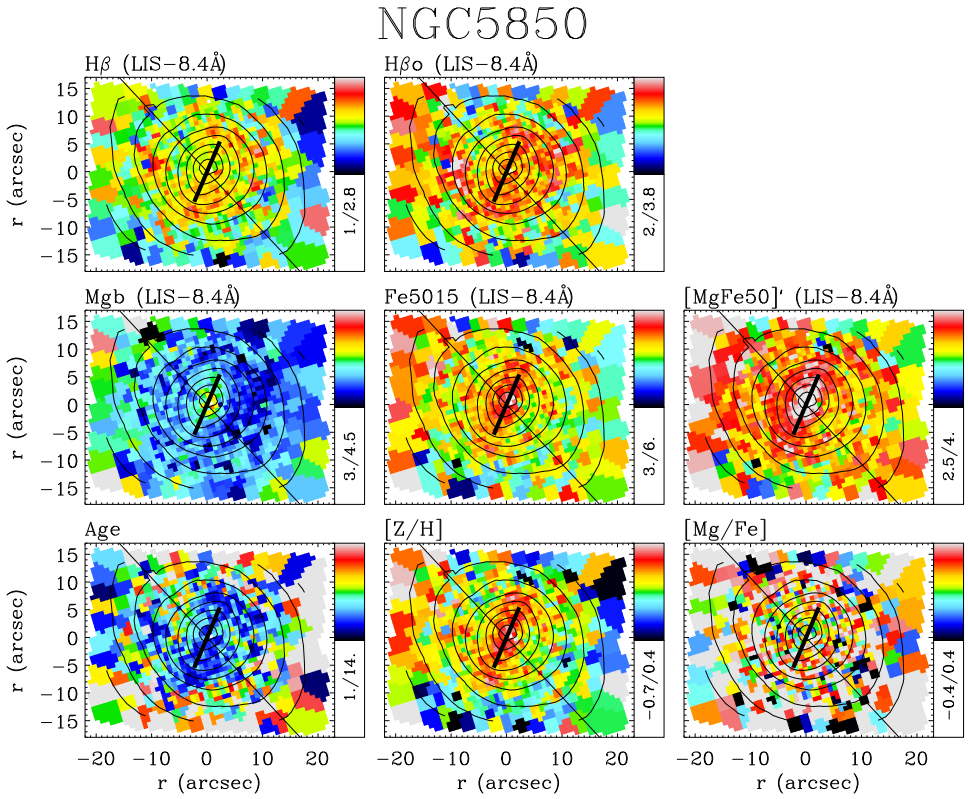

FIGURE A.8— Same as Figure A.2 but for NGC 5850. The scale is 1 arcsec ∼ 140 pc.

Muchas gracias

... si vas a venir conmigo, agárrate
Apuesta por el rock'n'roll (Héroes del silencio)

Happiness only real when shared. Hace calor. Es viernes. Me quedan un par de horas antes de salir hacia el IAC para imprimir las tropecientas copias de la tesis. Pero aún tengo unas cuantas páginas en blanco por delante. *Los agradecimientos es lo único que la gente lee*. No me gusta empezar algo que va a quedar mal irremediablemente. ¿Cómo transmitir lo que siento en solo unas palabras?. ¿Cómo no olvidar a nadie de entre la multitud de caras, situaciones y nombres que me vienen a la cabeza?. ¿Cómo recordar cada segundo de estos últimos años?. *He says "son can you play me a memory?"*.

Empecemos por lo fácil, por las incondicionales, por mis estrellitas. *Somos demasiado mayores para enfadarnos*. Ya nada nos va a separar. Por los aviones perdidos, los señores en las estaciones de tren, las llamadas urgentes por Skype, los fines de semana deluxe, los *spritz* en Rialto y el café de 8 euros, las fiestas de despedida improvisadas, las listas prohibidas, las fotos inolvidables. *Will you meet me in the middle, will you meet me in the air?*. Por la pequeña Adriana, que ya es tan guapa pese a no haber abierto los ojitos aún; lucharemos para que ella también consiga sus estrellas y pueda ser tan feliz como nosotras. Y por los chicos del 8 de agosto, por todo el tiempo que nos queda por pasar juntos, para que siempre cuiden a mis niñas.

Aquellos maravillosos años. El cole, la Universidad... Muchos amigos que han quedado lejos, pero que aún me hacen perder la noción del tiempo cuando tengo la suerte de encontrarme con ellos: Noe, Paulita, Gongui, los eileros Borjita, DVD, y Fran *el Rey*, Leo, Ali, Héctor, Bruno, Alberto, Elsa, Elena

Hernández, Rosa la de órgano...

Y otros pocos que aguantan un poquito más cerca: Jaime, el señor *toria*, el que siempre llama y siempre escucha; Pache, que no deja de sorprenderme año tras año; Sara, el motor que nos mueve a todas, con paciencia y siempre una sonrisa, para que no perdamos el contacto ni esa amistad inocente forjada hace tantos años; y Rafa, porque aunque pase el tiempo, sé que puedo volver a él en cualquier momento, a sus increíbles historias, a los libros y pelis, a la música, al juego. *Stop making the eyes at me, I'll stop making my eyes at you.*

Feo, fuerte y formal. ¿Qué decir de mis chicos?. Montse y sus pequeños milagros con la termomix, el alma de mis últimos fines de año, la reina de Amsterdam y La Gomera, la campeona de los karaokes... ; Rubi, mi maravilloso compañero de mesa. Cómo eché de menos los pterodáctilos y las orcas, las lentes y el ruido, las coca-colas sin ron, las risas y las sonrisas, el apoyo de saberle cerca; los días con Teo, desde los desayunos en el Paco hasta las cervezas en el 7 Islas, las conversaciones serias y las no tan serias, la complicidad y la sinceridad...

Carliños y las series, las cenas en su casa, las sillas rotas, la cachaça, una bandera pintada en el parking de los estudios Universal, la charla de la SEA, el Mundial en Madrid... ; Norbert, ¡que cada día está más flaco! *Por eso amigo tú alza la voz.* ¿La Senda de los cazadores?. ¡No entiendo cómo me ha aguantado tanto tiempo! Una noche en el baño con la Rebe... ¿cuántas horas pasamos allí dentro? Todo empezó con una entrevista para un trabajo de Física Solar, y después... *road trip* en un jetta azul marino con matrícula de Colorado, *take me home, country roads*, dos locos con sombrero mexicano en una estación de guaguas de Ensenada, duelo de rones, escalar, escalar y escalar, nueve bicicletas, mails interminables...

¡La familia Amorín! Cuántos años compartidos en el despacho con Ric, esa lentejada de boda, las bienvenidas y despedidas de Lu, una noche tocando la guitarra y una noticia, el 9 de agosto de 2008, una llamada Lanzarote-Barcelona, mi sobrinito Santi... Desde Tenerife a Granada, pasando por Barcelona, iremos donde haga falta.

Tenemos que ir a un concierto de U2. Los sueños por cumplir y los ya cumplidos. *Who'll stop the rain?.* Josito llevándome a la pela, Josito haciendo fideuá, Josito jugando al Risk... Conversaciones en el Jospi, llamadas los viernes por la tarde. ¡Eva y sus súper-tortillas! La Palma se ha llevado un pequeño tesoro riojano-lagunero.

Guapas, atractivas, listas, seductoras, un poco locas, ¡divines! Mis chicas de los chicharrones con pelos, los sombreros de Ascot, Ca'morfi, Anna de Codorníu:

Miggi, Tanja, Evita, Judith. De día son trabajadoras eficientes y dedicadas, de noche son divinas y divertidísimas. No quiero que se acaben esas horas de cotilleos y confesiones, de risas y vino, de señales de tráfico y gritos.

El mundo de la Astrofísica es bastante peculiar. Agradezco todos estos años de congresos, colaboraciones, trabajo en grupo... que me han permitido conocer gente tan fantástica. ¡Qué mejor ejemplo que mis *embarradas*! La loquita de Pat, con su gran sonrisa y sus enormes ojos, la afinidad y comprensión, la más divertida y un poquito despistada, que se hace querer palabra tras palabra, mirada tras mirada; la increíble Isa, la deportista más impresionante que conozco, ¡quién tuviera su vitalidad! No hay reto que la frene y, encima, tiene un corazón enorme y una generosidad sin parangón, cualidades que tiene la suerte de compartir con súper Ángel; la bondadosa Cari, de Cari&Cari, la pareja más especial del mundo. A Inma su fama le precede y es imposible no adorarla, siempre dispuesta a ayudar y a decir palabras de ánimo, siempre positiva, paciente y amable, muy inteligente y también muy divertida, se merece todo lo mejor.

Ladies' nights: Anna y Esther. Anna y su playa, su particular estilo, su gran iniciativa, su eficiencia, sus ganas interminables de disfrutar la vida. A ella le debo muchos momentos de alegría y muchas penas compartidas. Esther, loca por los mojitos, loca por bailar, loca por reír... le agradezco la confianza que me dio desde el principio. Las dos han sido fundamentales estos últimos años.

Muy presentes tengo a todos mis compañeros de lo que ahora es el grupo TRACE, antes conocido como *el grupo de Alejandro*, por el que pasan y han pasado tantos y tantos amigos: mis predecesores Conrado y José Luis, de los que tanto aprendí y que tanto me ayudaron, por aquellas cenas y aquellas tartas de cumpleaños, por los ensayos de charlas y *Seda*, por los abrazos de despedida. Cenarrín, Mike, Ignacio, ¡qué comienzos tan divertidos! Con ellos hemos llegado a ser lo que somos. Súper Nacho y las galletas de chocolate, *can you teach me how to dance real slow?*. Las nuevas generaciones que vienen pisando fuerte: Luis *el chico que siempre sonríe*, Nacho 2.0 y su escepticismo, mis ex-compis de despacho Trini y Judit, Aga y Marja.

¡Raveros al poder!. Susana *ambrosías y ron*, el entrañable Vicent, Javi Navarro y el proyecto secreto BESOS (ssssssh). Tanta gente que se ha portado tan bien conmigo: la maravillosa Katia, el bueno de Jan Lub, Enrico y su paciencia y apoyo, Richard McDermid y sus cafés, Eric y sus inesperadas palabras de ánimo. Tengo un especial cariño a Reynier, que siempre me habla en español, que siempre es tan bueno y sincero, que siempre encuentra un hueco

para mí. Los chicos de mi despacho preferido: Jesús y Alfonso, porque su ayuda profesional ha sido imprescindible pero, sobre todo, porque les adoro a nivel personal y espero mantener siempre el contacto con ellos y con Auxi, Cecilia, Elisa, Elena, Jorge y Héctor.

Mi espinita clavada es, sin duda, el grupo de solar. Manolo, Lena, Javier y Héctor siempre se han preocupado por mí y hubieran sido unos compañeros estupendos. Ahora son unos amigos estupendos. Cómo olvidar a Raquel, Orlagh y nuestras aventuras americanas. *I know I have a bad reputation, and it isn't just talk, talk, talk.* ¡Lorenzo y su café con leche antes de dormir! El grupo de *autoayuda*: Christoph, Jesús, Nayra, Manu... es genial avanzar con ellos. La dulce Cris, David Abreu, Omaira, viajes, cenas, rones, excursiones...

Es fácil acordarse de Basilio y Lourdes, a los que últimamente he dado mucho la lata con esto de la tesis y se han portado estupendamente, pese a lo cansina que he sido en más de una ocasión. Begoña, de la Comisión de Doctorado. John, un referee interno ejemplar. María Jesús Arévalo, cuyo apoyo es increíble desde que estoy en la carrera. Evencio, Antonio y Victor, que aceptaron sin pensarlo formar parte de mi tribunal.

Y por supuesto, V de Vazdekis. Han sido muchos años de encuentros y desencuentros, de conversaciones triviales y no tan triviales, de trabajo y también de amistad, de risas y lágrimas. Aunque pasen los años Alejandro siempre será mi jefe y mi amigo, y espero que esa confianza para hablar o callar siga siendo una constante en nuestra relación. Mucho cariño también para Sonia, Kyros, Aris y Hermes.

Quiero hacer hueco también para toda la familia Méndez-Abreu: Memele, Noe, Sergio, Aday, David, Nieves y Alejandro. Es verdad que en poco tiempo les he cogido muchísimo cariño a todos, pero sobre todo quiero agradecer el calor que yo he sentido por parte de ellos. Nos quedan muchos momentos por compartir y ojalá todos sean igual de buenos que hasta ahora.

He dejado para el final a mi familia porque me resulta difícil expresar cuánto les quiero y cuánto me han ayudado sin siquiera darse cuenta, simplemente por estar ahí y darme tantos momentos de familia y confianza que reconfortan y motivan a ser cada día un poquito mejor. Estoy muy orgullosa de mis primos: la guapísima doctora Beatriz, el campeón de squash Iván, mi inteligente Daniel, las pequeñas Cristi y Emma que ahora son dos pedazo de mujeres, el atractivo Tomi y su gran personalidad, y mi travieso y espabilado Joselillo. Adoro a todos mis tíos pero quiero mencionar especialmente a María José, mi tía y

madrina doble, que muchas veces es la única que me entiende, ¡literalmente!. Mi padre es una de las personas más inteligentes y buenas que conozco, me ha enseñado muchísimas cosas y siento una gran empatía hacia sus percepciones; sé que siempre me ha entendido y que está orgulloso de mí. Cuento con Adela para que me lo mime mucho.

Mi madre, fantástica, divertida y discreta. Sabe más de lo que dice y siempre me apoya aunque me equivoque. Me conoce mejor que nadie. JM, que me demuestra siempre tanto cariño; espero no fallarle nunca, él jamás lo ha hecho y sé que no lo hará. Mi Ori, que es uno más de la familia y solo da alegrías, con sus ojos despiertos y su silenciosa cercanía.

La abuela Fefi, la mejor abuela del mundo, la abuela que todos desearían tener. Con su pelo largo recogido en un moño, su mirada franca y sus manos cálidas. Siempre dice lo que necesitamos oír, nos guste o no. De ella hay mucho que aprender. El abuelo Juan, al que siempre recordaré regando el jardín, en su sillón con los cascos puestos, la sonrisa en la cara cuando llegábamos los nietos.

Mi abuela, que me acompaña cada día aunque hace ya casi nueve años que no está. Crecí con ella y gracias a ella soy como soy; compartimos durante veinte años los mejores y peores momentos de nuestra vida, y ahora sigo caminando, sola, pero recordando a cada paso todo lo que aprendí de ella.

Gracias a mi abuelo, a quien le dedico este trabajo de tantos años. Porque él siempre ha creído en mí, siempre me ha tratado con respeto y me ha dado todo para que yo pudiera elegir en cada momento el camino a seguir. Porque siempre me ha contado las cosas tal y como son y me ha enseñado la importancia del lenguaje, de la expresión, de la disciplina y de la responsabilidad. Porque ha dedicado su vida a luchar por un objetivo y ha sido un ejemplo constante en su trabajo y en su casa. Porque me arreglaba los juguetes de pequeña y me llevaba en brazos por la casa. Porque me sigue cuidando cuando quizá debería cuidarle yo a él un poquito más.

Y, por fin, gracias a Jairo. *I just need some place where I can lay my head*. Cuando empecé la tesis imaginaba que la terminaría algún día de 2010. Si hubiera sido así, probablemente no hubiera escrito estas últimas palabras. Siempre hay un lado bueno y yo he ganado años de felicidad junto a él. Ahora sé que tengo un compañero para toda la vida, y no quiero alejarme de su sonrisa, de sus ojos, de sus besos... Gracias a él, pongo este punto y final bañado de alegría.

Adriana
En Radazul, a 20 de julio de 2012

Bibliography

Abraham R. G., Merrifield M. R., 2000, AJ, 120, 2835

Aguerri J. A. L., 1999, A&A, 351, 43

Aguerri J. A. L., Balcells M., Peletier R. F., 2001, A&A, 367, 428

Aguerri J. A. L., Beckman J. E., Prieto M., 1998, AJ, 116, 2136

Aguerri J. A. L., Debattista V. P., Corsini E. M., 2003, MNRAS, 338, 465

Aguerri J. A. L., Elias-Rosa N., Corsini E. M., Muñoz-Tuñón C., 2005, A&A, 434, 109

Aguerri J. A. L., González-García A. C., 2009, A&A, 494, 891

Aguerri J. A. L., Méndez-Abreu J., Corsini E. M., 2009, A&A, 495, 491

Aguerri J. A. L., Muñoz-Tuñón C., Varela A. M., Prieto M., 2000, A&A, 361, 841

Allington-Smith J., Murray G., Content R., Dodsworth G., Davies R., et al. 2002, PASP, 114, 892

Allington-Smith J. R., Dubbeldam C. M., Content R., Dunlop C. J., Robertson D. J., et al. 2004, in Moorwood A. F. M., Iye M., eds, Society of Photo-Optical Instrumentation Engineers (SPIE) Conference Series Vol. 5492 of Society of Photo-Optical Instrumentation Engineers (SPIE) Conference Series, *Integral field spectroscopy with the Gemini Near-Infrared Spectrograph*. pp 701–710

Andredakis Y. C., Peletier R. F., Balcells M., 1995, MNRAS, 275, 874

Andredakis Y. C., Sanders R. H., 1994, MNRAS, 267, 283

Arribas S., Mediavilla E., Fuensalida J. J., 1998, ApJ, 505, L43

Arribas S., Mediavilla E., Rasilla J. L., 1991, ApJ, 369, 260

Athanassoula E., 1984, Phys. Rep., 114, 321

Athanassoula E., 1990, Annals of the New York Academy of Sciences, 596, 181

Athanassoula E., 1992, MNRAS, 259, 345

Athanassoula E., 2003, MNRAS, 341, 1179

Athanassoula E., Misiriotis A., 2002, MNRAS, 330, 35

Bacon R., 1995, in Comte G., Marcelin M., eds, IAU Colloq. 149: Tridimensional Optical Spectroscopic Methods in Astrophysics Vol. 71 of Astronomical Society of the Pacific Conference Series, *The Integral Field Spectrograph TIGER: Results and Prospects*. p. 239

Bacon R., Copin Y., Monnet G., Miller B. W., Allington-Smith J. R., et al. 2001, MNRAS, 326, 23

Baldwin J. A., Phillips M. M., Terlevich R., 1981, PASP, 93, 5

Barazza F. D., Jogee S., Marinova I., 2008, ApJ, 675, 1194

Barnes J. E., 2002, MNRAS, 333, 481

Barway S., Wadadekar Y., Kembhavi A. K., 2011, MNRAS, 410, L18

Berentzen I., Heller C. H., Shlosman I., Fricke K. J., 1998, MNRAS, 300, 49

Berentzen I., Shlosman I., Martínez-Valpuesta I., Heller C. H., 2007, ApJ, 666, 189

Bertola F., Buson L. M., Zeilinger W. W., 1992, ApJ, 401, L79

Binggeli B., Cameron L. M., 1991, A&A, 252, 27

Boone F., Baker A. J., Schinnerer E., Combes F., García-Burillo S., et al. 2007, A&A, 471, 113

Bottema R., 1989, A&A, 221, 236

Bottema R., Gerritsen J. P. E., 1997, MNRAS, 290, 585

Bournaud F., Combes F., 2002, A&A, 392, 83

Bureau M., Aronica G., Athanassoula E., Dettmar R. J., Bosma A., Freeman K. C., 2006, MNRAS, 370, 753

Bureau M., Athanassoula E., 1999, ApJ, 522, 686

Bureau M., Athanassoula E., 2005, ApJ, 626, 159

Bureau M., Chung A., 2006, MNRAS, 366, 182

Bureau M., Freeman K. C., 1997, PASA, 14, 146

Bureau M., Freeman K. C., 1999, AJ, 118, 126

Buta R., Block D. L., 2001, ApJ, 550, 243

Buta R., Combes F., 1996, Fund. Cosmic Phys., 17, 95

Cameron E., Carollo C. M., Oesch P., Aller M. C., Bschorr T., et al. 2010, MNRAS, 409, 346

Caon N., Capaccioli M., D'Onofrio M., 1993, MNRAS, 265, 1013

Cappellari M., Bacon R., Bureau M., Damen M. C., Davies R. L., et al. 2006, MNRAS, 366, 1126

Cappellari M., Copin Y., 2003, MNRAS, 342, 345

Cappellari M., Emsellem E., 2004, PASP, 116, 138

Cardiel N., 1999, PhD thesis, Universidad Complutense de Madrid, Spain

Cardiel N., Gorgas J., Sánchez-Blázquez P., Cenarro A. J., Pedraz S., et al. 2003, A&A, 409, 511

Carretero C., Vazdekis A., Beckman J. E., Sánchez-Blázquez P., Gorgas J., 2004, ApJ, 609, L45

Cepa J., Beckman J. E., 1990, ApJ, 349, 497

Cervantes J. L., Vazdekis A., 2009, MNRAS, 392, 691

Ceverino D., Klypin A., 2007, MNRAS, 379, 1155

Chapelon S., Contini T., Davoust E., 1999, A&A, 345, 81

Chung A., Bureau M., 2004, AJ, 127, 3192

Ciri R., Bettoni D., Galletta G., 1995, Nature, 375, 661

Coccato L., Morelli L., Corsini E. M., Buson L., Pizzella A., et al. 2011, MNRAS, 412, L113

Coelho P., Gadotti D. A., 2011, ApJ, 743, L13

Combes F., Debbasch F., Friedli D., Pfenniger D., 1990, A&A, 233, 82

Combes F., Sanders R. H., 1981, A&A, 96, 164

Comerón S., Knapen J. H., Beckman J. E., 2008, A&A, 485, 695

Comerón S., Martínez-Valpuesta I., Knapen J. H., Beckman J. E., 2009, ApJ, 706, L256

Contopoulos G., Grosbol P., 1989, A&A Rev., 1, 261

Contopoulos G., Papayannopoulos T., 1980, A&A, 92, 33

Corsini E. M., Aguerri J. A. L., Debattista V. P., Pizzella A., Barazza F. D., Jerjen H., 2007, ApJ, 659, L121

Corsini E. M., Debattista V. P., Aguerri J. A. L., 2003, ApJ, 599, L29

Danby J. M. A., 1965, AJ, 70, 501

de La Rosa I. G., La Barbera F., Ferreras I., de Carvalho R. R., 2011, MNRAS, 418, L74

de Vaucouleurs G., de Vaucouleurs A., Corwin Jr. H. G., Buta R. J., Paturel G., Fouque P., 1991, Third Reference Catalogue of Bright Galaxies

Debattista V. P., 2003, MNRAS, 342, 1194

Debattista V. P., Carollo C. M., Mayer L., Moore B., 2004, ApJ, 604, L93

Debattista V. P., Corsini E. M., Aguerri J. A. L., 2002, MNRAS, 332, 65

Debattista V. P., Mayer L., Carollo C. M., Moore B., Wadsley J., Quinn T., 2006, ApJ, 645, 209

Debattista V. P., Sellwood J. A., 1998, ApJ, 493, L5

Debattista V. P., Sellwood J. A., 2000, ApJ, 543, 704

Debattista V. P., Shen J., 2007, ApJ, 654, L127

Eisenhauer F., Abuter R., Bickert K., Biancat-Marchet F., Bonnet H., et al. 2003, in Iye M., Moorwood A. F. M., eds, Society of Photo-Optical Instrumentation Engineers (SPIE) Conference Series Vol. 4841 of Society of Photo-Optical Instrumentation Engineers (SPIE) Conference Series, *SINFONI - Integral field spectroscopy at 50 milli-arcsecond resolution with the ESO VLT*. pp 1548–1561

Eliche-Moral M. C., Balcells M., Aguerri J. A. L., González-García A. C., 2006, A&A, 457, 91

Eliche-Moral M. C., González-García A. C., Balcells M., Aguerri J. A. L., Gallego J., et al. 2011, A&A, 533, A104

Elmegreen B. G., Elmegreen D. M., 1985, ApJ, 288, 438

Elmegreen B. G., Elmegreen D. M., Hirst A. C., 2004, ApJ, 612, 191

Emsellem E., Arsenault R., 1997, A&A, 318, L39

Emsellem E., Cappellari M., Krajnović D., Alatalo K., Blitz L., Bois M., Bournaud F., et al. 2011, MNRAS, 414, 888

Emsellem E., Cappellari M., Peletier R. F., McDermid R. M., Bacon R., et al. 2004, MNRAS, 352, 721

Emsellem E., Greusard D., Combes F., Friedli D., Leon S., et al. 2001, A&A, 368, 52

Englmaier P., Shlosman I., 2004, ApJ, 617, L115

Erwin P., 2004, A&A, 415, 941

Erwin P., 2005, MNRAS, 364, 283

Erwin P., Beckman J. E., Vega-Beltrán J.-C., 2004, in Block D. L., Puerari I., Freeman K. C., Groess R., Block E. K., eds, Penetrating Bars Through Masks of Cosmic Dust Vol. 319 of Astrophysics and Space Science Library, *Pseudobulges in Barred SO Galaxies*. p. 775

Erwin P., Sparke L. S., 1999, ApJ, 521, L37

Erwin P., Sparke L. S., 2002, AJ, 124, 65

Erwin P., Sparke L. S., 2003, ApJS, 146, 299

Falcón-Barroso J., Bacon R., Bureau M., Cappellari M., Davies R. L., et al. 2006, MNRAS, 369, 529

Falcón-Barroso J., Balcells M., Peletier R. F., Vazdekis A., 2003, A&A, 405, 455

Falcón-Barroso J., Peletier R. F., Balcells M., 2002, MNRAS, 335, 741

Falcón-Barroso J., Peletier R. F., Emsellem E., Kuntschner H., Fathi K., et al. 2004, MNRAS, 350, 35

Falcón-Barroso J., Sánchez-Blázquez P., Vazdekis A., Ricciardelli E., Cardiel N., et al. 2011, A&A, 532, A95

Fathi K., Beckman J. E., Piñol-Ferrer N., Hernandez O., Martínez-Valpuesta I., Carignan C., 2009, ApJ, 704, 1657

Fathi K., Toonen S., Falcón-Barroso J., Beckman J. E., Hernandez O., et al. 2007, ApJ, 667, L137

Fisher D., 1997, AJ, 113, 950

Fisher D. B., Drory N., 2008, AJ, 136, 773

Freeman K. C., 1966, MNRAS, 133, 47

Freeman K. C., 1970, ApJ, 160, 811

Friedli D., Benz W., 1995, A&A, 301, 649

Friedli D., Benz W., Kennicutt R., 1994, ApJ, 430, L105

Friedli D., Martinet L., 1993, A&A, 277, 27

Gadotti D. A., Athanassoula E., Carrasco L., Bosma A., de Souza R. E., Recillas E., 2007, MNRAS, 381, 943

Gadotti D. A., de Souza R. E., 2005, ApJ, 629, 797

Gadotti D. A., de Souza R. E., 2006, ApJS, 163, 270

Ganda K., Falcón-Barroso J., Peletier R. F., Cappellari M., Emsellem E., et al. 2006, MNRAS, 367, 46

Ganda K., Peletier R. F., McDermid R. M., Falcón-Barroso J., de Zeeuw P. T., et al. 2007, MNRAS, 380, 506

Gerhard O. E., 1993, MNRAS, 265, 213

González J. J., 1993, PhD thesis, PhD thesis, University of California, Santa Cruz

Goudfrooij P., Gorgas J., Jablonka P., 1999, Ap&SS, 269, 109

Heller C., Shlosman I., Englmaier P., 2001, ApJ, 553, 661

Heller C. H., Shlosman I., 1994, ApJ, 424, 84

Heller C. H., Shlosman I., Athanassoula E., 2007, ApJ, 657, L65

Hernandez O., Wozniak H., Carignan C., Amram P., Chemin L., Daigle O., 2005, ApJ, 632, 253

Ho L. C., Filippenko A. V., Sargent W. L. W., 1997, ApJ, 487, 591

Hubble E. P., 1936, Realm of the Nebulae

Jablonka P., Gorgas J., Goudfrooij P., 2007, A&A, 474, 763

Jedrzejewski R. I., 1987, MNRAS, 226, 747

Jogee S., Barazza F. D., Rix H. W., Shlosman I., Barden M., et al. 2004, ApJ, 615, L105

Jørgensen I., 1999, MNRAS, 306, 607

Jungwiert B., Combes F., Axon D. J., 1997, A&AS, 125, 479

Kauffmann G., 1996, MNRAS, 281, 487

Kissler-Patig M., Copin Y., Ferruit P., Pécontal-Rousset A., Roth M. M., 2004, Astronomische Nachrichten, 325, 159

Knapen J. H., Shlosman I., Peletier R. F., 2000, ApJ, 529, 93

Koleva M., Prugniel P., Bouchard A., Wu Y., 2009, A&A, 501, 1269

Kormendy J., 1979, ApJ, 227, 714

Kormendy J., Bender R., 2012, ApJS, 198, 2

Kormendy J., Fisher D. B., Cornell M. E., Bender R., 2009, ApJS, 182, 216

Kormendy J., Illingworth G., 1982, ApJ, 256, 460

Kormendy J., Kennicutt Jr. R. C., 2004, ARA&A, 42, 603

Krajnović D., Cappellari M., de Zeeuw P. T., Copin Y., 2006, MNRAS, 366, 787

Kuijken K., Fisher D., Merrifield M. R., 1996, MNRAS, 283, 543

Kuntschner H., 2000, MNRAS, 315, 184

Kuntschner H., Emsellem E., Bacon R., Cappellari M., Davies R. L., et al. 2010, MNRAS, 408, 97

Laine S., Shlosman I., Knapen J. H., Peletier R. F., 2002, ApJ, 567, 97

Laurikainen E., Salo H., Buta R., 2004, ApJ, 607, 103

Laurikainen E., Salo H., Buta R., Knapen J. H., 2007, MNRAS, 381, 401

Laurikainen E., Salo H., Rautiainen P., 2002, MNRAS, 331, 880

Le Fèvre O., Saisse M., Mancini D., Brau-Nogue S., Caputi O., et al. 2003, in Iye M., Moorwood A. F. M., eds, Society of Photo-Optical Instrumentation Engineers (SPIE) Conference Series Vol. 4841 of Society of Photo-Optical Instrumentation Engineers (SPIE) Conference Series, *Commissioning and performances of the VLT-VIMOS instrument*. pp 1670–1681

Lisker T., Grebel E. K., Binggeli B., 2006, AJ, 132, 497

López-Sanjuan C., Balcells M., Pérez-González P. G., Barro G., García-Dabó C. E., et al. 2009, A&A, 501, 505

Lütticke R., Dettmar R.-J., Pohlen M., 2000, A&AS, 145, 405

MacArthur L. A., 2005, ApJ, 623, 795

MacArthur L. A., Courteau S., Holtzman J. A., 2003, ApJ, 582, 689

MacArthur L. A., González J. J., Courteau S., 2009, MNRAS, 395, 28

Maciejewski W., 2006, MNRAS, 371, 451

Maciejewski W., Sparke L. S., 1997, ApJ, 484, L117

Maciejewski W., Sparke L. S., 2000, MNRAS, 313, 745

Marinova I., Jogee S., 2007, ApJ, 659, 1176

Marinova I., Jogee S., Weinzirl T., Erwin P., Trentham N., et al. 2012, ApJ, 746, 136

Márquez I., Durret F., Masegosa J., Moles M., González Delgado R. M., et al. 2000, A&A, 360, 431

Márquez I., Masegosa J., Durret F., González Delgado R. M., Moles M., et al. 2003, A&A, 409, 459

Martin P., 1995, AJ, 109, 2428

Martinez-Valpuesta I., Knapen J. H., Buta R., 2007, AJ, 134, 1863

Martinez-Valpuesta I., Shlosman I., 2004, ApJ, 613, L29

Martinez-Valpuesta I., Shlosman I., Heller C., 2006, ApJ, 637, 214

Masters K. L., Maraston C., Nichol R. C., Thomas D., Beifiori A., et al. 2011, MNRAS, 418, 1055

Mayya Y. D., Rosa González D., Vega O., Mendez-Abreu J., Terlevich R., et al. 2012, ArXiv e-prints

Meidt S. E., Rand R. J., Merrifield M. R., 2009, ApJ, 702, 277

Méndez-Abreu J., Aguerri J. A. L., Corsini E. M., Simonneau E., 2008a, A&A, 478, 353

Méndez-Abreu J., Corsini E. M., Debattista V. P., De Rijcke S., Aguerri J. A. L., Pizzella A., 2008b, ApJ, 679, L73

Méndez-Abreu J., Sánchez-Janssen R., Aguerri J. A. L., 2010, ApJ, 711, L61

Menéndez-Delmestre K., Sheth K., Schinnerer E., Jarrett T. H., Scoville N. Z., 2007, ApJ, 657, 790

Merlin E., Chiosi C., 2006, A&A, 457, 437

Moiseev A. V., 2001, Bull. Special Astrophys. Obs., 51, 140

Moiseev A. V., Valdés J. R., Chavushyan V. H., 2004, A&A, 421, 433

Moles M., Márquez I., Pérez E., 1995, ApJ, 438, 604

Moorthy B. K., Holtzman J. A., 2006, MNRAS, 371, 583

Morelli L., Cesetti M., Corsini E. M., Pizzella A., Dalla Bontà E., et al. 2010, A&A, 518, A32

Morelli L., Corsini E. M., Pizzella A., Dalla Bontà E., Coccato L., Méndez-Abreu J., Cesetti M., 2012, MNRAS, 423, 962

Morelli L., Pompei E., Pizzella A., Méndez-Abreu J., Corsini E. M., et al. 2008, MNRAS, 389, 341

Muñoz-Tuñón C., Caon N., Aguerri J. A. L., 2004, AJ, 127, 58

Noguchi M., 1987, MNRAS, 228, 635

Ohta K., Hamabe M., Wakamatsu K. I., 1990, ApJ, 357, 71

Osterbrock D. E., Fulbright J. P., Martel A. R., Keane M. J., Trager S. C., Basri G., 1996, PASP, 108, 277

Pasquini L., Avila G., Allaert E., Ballester P., Biereichel P., et al. 2000, in Iye M., Moorwood A. F., eds, Society of Photo-Optical Instrumentation Engineers (SPIE) Conference Series Vol. 4008 of Society of Photo-Optical Instrumentation Engineers (SPIE) Conference Series, *FLAMES: a multi-object fiber facility for the VLT*. pp 129–140

Patsis P. A., Athanassoula E., 2000, A&A, 358, 45

Peletier R. F., Balcells M., Davies R. L., Andredakis Y., Vazdekis A., et al. 1999, MNRAS, 310, 703

Peletier R. F., Falcón-Barroso J., Bacon R., Cappellari M., Davies R. L., et al. 2007, MNRAS, 379, 445

Pérez I., Aguerri J. A. L., Méndez-Abreu J., 2012, A&A, 540, A103

Pérez I., Sánchez-Blázquez P., 2011, A&A, 529, A64

Pérez I., Sánchez-Blázquez P., Zurita A., 2007, A&A, 465, L9

Pérez I., Sánchez-Blázquez P., Zurita A., 2009, A&A, 495, 775

Pfenniger D., Norman C., 1990, ApJ, 363, 391

Pizzella A., Corsini E. M., Vega-Beltrán J. C., Bertola F., 2004, A&A, 424, 447

Prieto M., Gottesman S. T., Aguerri J. A. L., Varela A.-M., 1997, AJ, 114, 1413

Proctor R. N., Sansom A. E., 2002, MNRAS, 333, 517

Puerari I., Dottori H., 1997, ApJ, 476, L73

Rand R. J., Wallin J. F., 2004, ApJ, 614, 142

Rautiainen P., Salo H., Laurikainen E., 2002, MNRAS, 337, 1233

Reese A. S., Williams T. B., Sellwood J. A., Barnes E. I., Powell B. A., 2007, AJ, 133, 2846

Roth M. M., Kelz A., Fechner T., Hahn T., Bauer S. M., et al. 2005, PASP, 117, 620

Ryden B. S., Terndrup D. M., Pogge R. W., Lauer T. R., 1999, ApJ, 517, 650

Sánchez S. F., Kennicutt R. C., Gil de Paz A., van de Ven G., Vílchez J. M., et al. 2012, A&A, 538, A8

Sánchez-Blázquez P., Ocvirk P., Gibson B. K., Pérez I., Peletier R. F., 2011, MNRAS, 415, 709

Sánchez-Blázquez P., Peletier R. F., Jiménez-Vicente J., Cardiel N., Cenarro A. J., et al. 2006, MNRAS, 371, 703

Sarzi M., Falcón-Barroso J., Davies R. L., Bacon R., Bureau M., et al. 2006, MNRAS, 366, 1151

Scannapieco C., Tissera P. B., 2003, MNRAS, 338, 880

Sellwood J. A., 2006, ApJ, 637, 567

Sellwood J. A., Debattista V. P., 2006, ApJ, 639, 868

Sellwood J. A., Merritt D., 1994, ApJ, 425, 530

Sérsic J. L., 1968, Atlas de galaxias australes

Shen J., Debattista V. P., 2009, ApJ, 690, 758

Sheth K., Elmegreen D. M., Elmegreen B. G., Capak P., Abraham R. G., et al. 2008, ApJ, 675, 1141

Sheth K., Regan M. W., Scoville N. Z., Strubbe L. E., 2003, ApJ, 592, L13

Shlosman I., Begelman M. C., Frank J., 1990, Nature, 345, 679

Shlosman I., Frank J., Begelman M. C., 1989, Nature, 338, 45

Shlosman I., Heller C. H., 2002, ApJ, 565, 921

Shlosman I., Peletier R. F., Knapen J. H., 2000, ApJ, 535, L83

Sparke L. S., Sellwood J. A., 1987, MNRAS, 225, 653

Thomas D., Maraston C., Johansson J., 2011, MNRAS, 412, 2183

Tonry J., Davis M., 1979, AJ, 84, 1511

Trager S. C., Faber S. M., Worthey G., González J. J., 2000, AJ, 120, 165

Trager S. C., Worthey G., Faber S. M., Burstein D., González J. J., 1998, ApJS, 116, 1

Tremaine S., Weinberg M. D., 1984, ApJ, 282, L5

Tully R. B., 1974, ApJS, 27, 415

Tully R. B., 1988, Nearby galaxies catalog

van den Bergh S., 1976, ApJ, 206, 883

van den Bergh S., 2002, AJ, 124, 782

van der Marel R. P., Franx M., 1993, ApJ, 407, 525

Vazdekis A., 1999, ApJ, 513, 224

Vazdekis A., Arimoto N., 1999, ApJ, 525, 144

Vazdekis A., Kuntschner H., Davies R. L., Arimoto N., Nakamura O., Peletier R., 2001, ApJ, 551, L127

Vazdekis A., Peletier R. F., Beckman J. E., Casuso E., 1997, ApJS, 111, 203

Vazdekis A., Sánchez-Blázquez P., Falcón-Barroso J., Cenarro A. J., Beasley M. A., et al. 2010, MNRAS, 404, 1639

Vazdekis A., Trujillo I., Yamada Y., 2004, ApJ, 601, L33

Véron-Cetty M. P., Véron P., 2006, A&A, 455, 773

Wilkinson A., Sharples R. M., Fosbury R. A. E., Wallace P. T., 1986, MNRAS, 218, 297

Worthey G., Faber S. M., González J. J., 1992, ApJ, 398, 69

Worthey G., Faber S. M., González J. J., Burstein D., 1994, ApJS, 94, 687

Worthey G., Ottaviani D. L., 1997, ApJS, 111, 377

Wozniak H., 2007, A&A, 465, L1

Wozniak H., Champavert N., 2006, MNRAS, 369, 853

Wozniak H., Combes F., Emsellem E., Friedli D., 2003, A&A, 409, 469

Wozniak H., Friedli D., Martinet L., Martin P., Bratschi P., 1995, A&AS, 111, 115

Wozniak H., Pierce M. J., 1991, A&AS, 88, 325

Yamada Y., Arimoto N., Vazdekis A., Peletier R. F., 2006, ApJ, 637, 200

Yoachim P., Dalcanton J. J., 2008, ApJ, 683, 707

York D. G., Adelman J., Anderson Jr. J. E., Anderson S. F., Annis J., et al. 2000, AJ, 120, 1579

Zimmer P., Rand R. J., McGraw J. T., 2004, ApJ, 607, 285

Zwicky F., 1957, Morphological astronomy